On the Frequency-Dependence of Electrical Soil Properties and their Influence on Ground-Penetrating Radar

vorgelegt von
Master of Science (Applied Geophysics)
Markus Loewer
geb. in München

von der Fakultät VI - Planen Bauen Umwelt
der Technischen Universität Berlin
zur Erlangung des akademischen Grades

Doktor der Naturwissenschaften
- Dr. rer. nat. -

genehmigte Dissertation

Promotionsausschuss:

Vorsitzender:	Prof. Dr. Wilhelm Dominik
Gutachterin:	Prof. Dr. Charlotte Krawczyk
Gutachter:	Prof. Dr. Frank Börner
Gutachter:	Prof. Dr. Jens Tronicke
Gutachter:	Dr. Jan Igel

Tag der wissenschaftlichen Aussprache: 5. Juni 2018

Berlin 2018

Abstract

Ground-Penetrating Radar (GPR) is sensitive to changes of electrical soil properties. These properties can become strongly frequency-dependent, even so they are considered constant in many applications. Analysis of radargrams provided evidence that radar waves propagating in moist loamy and clayey soils underlie strong absorption and dispersion effects. The energy absorption together with the wavelet distortion can reach a degree that even shallow buried objects, as for instance in case of landmine or utility detection, cannot be detected by GPR. In this context, the question on the physical origin and extent of individual dielectric relaxation and conduction mechanisms arose and how they affect GPR. In addition, the demand for a prognosis facility emerged to predict the GPR performance with respect to the soil. As the topic has barely been analyzed in the past, the study aims to fill this gap using a combination of field measurements, extensive laboratory investigations and numerical simulations with a variety of soils.

To address the causes of absorption and dispersion, electrical properties of soils in the GPR frequency range were analyzed using dielectric spectroscopy. The different electrical loss-mechanisms were separated from each other by fitting a generalized dielectric response model to the data. It was found that the effective permittivity of most soils can be split into i) a dielectric relaxation of free water molecules at microwave frequency, ii) a very broadband distribution of relaxations attributed to relaxations at the interface of the multiphase system, which spans across several orders of magnitude, iii) and a constant dc-conductivity term. The very broadband distribution of low-frequency relaxations showed severe impact on GPR especially in moist clayey soils. In order to resolve the relaxation parameters of that process, the high-frequency dielectric spectroscopy data were combined with low-frequency Spectral Induced Polarization (SIP). A new dielectric model was developed that enabled to accurately explain the extraordinary large spectrum. The combined permittivity and conductivity model (CPCM) showed that the broadband interfacial relaxations can be described using two Cole-Cole relaxation models: one model with relaxation frequencies between 2 and 40 MHz, which was partially attributed to the relaxation of physically bound and hydrated water at the mineral-water interfaces, and one model with a broad relaxation time distribution and relaxation frequencies between 100 kHz and 16 MHz, which was attributed to spatial relaxations of the Maxwell-Wagner type together with the counterion relaxations in the electrical double layer (EDL).

Based on dielectric spectroscopy of the soils, an extensive GPR simulation study was carried out. The measured frequency-dependent electrical soil properties were incorporated into a FDTD code using a multi-Debye term decomposition. The simulation result using GPR wavelets with different center frequency showed that in lossy and dispersive soils a precise description of the electrical soil parameters is essential. Simplified assumptions can only be made for sandy soils, which can be described using a single Debye process for the free water relaxation and a constant dc-conductivity term. Finer-grained soils, like silty clay, requires three Debye relaxations for an adequate data fit and therefore a realistic simulation result.

As a practical result of this thesis, a method is presented that enables to predict the GPR performance in the field using a conventional moisture sensor. The method is based on the time-domain reflectometry (TDR) principle and incorporates not only losses due to the dc-conductivity, but also dielectric relaxation losses in the soil. In order to derive the performance, intrinsic attenuation of various soils were measured using a TDR sensor that was calibrated based on dielectric spectroscopy data. Additionally, the results were compared to data from low-frequency measurement techniques as Geoelectrics. The results confirmed that the measurement of dc-conductivity alone fails to predict the GPR performance and that losses due to dielectric relaxations have to be taken into account.

In summary, dispersive soils have generally a negative influence on most GPR applications, which is particularly due to the reduced resolution and penetration depth. On the other hand, using multi-frequency sensing techniques or the incorporation of dielectric relaxation models in full waveform inversion can possibly help to assess soil physical parameters from GPR in the future, as e.g. the amount of physically bound water, the cation exchange capacity (CEC) or the clay and silt fraction of the soil.

Kurzfassung

Das Georadar (GPR) ist sensitiv gegenüber Änderungen der elektrischen Bodeneigenschaften. Hierbei können diese Eigenschaften stark von der Frequenz abhängen, obwohl sie bei vielen Anwendungen als konstant angenommen werden. Bei der Auswertung von Radargrammen konnte nachgewiesen werden, dass die Ausbreitung von Radarwellen in feuchten, tonhaltigen und schluffigen Böden starken Absorptions- und Dispersionseffekten unterliegt. Die Energieabsorption in Verbindung mit der Verzerrung des Nutzsignals kann dabei so stark werden, dass selbst oberflächennah vergrabene Objekte, wie zum Beispiel im Falle der Detektion von Landminen- oder von Versorgungsleitungen, mit Hilfe des GPRs nicht mehr detektiert werden können. In diesem Zusammenhang kommt die Frage über den physikalischen Ursprung und das Ausmaß der einzelnen dielektrischen Relaxations- und elektrischen Leitungsmechanismen auf und in wieweit diese das GPR beeinflussen. Zusätzlich besteht der Bedarf einer Prognosemöglichkeit, um die GPR Performance in Abhängigkeit vom Boden zu beurteilen. Da dieses Gebiet in der Vergangenheit nur unzureichend analysiert wurde, versucht diese Arbeit dazu beizutragen, die Lücke durch eine Kombination aus Feldmessungen, umfangreichen Labormessungen und numerischen Simulationen an einer Vielzahl von Böden zu schließen.

Um den Ursachen der Absorption und Dispersion auf den Grund zu gehen, wurden die elektrischen Eigenschaften von Böden mit Hilfe der dielektrischen Spektroskopie im Frequenzbereich des GPRs untersucht. Durch Anpassen eines generalisierten dielektrischen Antwortmodells an die Daten konnten die unterschiedlichen elektrischen Verlustmechanismen voneinander getrennt werden. Es wurde festgestellt, dass die effektive Permittivität der meisten Böden in i) eine dielektrische Relaxation freier Wassermoleküle im unteren Mikrowellen- Frequenzbereich, ii) eine sehr breitbandige Verteilung von Relaxationen, die durch Relaxationen an den Grenzschichten des Mehrphasensystems verursacht wird und sich über zahlreiche Größenordnungen erstreckt und zusätzlich iii) einen Gleichstrom-Leitfähigkeitsterm unterteilt werden kann. Die sehr breitbandige Verteilung niederfrequenter Relaxationen zeigte speziell bei feuchten und tonhaltigen Böden einen starken Einfluß auf die GPR Performance. Um die Relaxationsparameter dieses Prozesses näher aufzulösen, wurden die hochfrequenten Daten der dielektrischen Spektroskopie mit niederfrequenten Messungen der Spektralen Induzierten Polarisation (SIP) kombiniert. Ein neues dielektrisches Modell wurde entwickelt, welches ermöglicht, das außergewöhnlich große Spektrum präzise zu beschreiben. Durch das kombinierte Permittivitäts- und Leitfähigkeitsmodel (CPCM) wird

aufgezeigt, dass die breitbandigen Grenzschicht- Relaxationsprozesse am besten mit Hilfe zweier Cole-Cole Modelle beschrieben werden können: einem Modell, mit Relaxationsfrequenzen zwischen 2 und 40 MHz, welches teils der Relaxation des gebundenen und hydrierten Wassers an der Grenzschicht zwischen dem Mineral und Wasser zugeordnet wurde und einem Modell, mit einer breiten Verteilung an Relaxationsfrequenzen zwischen 100 kHz und 16 MHz, welches der räumlichen Relaxation des Maxwell-Wagner Types zugeordnet wurde, zusammen mit der Gegen-Ion-Relaxation in der elektrischen Doppelschicht (EDL).

Basierend auf der dielektrischen Spektroskopie der Böden, wurde eine umfassende Studie mit GPR Simulationen durchgeführt. Die frequenzabhängigen elektrischen Bodeneigenschaften wurden mit Hilfe einer Zerlegung in multi-Debye Terme in einem FDTD Code berücksichtigt. Das Simulationsergebnis mit GPR Wavelets unterschiedlicher Mittenfrequenz deutete darauf hin, dass in verlustreichen und dispersiven Böden eine genaue Beschreibung der elektrischen Bodenparameter unumgänglich ist. Vereinfachte Annahmen können lediglich für sandige Böden getroffen werden, welche mittels eines einzelnen Debye-Prozesses für die Relaxation des freien Wassers und einem konstanten Gleichstrom-Term im gesamten GPR-Frequenzbereich beschrieben werden können. Feinkörnigere Böden, wie schluffiger Ton, benötigen hingegen drei Debye Relaxationen für einen ausreichenden Daten-Fit, um ein realistisches Simulationsergebnis zu erhalten.

Als praktisches Resultat stellt diese Arbeit ein Verfahren vor, welches die Vorhersage der GPR Performance mit Hilfe eines konventionellen Feuchtigkeitssensors im Feld erlaubt. Die Methode basiert auf dem Prinzip der Zeitbereichs-Reflektometrie (TDR) und bezieht nicht nur Gleichstromverluste, sondern ebenso Verluste aufgrund dielektrischer Relaxationen im Boden mit ein. Um die Performance abzuleiten wurde die intrinsische Dämpfung einer Vielzahl von Böden mit einem TDR-Sensor gemessen, welcher anhand von dielektrischen Spektroskopie-Daten kalibriert wurde. Zusätzlich wurden die Ergebnisse mit Daten niederfrequenter Messungen, wie dem Geoelektrik-Verfahren verglichen. Die Ergebnisse bestätigten, dass die Messung der Gleichstromleitfähigkeit allein nicht ausreicht, um die Performance von GPR vorherzusagen und dass die Verluste aufgrund dielektrischer Relaxationen berücksichtigt werden müssen.

Zusammenfassend betrachtet, haben dispersive Böden generell einen negativen Einfluss auf typische GPR Anwendungen, was insbesondere auf ein veringertes Auflösungsvermögen und eine geringe Eindringtiefe zurückzuführen ist. Jedoch ist es vorstellbar mit Hilfe von Multi-Frequenz Systemen oder durch Einbeziehung von dielektrischen Relaxationsmodellen in der Full-Waveform Analyse, bodenphysikalische Parameter, wie z.B. den Anteil an gebundenem Wasser, die Kationaustauschkapazität (CEC) oder den Ton- und Schluffgehalt durch GPR in Zukunft abzuschätzen.

Contents

List of Publications

1.) Loewer, M., Igel, J. & Wagner, N. (2016): Spectral Decomposition of Soil Electrical and Dielectric Losses and Prediction of *In Situ* GPR Performance. IEEE Journal of Selected Topics in Earth Observations and Remote Sensing, 9(1), pp. 212-220, doi: https://doi.org/10.1109/JSTARS.2015.2424152.

2.) Loewer, M., Günther, T., Igel, J., Kruschwitz, S., Martin, T. & Wagner, N. (2017): Ultra-broadband electrical spectroscopy of soils and sediments – A combined permittivity and conductivity model. Geophysical Journal International, 210(3), pp. 1360-1373, doi: https://doi.org/10.1093/gji/ggx242.

3.) Loewer, M. & Igel, J. (2017): Multi-Pole Debye Description of Lossy and Dispersive Media for realistic FDTD Simulation of GPR. Geophysics, submitted.

List of Figures

List of Tables

Nomenclature

Acronyms

ABC	absorbing boundary condition
cc	cross-correlation
CC	Cole-Cole
CEC	cation exchange capacity
CFL	Courant-Friedrich-Lewy
CPCM	combined permittivity and conductivity model
CRIM	complex refractive index model
CTL	coaxial transmission line
DC	direct-current
EDL	electrical double layer
EM	electromagnetic
env	envelope
FDTD	finite-difference time-domain
FFT	fast Fourier transform
GIMLi	Geophysical Modelling and Inversion Library
GPR	ground-penetrating radar
HF	high-frequency
IED	improvised explosive device
KK	Kramers-Kronig
LF	low-frequency
MCM	model covariance matrix
MWE	Maxwell-Wagner effect
OBS	Obersulzbach
PM	propagation matrix
PML	perfectly matched layer
rRMS	relative root mean square
SI	international system of units
SIP	spectral induced polarization
TDR	time-domain reflectometry
UXO	unexploded ordnance
VNA	vector network analyzer
we	wavelet elongation

Symbols

A_{TDR}	TDR amplitude	
$\alpha = \alpha_i$	intrinsic attenuation	$\frac{Np}{m}$
α_s	scattering attenuation	$\frac{Np}{m}$
α_t	total attenuation	$\frac{Np}{m}$
B	band width	Hz
$\mathbf{B}$	magnetic induction	$T = \frac{Vs}{m^2}$
$\beta_n = 1 - \alpha_n$	streching exponent of relaxation process n	
c_0	speed of light	$2.998 \times 10^8 \frac{m}{s}$
C_{tot}	total carbon content	
$\mathbf{D}$	electric displacement	$\frac{C}{m^2}$
δ_s	skin depth	m
$\tan\delta$	loss tangent	
$\mathbf{E}$	electric field strength	$\frac{V}{m}$
ε	dielectric permittivity (diel. perm.)	$\frac{F}{m} = \frac{As}{Vm}$
ε_∞	high-frequency limit of (relative) diel. perm.	
ε_0	vacuum dielectric permittivity	$8.854 \times 10^{-12} \frac{F}{m}$
ε_r	relative dielectric permittivity	
ε^*	complex dielectric permittivity	$\frac{F}{m}$
ε_r^*	complex relative dielectric permittivity	
ε_{eff}	effective dielectric permittivity	$\frac{F}{m}$
ε_{eff}^*	complex effective dielectric permittivity	$\frac{F}{m}$
$\varepsilon_{r,eff}^*$	complex relative effective diel. perm.	
$\Delta\varepsilon_i$	relaxation strength of the i-th process	
f	frequency	$Hz = \frac{1}{s}$
f_r	relaxation frequency	Hz
f_{cr}	critical frequency	Hz
f_c	center frequency	Hz
F	formation factor	
$\Delta G^\#$	Gibbs free energy	J
γ	propagation constant	$\frac{1}{m}$
h	Planck constant	$6.626 \times 10^{-34} Js$
$\mathbf{H}$	magnetic field strength	$\frac{A}{m}$
$\Delta H^\#$	activation enthalpy	$\frac{J}{mol}$
i	complex number	
$\mathbf{J}_d$	displacement current density	$\frac{A}{m^2}$
$\mathbf{J}_f$	electric current density (of free charges)	$\frac{A}{m^2}$

k	permeability	mD
k_B	Boltzmann constant	$1.381 \times 10^{-23} \frac{J}{K}$
κ	(volume specific) magnetic susceptibility	
κ_{FD}	frequency-dependance of κ (in %)	
$\Delta\kappa$	total (volume specific) magnetic susceptibility	
l	length	m
λ	wave length	m
m	Archie exponent (cementation exponent)	
m_n	chargeability of process n	$\frac{mV}{V}$
m_d	mass of dry fraction	kg
m_w	mass of water fraction	kg
$\mathbf{M}$	magnetization	$\frac{A}{m}$
μ	magnetic permeability	$\frac{H}{m} = \frac{Vs}{Am}$
μ_0	vacuum magnetic permeability	$4\pi \times 10^{-7} \frac{H}{m}$
μ_r	relative magnetic permeability	
μ^*	complex magnetic permeability	$\frac{H}{m}$
∇	Nabla operator	
ω	angular frequency	$\frac{rad}{s}$
$\mathbf{P}$	dielectric polarization	$\frac{C}{m^2}$
ϕ	porosity	
φ	phase shift	rad
Q^*	EM 'quality' factor	
r	distance or radius	m
R	gas constant	$8.314 \frac{J}{Kmol}$
ρ	electric resistivity	Ωm
ρ^*	complex electric resistivity	Ωm
ρ_b	bulk density	$\frac{g}{cm^3}$
ρ_d	dry density	$\frac{g}{cm^3}$
ρ_f	volume charge density (f: free)	$\frac{C}{m^3}$
ρ_s	grain density	$\frac{g}{cm^3}$
ρ_w	density of water	$\frac{g}{cm^3}$
S_{ii}	scattering parameters ($i = 1, 2$)	
S_{sp}	specific surface area	$\frac{m^2}{g}$
$\Delta S^{\#}$	activation entropy	$\frac{J}{Kmol}$
σ	electrical conductivity	$\frac{S}{m}$
σ_∞	high-frequency limit of electrical conductivity	$\frac{S}{m}$
σ_{HF}	high-frequency electrical conductivity	$\frac{S}{m}$
σ_{dc}	direct-current electrical conductivity	$\frac{S}{m}$
σ^*	complex electrical conductivity	$\frac{S}{m}$
σ_{eff}	effective electrical conductivity	$\frac{S}{m}$

σ^*_{eff}	complex effective electrical conductivity	$\frac{S}{m}$
$\Delta\sigma_n$	relaxation strength of the n-th process	$\frac{S}{m}$
t	time	s
T	temperature	$^\circ C$ or K
τ	relaxation time	s
τ_w	relaxation time of (free) water	ps
τ_{bw}	relaxation time of bound water molecules	ps
θ_v	volumetric water content	cm^3
θ_g	gravimetric water content	g
v	phase velocity	$\frac{m}{s}$
V_i	TDR voltage magnitude in medium i	cm^3
V_a	volume of air fraction	cm^3
V_b	bulk volume	cm^3
V_w	volume of water fraction	cm^3
χ_e	electric susceptibility	
χ_m	magnetic susceptibility	
χ^2	chi square value (goodness of fit)	
z	depth	m
ζ	wave coefficient (phase constant)	$\frac{rad}{m}$

1. Introduction

1.1. Background

For many years, GPR is successfully used in different application areas from non-destructive testing of concrete reinforcements (Hugenschmidt, 2010) to the mapping of glacial ice thickness in the Antarctica (Vaughan et al., 1999). It is frequently used in civil and geotechnical engineering for locating service utilities in the underground, like cables and pipes and to evaluate structures with respect to cracks and voids (Yelf, 2007). Other areas comprise archaeological prospection (Vaughan, 1986) as well as contaminant mapping (Redman, 2009) and hydrological investigations (Slater and Comas, 2009). Thus, most GPR applications focus on the first few meters of the subsurface, since the electrical properties of soils often restrict EM waves to penetrate deeper. However, the properties that determine success or failure of GPR are generally unknown and the suitability of GPR for a particular soil can only be verified by trial and error. Nevertheless, in some cases the knowledge of the electrical properties and their influence on GPR must be known in advance, since it can be of lethal importance in the field. For instance, one of these cases comprise the detection of landmines in post-conflict zones. Here, GPR is often used complementary to a metal detector (dual sensor) in order to reduce the high false alarm rate and since modern plastic landmines only contain little metal parts[1] (Takahashi and Sato, 2008; Kaspan et al., 2010; Takahashi et al., 2011). Apart from landmines, there is also demand to track explosive ordnance of modern terrorist warfare, such as improvised explosive devices (IED), which can strongly vary in form, size or material. In contrast to landmines, these devices are often found in greater depth (Igel et al., 2013b), where EM energy absorption can strongly influence the detection probability.

The practical application of GPR has shown that the method is very useful in many cases, but also fails under certain circumstances. The conditions that lead to a limited usability of GPR can be diverse. One of the most important factors influencing the performance of the high-frequency EM technique are the electrical properties of the soil. In order to be useful as an imaging tool, GPR requires a preferably strong electrical contrast between a potential target and the surrounding soil. However, previous

[1] Despite the Ottawa treaty of 1997, in which most UN-countries pledged themselves to ban anti-personnel mines, there are still remains of armed conflicts in more than 64 countries (ICBL-CMC, 2016)

studies have shown that the small-scale variability of electrical soil properties or other heterogeneities like roots and stones can also lead to the diffraction and scattering of GPR energy which can mask the signals from shallow buried objects, like landmines (Igel, 2007, 2008; Takahashi et al., 2012). In addition, when using GPR to detect deeper buried objects and structures, energy absorption and dispersion effects play an increasing role. These effects strongly depend on soil type, moisture condition and also the frequency of the EM field. In many cases, simplified assumptions are made relating to the electrical properties of soils. GPR test sites for instance, often use optimal reference media like sand, in order to test the GPR performance. However clean sand is nearly radar-transparent in comparison to natural soils, which contain at least some small amounts of clay and increased moisture content. Thus, simplifications can lead to false prediction of the GPR performance or false interpretation of the reasons behind its failure. Furthermore, oversimplified assumptions do not contribute the ambition to explore a greater range of possible application areas, as to receive a wider range of soil physical parameters by GPR.

In this context, the frequency-dependence of the electrical soil properties plays an important role. Commercial pulse GPR systems can be provided with a multitude of antennas with different center frequencies from the MHz to the lower GHz frequency ranges. Therefore, the first step in a GPR field application is often to find the best trade-off between penetration depth and resolution, which are both strongly controlled by frequency. Due to the frequency-dependent nature of the electrical soil properties, GPR waves undergo different attenuation and can also have different phase velocities with respect to the frequency range of the emitted pulse. Multi-offset GPR can be used in order to derive water content of the soil by means of velocity (Igel et al., 2001; Huisman et al., 2003) and in combination with dielectric mixing models or empirically determined relationships (e.g. CRIM; Topp et al., 1980; Dobson et al., 1985). However, for dispersive and lossy soils the results can vary dependent to the chosen model and frequency of the GPR system, and therefore lead to different water content predictions. More importantly, each GPR pulse contains a certain frequency bandwidth and thus, wavelets propagating in frequency-dependent media get distorted, which results in blurry images especially of deeper reflections in the radargram. Some studies exist that approximate the soil-dependent dispersion using a constant Q^* factor and incorporate it into GPR processing or that even try to derive the clay and water content from frequency-dependent attenuation in the radargram (e.g. Irving and Knight, 2003; Bradford, 2007, 2011; Wunderlich and Rabbel, 2013). However, most approximations of the electrical properties for fine-grained soils and also their incorporation into simulations (e.g. Powers, 2001; Cassidy, 2001) are based on very few sources (e.g. Olhoeft and Capron, 1993) and precise measurements of the frequency-dependent electrical soil parameters and accurate model fitting have rarely been carried out. Apart from measurements of soil electrical parameters, the question on the physical origin and extent of the underlying dielectric relaxation and conduction mechanisms and their

individual influence on GPR has not been answered; especially not considering the full frequency range of the GPR method. In addition to these rather fundamental and laboratory intensive investigations, the demand for a prognosis facility came up that enables to predict the GPR performance in-situ with respect to the soil. Considering some of the described application areas for GPR, the knowledge about its limitation as a detection device can be of great importance for the user in the field.

1.2. Aims and objectives

Frequency-dependent properties of soils play an important role in many GPR applications. Whereas the detection of landmines, IEDs, cables or service utilities require high GPR frequencies, geological, geotechnical or hydrogeological investigations use rather low frequencies. This work aims to investigate the frequency-dependent electrical soil properties on the entire frequency band that is relevant for the GPR method. Furthermore, the thesis generally tries to cover all sources of intrinsic attenuation and dispersion in soils when exposed to an applied EM field and therefore spans a much wider frequency range. The electrical soil properties, not only in the frequency range of GPR, but also in the lower frequency range, carry important information on its composition and therefore, different geophysical methods can be used in order to reveal them. One question that is addressed in this context is, which electromagnetic method complements GPR as a technique that is sensitive to high-frequency electrical properties and which methods underestimate these properties due to frequency. The thesis tries to answer this question with respect to the frequency-dependent response of the soil. The objectives of the thesis are

- to analyze and interpret the frequency-dependent response of the electrical properties of soils, i.e., the effective dielectric permittivity or the effective electrical conductivity,
- to develop an adequate phenomenological model, which enables to fit the measured data for a variety of soils with different water content, mineralogy and texture,
- to provide an empirical measure for the strength and nature of the individual loss mechanisms in soils with respect to the GPR frequency band,
- to predict the performance of GPR based on elaborate dielectric spectroscopy of soils,
- to find a simplified method that enables to predict the performance of GPR in the field,
- to produce realistic GPR simulations that can incorporate measured frequency-dependent electrical properties of soils with high accuracy,

- and to verify, whether accurate soil parameter models are necessary for GPR simulations or if simplified assumptions can suffice.

1.3. Guideline of the thesis

The basis of the thesis is build on three publications presented in chapters 4, 5 and 6, in which the above listed objectives are addressed. The following guideline gives a brief overview on the content of each chapter.

Chapter 2 presents fundamental physical equations from the EM theory. It furthermore introduces effective parameters and their origin in the context of complex electrical parameter measurements, which are presented in paper 1 and 2 in reduced form. The chapter also presents the different concepts of electrical polarization and relaxation mechanisms that can occur in moist soil, and which are the inherent origin of the frequency-dependence.

Chapter 3 gives a brief overview on the geophysical methods that were used throughout the thesis with an increased focus on GPR and dielectric spectroscopy.

Chapter 4 is publication I: Loewer, M., Igel, J. and Wagner, N. (2016): Spectral Decomposition of Soil Electrical and Dielectric Losses and Prediction of *In Situ* GPR Performance, IEEE Journal of Selected Topics in Earth Observations and Remote Sensing, 9(1), pp. 212-220. doi: https://doi.org/10.1109/JSTARS.2015.2424152.

The paper introduces the problem of intrinsic attenuation in GPR with respect to different soils. It analyzes the electrical soil properties using dielectric spectroscopy in the GPR frequency range. The paper shows a decomposition approach of the dielectric spectra in order to derive the individual contribution of different loss mechanisms to the overall intrinsic attenuation. As a practical result, it verifies that measurements of dc-conductivity do not suffice in order to predict the GPR performance in the field. In contrast, a simple method is presented that enables to predict the performance by means of a calibrated field-moisture sensor based on TDR.
Appendix A.2 briefly introduces new advancements of the soil suitability assessment via TDR, which has been developed on basis of a greater data volume after the publication of this paper. It introduces the conventional, but specifically calibrated field moisture sensor, which enables to measure dielectric permittivity and intrinsic attenuation.

Chapter 5 is publication II: Loewer, M., Günther, T., Igel, J., Kruschwitz, S., Martin, T. and Wagner, N. (2017): Ultra-broad-band electrical spectroscopy of soils and sediments - a combined permittivity and conductivity model, Geophysical Journal International, 210(3), pp. 1360-1373, Oxford Uni. P., doi: https://doi.org/10.1093/gji/ggx242.

The paper addresses the general problem of dielectric relaxations in electrical spectra, which go beyond the range of an individual frequency-dependent measurement technique. Therefore, it combines the high-frequency dielectric spectroscopy data for the 1 MHz to 10 GHz frequency range, with low-frequency resistivity and phase data using SIP between 1 mHz to 45 kHz. A new semi-empirical model was developed that enabled to accurately explain the extraordinary large electrical response spectrum for different soils and one sandstone.

Chapter 6 is publication III: Loewer, M. and Igel, J. (2018): Multi-Pole Debye Description of Lossy and Dispersive Media for realistic FDTD Simulation of GPR, Geophysics, submitted.

The paper carries out GPR simulations, based on dielectric spectroscopy of different soils with respect to texture. The measured frequency-dependent electrical soil properties were implemented using a multi-Debye term decomposition and a FDTD code. The paper addresses the question, whether and to which degree simplified assumptions can be made with respect to the electrical parameter description of soils, and how big deviations in the simulation are in comparison to results in which the frequency-dependent properties were properly accounted for.

Chapter 7 gives an outlook on present and possible future work in regard to the thesis with potential applications and research topics with respect to the described findings.

2. Electromagnetic wave interaction with soils

The interaction of EM waves with soil can provide important information on its composition and state. Here, the response of a soil when exposed to an external field can be stored in varying physical quantities. In order to interpret the response properly, it is important to understand how the measured variables generally arise from the electrodynamics principles and how they compound. This chapter presents the fundamental physical equations from the EM theory and introduces effective parameters in the context of electrical parameter measurements of soils. It introduces the composition of a soil and the dependencies from thermodynamic state parameters. Furthermore, it analyses the frequency-dependent polarization and dielectric relaxation mechanisms of the individual components of the soil and the effects, which occur due to the interfaces of the different phases of the soil.

2.1. Electromagnetic theory

In the following the interaction of time-variant EM fields with matter is described. All formulas and models are based on classical electrodynamics and only refer to the wave nature of EM radiation. A particle- or quantum-physical description of the phenomena can be neglected in the frequency range of GPR, since all observable phenomena occur in a continuous manner.

2.1.1. Fundamental equations

The Maxwell's equations provide the mathematical framework to explain all EM phenomena in this study. In the form below, they describe the macroscopic behavior of electric and magnetic fields with respect to free charges and currents and their dynamic interaction with each other. An elaborate description of the fundamental equations can be found in Griffiths (1999) or Orfanidis (2013) and in more view of GPR in Powers (2001) or Knight and Endres (2005). The four Maxwell's equations are:

$$\nabla \cdot \mathbf{D} = \rho_f \tag{2.1}$$

$$\nabla \cdot \mathbf{B} = 0, \tag{2.2}$$

$$\nabla \times \mathbf{E} = -\frac{\partial \mathbf{B}}{\partial t} \tag{2.3}$$

$$\nabla \times \mathbf{H} = \mathbf{J}_f + \frac{\partial \mathbf{D}}{\partial t} \tag{2.4}$$

where all vectors depend on position and time. **E** and **H** are the electric and magnetic field strength, respectively. **D** and **B** are the electric and magnetic flux density[1]. $\mathbf{J}_f$ and ρ_f are the electric current density and the volume charge density of the free charges. Considering the four Maxwell's equations, no material-specific parameters like the electrical conductivity σ, the dielectric permittivity ε or the magnetic permeability μ appear. These parameters come into effect with the introduction of the medium in which the EM fields propagate. Therefore, the constitutive equations enables to establish a connection between cause and effect of the applied EM fields with respect to the medium. Therefore, the electric displacement **D** and the magnetic field strength **H** in equations 2.1 and 2.4 can equivalently be described using:

$$\mathbf{D} \equiv \varepsilon_0 \mathbf{E} + \mathbf{P} \qquad \text{and} \qquad \mathbf{B} \equiv \mu_0 (\mathbf{H} + \mathbf{M}), \tag{2.5}$$

in which **P** corresponds to dielectric polarization and **M** is the magnetization, or the mean electric and magnetic dipole moment per unity volume of the medium. The constant ε_0 and μ_0 are the vacuum dielectric permittivity and magnetic permeability. Assuming an isotropic medium and provided that the electric field **E** is not too strong (Griffiths, 1999), a proportionate or linear connection between the applied electric field **E** (cause) and the dielectric polarization **P** (effect) can be observed. Similarly for the relation between the applied magnetic field **B** and the strength of inducted magnetization **M**, and thus:

$$\mathbf{P} = \varepsilon_0 \chi_e \mathbf{E} \qquad \text{and} \qquad \mathbf{M} = \chi_m \mathbf{H}, \tag{2.6}$$

with permittivity $\varepsilon \equiv \varepsilon_0(1+\chi_e)$ and magnetic permeability $\mu \equiv \mu_0(1+\chi_m)$. The parameters χ_e and χ_m are the electric and magnetic susceptibility[2], or the material-specific electric and magnetic polarization. The requirement for a linear relationship between cause and effect is met, since the response of the EM material properties to an applied field is considered to be independent from the field-strength in the GPR method (Annan, 2009). Following constitutive equations arise:

$$\mathbf{J}_f = \sigma \mathbf{E} \tag{2.7}$$

$$\mathbf{D} = \varepsilon \mathbf{E} \tag{2.8}$$

$$\mathbf{B} = \mu \mathbf{H}. \tag{2.9}$$

[1] **D** and **B** are also often called electric displacement and magnetic induction

[2] The (volume-specific) magnetic susceptibility is often denoted by κ

The electric current density $\mathbf{J}_f$ given by Ohm's law (Eq. 2.7) linearly implicates the applied electric field $\mathbf{E}$. The electrical conductivity σ herein is a measure of the mediums ability to let free charges pass through its volume. The second equation (2.8) was derived by substituting the first equation in Eq. 2.5 into Ampère's law of Maxwell's equations 2.4. The dielectric permittivity ε describes the ability of a material to store energy by the displacement of charges in a restricted space or in a fixed molecular structure. Equations 2.8 and 2.9 result from substituting equations 2.6 in equations 2.5. Here, the magnetic permeability μ corresponds to the response of the molecular magnetic moments in a material to a magnetic field. Since both the dielectric permittivity ε and the magnetic permeability μ of most geological materials are quite small, measurements generally specify the parameters using relative values that are normalized by the value in vacuum:

$$\varepsilon_r = \frac{\varepsilon}{\varepsilon_0} \qquad \text{and} \qquad \mu_r = \frac{\mu}{\mu_0}, \tag{2.10}$$

where ε_r and μ_r are the relative dielectric permittivity and the relative magnetic permeability[3].

Considering the fourth Maxwell's equation (Eq. 2.4), a magnetic field $\mathbf{H}$ will be induced by the flux of free charged particles $\mathbf{J}_f$ (Ampère's law). The same however can occur through the time-variation, or the displacement of the electric flux density $\partial\mathbf{D}/\partial t$ (Maxwell's correction to Ampère's law), or equally valid through the introduction of a displacement current $\mathbf{J}_d = \partial\mathbf{D}/\partial t$ [in Ampère/m^2]. The sum is the total current and together with the constitutive equation 2.7 and 2.8 it yields:

$$\nabla \times \mathbf{H} = \mathbf{J_f} + \mathbf{J_d} = \sigma\mathbf{E} + \varepsilon\frac{\partial \mathbf{E}}{\partial t}. \tag{2.11}$$

The equation shows that the displacement current only appears in connection with time-varying electric fields, whereas the electric current can occur in both constant and time-varying fields. From a physical point of view, electric current causes energy losses in the form of heat, which is due to the collision of free moving charges with other particles in the medium. The displacement current in contrast, stores energy during the displacement of the bound charges in the time-varying field. The radiated EM energy now only propagates as waves as long as the displacement current is larger than the electric current. Otherwise the energy will propagate via diffusion and therefore, outside of the wave regime GPR would clearly fail.

[3] In literature the terminus dielectric constant is often found for ε_r. However, in the following chapters I will show that ε_r is not constant in complex materials like soils and I therefore favor to call ε_r relative dielectric permittivity.

2.1.2. Wave propagation in matter

The Faraday's law (2.3) and Ampère's law (2.4) in Maxwell's equations show the direct coupling of the time-variant magnetic field **H** and electric field **E** and vice versa, which implicates that these fields can propagate as waves. Fig. 2.1 illustrates that a time-variant electric current **J** on an antenna generates a circulating time-varying magnetic field **H**, which in turn due to Faraday's law (2.3) generates a circulating and time-varying electric field and due to Ampẽre's law (2.4) generates a magnetic field again. By doing so, the EM energy from GPR can propagate in the medium in the form of EM waves, until it dissipates into heat for instance. In order to mathemati-

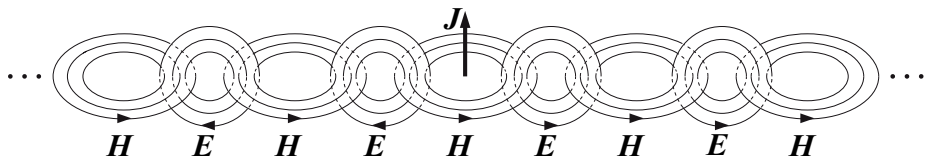

Fig. 2.1.: EM wave propagation on the basis of Maxwell's equations (2.3, 2.4) using alternating electric (**E**) and magnetic (**H**) fields that are initiated by a time-variant current of charged particles **J** (after Orfanidis, 2013).

cally illustrate that electric and magnetic fields propagate together as waves, one can substitute the constitutive equations (2.7-2.9) into Maxwell's equations (2.1-2.4) and assume that the only source of EM fields is concentrated in the antenna (i.e. the net free charge density ρ_f of the medium is zero; Griffiths, 1999) for a linear conductive medium one obtains:

$$\begin{aligned} &\text{(i)} \quad \nabla\cdot\mathbf{E}=0, \qquad &&\text{(iii)} \quad \nabla\times\mathbf{E}=-\frac{\partial\mathbf{B}}{\partial t},\\ &\text{(ii)} \quad \nabla\cdot\mathbf{B}=0, \qquad &&\text{(iv)} \quad \nabla\times\mathbf{B}=\mu\sigma\mathbf{E}+\mu\varepsilon\frac{\partial\mathbf{E}}{\partial t}. \end{aligned} \tag{2.12}$$

Taking the curl of (iii) and (iv) together with the identity $\nabla\times\nabla\times\mathbf{A}=\nabla(\nabla\cdot\mathbf{A})-\nabla^2\mathbf{A}$ yields:

$$\nabla^2\mathbf{E}=\mu\varepsilon\frac{\partial^2\mathbf{E}}{\partial t^2}+\mu\sigma\frac{\partial\mathbf{E}}{\partial t} \quad \text{and} \quad \nabla^2\mathbf{B}=\mu\varepsilon\frac{\partial^2\mathbf{B}}{\partial t^2}+\mu\sigma\frac{\partial\mathbf{B}}{\partial t}. \tag{2.13}$$

These equations have the typical form of wave equations for which an infinite number of solution exists. One solution for the EM wave equation is the rather complicated wave form of the GPR signal that propagates in the subsurface (Irving, 2000). Using Fourier analysis any complex signal can be split into a linear combination of sinusoidal waves with varying frequency. Therefore, taking a monochromatic plane wave assumption in the most simple case, the solutions for the electric and magnetic field vectors in Eqs. 2.13 are:

$$\mathbf{E}(z,t)=\mathbf{E}_0e^{i(\omega t-\gamma z)} \quad \text{and} \quad \mathbf{B}(z,t)=\mathbf{B}_0e^{i(\omega t-\gamma z)}, \tag{2.14}$$

where the vectors $\mathbf{E}$ and $\mathbf{B}$ depend on time t and depth z. $\mathbf{E}_0$ and $\mathbf{B}_0$ are the complex amplitudes of the fields and ω and γ are the angular frequency (with $\omega = 2\pi f$, with f being the frequency) and the propagation constant given by the dispersion relation:

$$\gamma^2 = \mu\varepsilon\omega^2 - i\mu\sigma\omega. \tag{2.15}$$

Here, the imaginary part of the propagation constant (2.15, 2.16) contains all information on the energy losses during wave propagation and the real part corresponds to the energy storage. Taking the square root of 2.15 gives:

$$\gamma = \zeta - i\alpha, \tag{2.16}$$

where

$$\zeta = \omega\sqrt{\frac{\mu\varepsilon}{2}\left(\sqrt{1+\left(\frac{\sigma}{\omega\varepsilon}\right)^2}+1\right)}, \qquad \alpha = \omega\sqrt{\frac{\mu\varepsilon}{2}\left(\sqrt{1+\left(\frac{\sigma}{\omega\varepsilon}\right)^2}-1\right)}. \tag{2.17}$$

The equations show that γ depends on frequency of the wave, as well as the constitutive parameters of the medium. Substituting 2.16 into 2.14 gives:

$$\mathbf{E}(z,t) = \mathbf{E}_0 e^{-\alpha z} e^{i(\omega t - \zeta z)} \quad \text{and} \quad \mathbf{B}(z,t) = \mathbf{B}_0 e^{-\alpha z} e^{i(\omega t - \zeta z)}, \tag{2.18}$$

which shows that the imaginary part of the wave number generates the attenuation (α in Np/m) of the EM waves and the real part corresponds to the phase coefficient (ζ in rad/m). The inverse of the attenuation is called *skin depth* and describes the depth in which the amplitude of the wave has decreased by the factor $1/e$:

$$\delta_s \equiv \frac{1}{\alpha}. \tag{2.19}$$

Similarly, phase velocity v [m/s] and wave length λ [m] of the EM wave can be calculated by the wave coefficient ζ via:

$$v = \frac{\omega}{\zeta} \quad \text{and} \quad \lambda = \frac{2\pi}{\zeta}. \tag{2.20}$$

2.1.3. Complex and effective properties

Eq. 2.17 shows that α generally increase with ω, independently from σ, ε or μ. Furthermore, if σ gets infinitely small, α approaches zero, whereas the v (given by Eq. 2.20) will only dependent on ε (for $\mu \approx 1$, which is the case for most soils).
However, the constitutive parameters σ, ε and μ also depend on frequency themselves. The frequency-dependence of the electrical parameters is relatively well-known for

dipolar liquids for example, like water, but it also applies to a wide range of solids (Jonscher, 1977) and especially to mixtures of both, like soils. The frequency-dependence of the constitutive parameters is commonly expressed using complex numbers (Knight and Endres, 2005):

$$\sigma^*(\omega) = \sigma'(\omega) + i\sigma''(\omega) \tag{2.21}$$

$$\varepsilon^*(\omega) = \varepsilon'(\omega) - i\varepsilon''(\omega) \tag{2.22}$$

$$\mu^*(\omega) = \mu'(\omega) - i\mu''(\omega). \tag{2.23}$$

Here, $\sigma'(\omega)$ and $\sigma''(\omega)$ correspond to carrier transport due to ohmic conduction and faradaic diffusion. $\varepsilon'(\omega)$ and $\varepsilon''(\omega)$ represents the dielectric relaxation due to a lag of polarization $\mathbf{P}$ behind the quickly changing electric field $\mathbf{E}$. Similarely, $\mu'(\omega)$ represents magnetization of bound magnetic currents and $\mu''(\omega)$ refers to losses thereof, in the form of magnetic relaxation due to the lag of magnetization $\mathbf{M}$ and the magnetic field $\mathbf{H}$ (Olhoeft and Capron, 1994; Knight and Endres, 2005). However, in most cases for GPR simplifying assumptions regarding the magnetic properties can be made, provided the soil is 'iron-free' and thus no considerable amounts of ferrimagnetic minerals are present in the soil (Cassidy, 2009). Since all soils in this thesis contained no considerable or in one case only small amounts of magnetic minerals (e.g. magnetite), we equate μ with the vacuum permeability μ_0 (the laterite in this thesis has the highest volume specific susceptibility of < 0.04 SI, which is clearly below the deployed threshold value of 0.3 SI as presented in Cassidy, 2009). Substituting the frequency-dependent constitutive parameters (2.21, 2.22) and the constitutive equation 2.9 into Maxwell's fourth equation (2.12 iv) and taking the Fourier transform of the equation with some reorganization, one receives:

$$\nabla \times \mathbf{H} = \left[\sigma'(\omega) + \omega\varepsilon''(\omega)\right]\mathbf{E} + i\omega\left[\varepsilon'(\omega) + \frac{\sigma''(\omega)}{\omega}\right]\mathbf{E}. \tag{2.24}$$

In this representation, it is obvious that the imaginary part of dielectric permittivity $\varepsilon''(\omega)$ contributes to the energy losses, whereas the imaginary part of conductivity $\sigma''(\omega)$ contributes to energy storage. However, using frequency-dependent measurement techniques, it is impossible to measure the individual contributions of $\varepsilon^*(\omega)$ and $\sigma^*(\omega)$ separately from each other. Therefore, effective parameters must be introduced (e.g. Knight and Endres, 2005), thus 2.24 becomes:

$$\nabla \times \mathbf{H} = \sigma_{eff}(\omega)\mathbf{E} + i\omega\varepsilon_{eff}(\omega)\mathbf{E}, \tag{2.25}$$

with

$$\sigma_{eff}(\omega) = \sigma'(\omega) + \omega\varepsilon''(\omega) \tag{2.26}$$

$$\varepsilon_{eff}(\omega) = \varepsilon'(\omega) + \frac{\sigma''(\omega)}{\omega}. \tag{2.27}$$

However, in dielectric and electric spectroscopy, the effective constitutive parameters (2.26 and 2.27) are commonly expressed by a single complex number, where the real part accounts for energy storage and the imaginary part for the losses. Therefore, they can be equivalently expressed as either complex effective dielectric permittivity:

$$\varepsilon^*_{eff}(\omega) = \varepsilon'_{eff}(\omega) - i\varepsilon''_{eff}(\omega) = \left[\varepsilon'(\omega) + \frac{\sigma''(\omega)}{\omega}\right] - i\left[\varepsilon''(\omega) + \frac{\sigma'(\omega)}{\omega}\right], \quad (2.28)$$

or by the complex effective electric conductivity:

$$\sigma^*_{eff}(\omega) = \sigma'_{eff}(\omega) + i\sigma''_{eff}(\omega) = \left[\sigma'(\omega) + \omega\varepsilon''(\omega)\right] + i\left[\sigma''(\omega) + \omega\varepsilon'(\omega)\right]. \quad (2.29)$$

Here, the effective parameters $\sigma'_{eff}(\omega)$ or $\varepsilon''_{eff}(\omega)$ correspond to ohmic conductance, whereas $\varepsilon'_{eff}(\omega)$ or $\sigma''_{eff}(\omega)$ correspond to capacitance, respectively.
Figs. 2.2 (a & b) show the general trend of ε_r and σ for most semi-conducting materials with respect to frequency. The spectra are divided by a critical frequency (f_{cr}) into two areas in which the material behaves either as a conductor or as a dielectric. The scheme indicates that this response can generally be observed independent from the frequency-dependence of the electrical properties themselves and therefore is found even when constant parameters for ε_r and σ are assumed (red and green lines). Assuming frequency-independent ε_r and σ, the complex relative permittivity can be defined as $\varepsilon^*_r = \varepsilon_r - i\frac{\sigma}{\omega\varepsilon_0}$ (Fig. 2.2 a) and the complex conductivity as $\sigma^* = \sigma + i\omega\varepsilon_0\varepsilon_r$ (Fig. 2.2 b). However, measured data for a silty clay loam Fig. 2.2 (c & d) show deviations from the straight lines, which indicates frequency-dependence of the dielectric and electrical parameters themselves, and therefore justifies the use of effective parameters. In the frequency-dependent response of soils above 100 kHz, the assumption is usually made that the imaginary part of conductivity $\sigma''(\omega)$ (faradaic diffusion) is negligible and that the real part $\sigma'(\omega)$ (ohmic conductance) is equivalent to the constant dc conductivity σ_{dc} (Powers, 2001; Knight and Endres, 2005). Since at high-frequencies dielectric permittivity prevails over electrical conductivity, we express both energy losses and energy storage, normalized by the vacuum permittivity ε_0, using the real and imaginary part of the complex effective dielectric permittivity using:

$$\varepsilon'_{r,eff}(\omega) = \frac{\varepsilon'_{eff}(\omega)}{\varepsilon_0} = \frac{\varepsilon'(\omega)}{\varepsilon_0} + \frac{\sigma''(\omega)}{\varepsilon_0\omega}, \quad (2.30)$$

$$\text{for f >100 kHz:} \quad \frac{\sigma''(\omega)}{\omega} \ll \varepsilon'(\omega) \quad \Rightarrow \quad \varepsilon'_{r,eff}(\omega) = \frac{\varepsilon'(\omega)}{\varepsilon_0} \quad (2.31)$$

$$\text{and} \quad \varepsilon''_{r,eff}(\omega) = \frac{\sigma'_{eff}(\omega)}{\varepsilon_0\omega} = \frac{1}{\varepsilon_0}\left(\varepsilon''(\omega) + \frac{\sigma_{dc}}{\omega}\right), \quad (2.32)$$

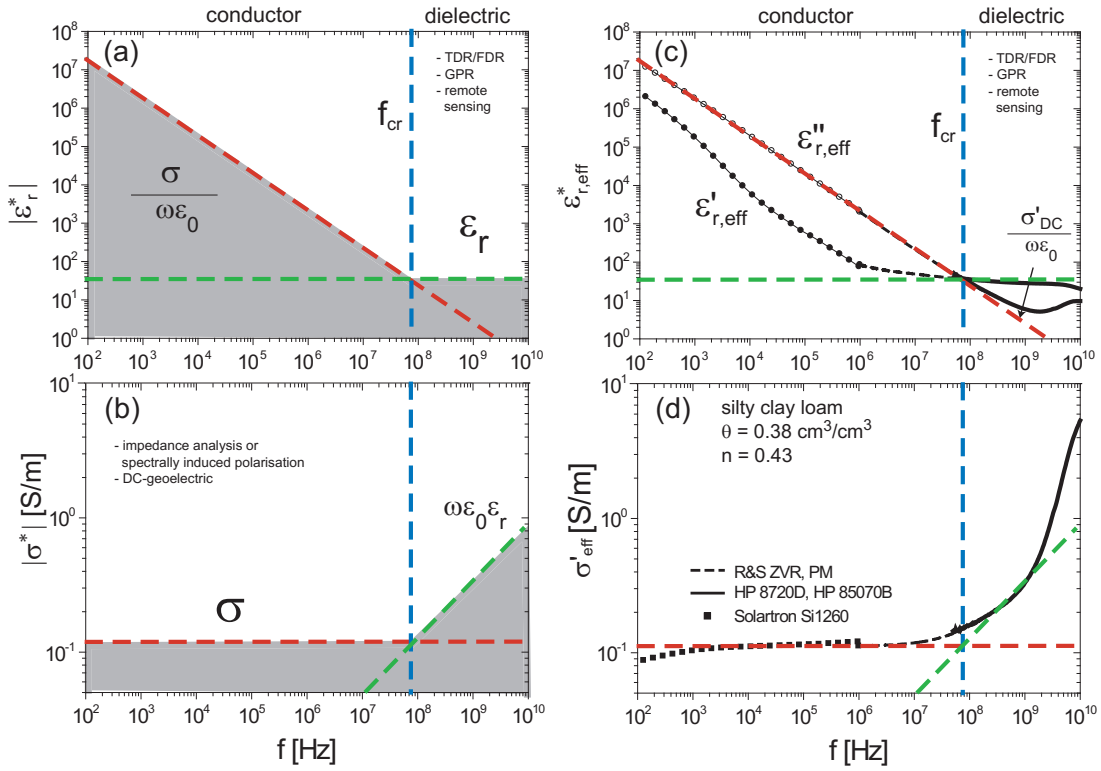

Fig. 2.2.: left (a & b): generalized frequency-dependent electrical response of a porous moist material described by constant parameters ε_r (green line) and σ (red line). The critical frequency f_{cr} divides the electrical response into conductor or dielectric (blue line). right (c & d): Measured frequency-dependent dielectric response of silty clay loam at 38% vol. water content and 43% porosity indicating the application of complex effective constitutive properties (modified from Wagner et al., 2011).

where the loss tangent $\tan\delta$ is defined as

$$\tan\delta = \frac{|\mathbf{J}_f|}{|\mathbf{J}_d|} = \frac{\sigma'_{eff}(\omega)}{\omega\varepsilon'_{eff}(\omega)} = \frac{\sigma_{dc} + \omega\varepsilon''(\omega)}{\omega\varepsilon'(\omega)} = \frac{\varepsilon''_{r,eff}(\omega)}{\varepsilon'_{r,eff}(\omega)}. \tag{2.33}$$

With respect to the presented scheme in Fig. 2.2, the medium becomes a conductor in case of $\tan\delta \gg 1$, meaning that the displacement current $\mathbf{J}_d$ is negligible against the conduction of free currents $\mathbf{J}_f$ (see Maxwell's correction to Ampère's law, Eq. 2.11). Similarly, the medium is a dielectric in case of $\tan\delta \ll 1$, when the displacement current $\mathbf{J}_d$ strongly prevails over the conduction current.

GPR clearly only works in the case of a dielectric medium, in case of $\tan\delta$ being smaller than 1. However, the transition zone between conductive and dielectric response of a soil can extend far into the GPR frequency range and strongly depend on moisture and texture of the soil. Furthermore, to which degree $\tan\delta$ needs to be smaller than 1 in order for GPR to work as a detection device, is strongly controlled by the depth of the aimed object or structure, the contrast to its surrounding soil and the applied GPR system (measuring frequency, dynamic range, antenna gain, etc.). Em-

bedding the newly defined effective parameters with all previously met assumptions into the attenuation and phase coefficient (2.17) yields:

$$\alpha = \frac{\omega}{c_0}\sqrt{\frac{\varepsilon'_{r,eff}(\omega)}{2}\left(\sqrt{1+\tan^2\delta}-1\right)} \tag{2.34}$$

$$\zeta = \frac{\omega}{c_0}\sqrt{\frac{\varepsilon'_{r,eff}(\omega)}{2}\left(\sqrt{1+\tan^2\delta}+1\right)}, \tag{2.35}$$

with the speed of light defined by:

$$c_0 = 1/\sqrt{\varepsilon_0\mu_0}. \tag{2.36}$$

Thus with Eq. 2.20 the phase velocity becomes:

$$v = c_0\left\{\sqrt{\frac{\varepsilon'_{r,eff}(\omega)}{2}\left(\sqrt{1+\tan^2\delta}+1\right)}\right\}^{-1}. \text{ For } \tan\delta \to 0: v = \frac{c_0}{\sqrt{\varepsilon'_{r,eff}}} \tag{2.37}$$

which either applies to non-lossy soils or which can be regarded as a high-frequency approximation (for f≈1 GHz). The attenuation describes the degree of decline of the signal amplitude in comparison to its initial value (cf. Eq. 2.18). It is usually expressed in decibel per meter [dB/m], which is approximately $8.686 \times \alpha$ in neper per meter [Np/m]. In order to confine the attenuation that is addressed in this thesis from another sort of attenuation (scattering attenuation), we use the term *intrinic* attenuation. Intrinsic means that the attenuation is caused by the inherent EM properties of the material in which the waves propagate. Fig. 2.3 shows schematically how intrin-

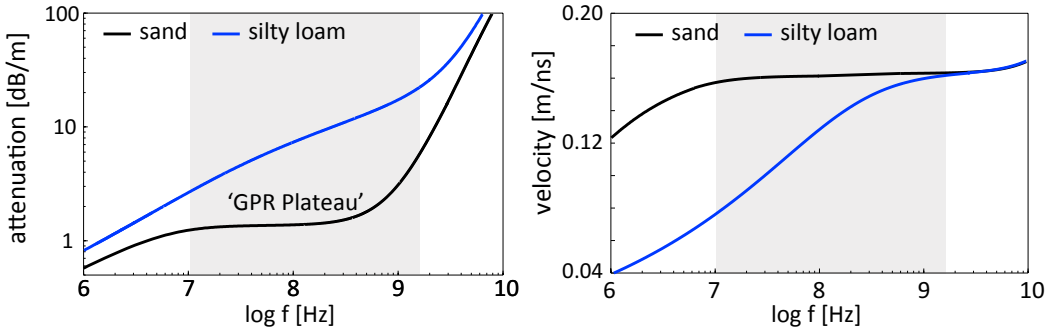

Fig. 2.3.: Comparison of the frequency-dependent intrinsic attenuation and phase velocity for sand (black line) and silty loam (blue line) at 15% volumetric water content. The grey shaded zone refers to the GPR frequency range.

sic attenuation and also velocity (given by Eqs. 2.37 & 2.20) can defer between two different soils at the same volumetric water content. For both soils attenuation and velocity generally increases with frequency. At GHz frequencies attenuation strongly

rises with frequency at approximately the same amount for both soils. However, the sand shows a 'plateau'-like frequency-independent part and relatively low attenuation and is constant in most of the velocity spectrum. This describes the ideal medium for GPR in which EM waves can propagate. In contrast, the silty loam is very dispersive in both spectra in most of the GPR frequency range (grey shaded area), which apart from the overall higher absorption rate causes low-pass filtering of the signals during wave propagation, since high frequencies are stronger attenuated than lower frequencies. In addition, phase velocity dispersion could lead to the distortion of the wavelet. Most soils in nature however, are somewhere between these depicted examples. Any possible reasons for increased attenuation and frequency-dependence of the finer-grained soil in contrast to pure sand is the basis of the next sections.

2.2. Soil composition

Looking at an ordinary organic free soil under the microscope, one can see a heterogeneous mixture of different phases (Fig. 2.4). These generally consist of solid mineral particles, liquid pore solution and air chambers that are mixed in varying portion and composition (Wagner and Scheuermann, 2009). In addition, most soils contain clay aggregates that provide large negatively charged surface areas, at which water can be adsorbed. Furthermore, at the interfaces of the mineral grains or clay aggregates and the liquid phase an electrical double layer (EDL) occurs, which allows cations and anions to diffuse along a concentration gradient (Revil, 2012). The single components of the soil have different constant or frequency-dependent electrical properties and therefore contribute to the overall electrical response in varying degrees. Apart from frequency, these parameters generally also depend on thermodynamic state parameters like water content, temperature and porosity or density (Wagner et al., 2011). The volumetric water content of the soil is calculated by (Behari, 2005):

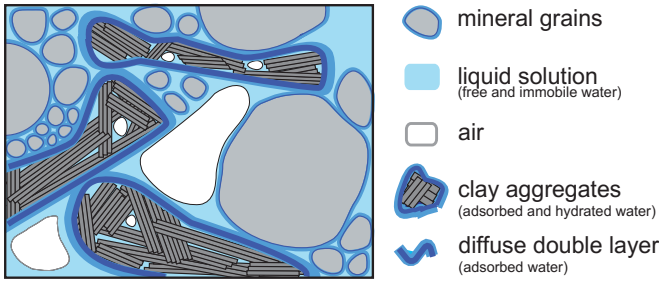

Fig. 2.4.: Simplified schematic illustration of the soil structure indicating the different contributions to the electrical response in an EM field (modified from Wagner and Scheuermann, 2009).

$$\theta_v = \frac{V_w}{V_b}, \tag{2.38}$$

where V_w and V_b are the volume of water and the bulk volume of the soil (in cm^3). In case of electric spectroscopy using moist soil samples, the bulk volume V_b corresponds

to the volume of the measuring cell that is completely filled by the soil sample. However, in case of in-situ samples with unknown water content, the volume of the water part V_w is unknown. Therefore, θ_v is calculated using the gravimetric water content θ_g by means of the sample weights and the component densities:

$$\theta_v = \theta_g \frac{\rho_b}{\rho_w} = \frac{m_w}{m_d} \frac{\rho_d}{\rho_w}, \tag{2.39}$$

where ρ_b and ρ_w are (dry) bulk density and the density of water (ρ_w=1 g/cm^3). m_w and m_d are mass of the water part and the mass of the dried sample. The bulk density is given by

$$\rho_b = \frac{m_d}{V_b}, \qquad \text{and thus} \qquad \theta_v = \frac{m_w}{\rho_w V_b}. \tag{2.40}$$

Porosity ϕ is defined by the pore volume divided by the bulk volume of the soil sample:

$$\phi = \frac{V_a + V_w}{V_b} = 1 - \frac{\rho_b}{\rho_m}, \tag{2.41}$$

where V_a and ρ_m is the volume of air and the density of the grain minerals. The latter can be measured using a pycnometer and often can also be estimated based on the mineral composition of the soil determined by x-ray diffractometry (e.g. for quartz-rich soils $\rho_m = 2.65$g/cm^3 is a reasonable approximation).

These properties can have a strong influence on the EM wave propagation since they determine the structural composition of the soil. However, the interaction of EM waves with the individual soil components is very divers, as will be discussed in the next section.

2.3. Polarization and loss mechanisms in soil

In section 2.1.2 it was indicated that the ratio of conduction to displacement current controls wave propagation and that both, electrical conductivity and dielectric relaxations are responsible for intrinsic losses of the GPR signal during wave propagation in soils. Therefore, with respect to the properties of a particular soil and the frequency of the applied GPR system, EM wave propagation strongly varies. The example of measured dielectric data for a soil as shown in Fig. 2.2 (b, c) demonstrated which electrical process (charge transport, polarization, etc.) prevails at which frequency. Even so the general trend remains similar, these spectra differ for each individual soil in nature. Furthermore, the spectra do not explain their physical cause. In order to understand the response of the overall electric soil spectrum one has first to analyze the response of individual soil components in the EM field.
The propagation of electromagnetic waves in air occurs at the speed of light, which

suggests that the dielectric permittivity corresponds to the electric field constant[4]. The main components of air (nitrogen & oxygen) are non-polar molecules and due to the entropy of gases, the density of polar molecules like in liquid droplets is relatively low. Due to the low attenuation of the EM waves at radio frequencies extreme ranges can be reached in air (e.g. over-the-horizon (OTH) radar systems at 3-30 MHz can reach thousands of kilometers (Galati, 2016)). This is in strong contrast to the wave propagation in other media, most of all for water. In the following, the underlying physical processes are briefly described, which can generally lead to strong polarization and relaxation mechanisms in the GPR frequency-range.

2.3.1. Dipolar orientational polarization of water

The liquid pore solution in soil is water with dissolved salts. What directly stands out when observing the dielectric spectrum of water (see Fig. 2.5) is its relatively high dielectric permittivity in comparison to other pure substances. For frequencies below 2-3

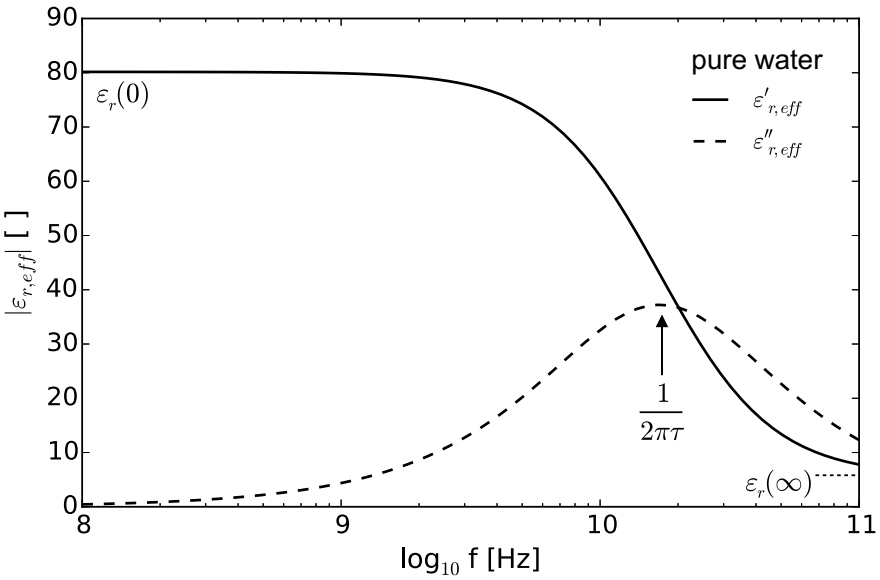

Fig. 2.5.: Real- and imaginary part of the normalized effective dielectric permittivity of pure water (data from Kaatze, 2000) at 20 ^{o}C ($\varepsilon_r(0)$ =80.16, $\varepsilon_r(\infty)$ =5.7 and τ =9.37 ps). The arrow point to the characteristic relaxation frequency.

GHz the real relative permittivity of water is constant with values around 80 at 20°C and at atmospheric pressure. In contrast, dry soils have values of permittivity between 2-6 and air has a value 1 (Cassidy, 2009). At the HF-range, the soil water content generally strongly determines the bulk dielectric permittivity of a soil and vice versa. This

[4]There can be a negligibly small offset between the vacuum permittivity and the permittivity in air due to humidity

relation is commonly used for soil moisture measurements in the field using EM technique, for example like Time-domain reflectometry (TDR; see section 3.3). Fig. 2.6 shows the relation between effective permittivity (Eqs. 2.30, 2.32) and the volumetric water content for different soils, which were measured at 1 GHz frequency using the coaxial transmission line (CTL) technique. The dielectric permittivity increases with the water content for all soil. However, its slope varies between the soils and different regression curves have been formulated in the past in order compensate for a particular soil type. One regression curve for mineral soils that was formulated by Topp et al. (1980) can be seen in Fig. 2.6 together with the value margin ranges of his measured data (Rubincon SL & Bainsville CL; shaded zone). The regression curve follows the equation $\varepsilon'_{r,eff} = 3.03 + 9.3\theta_v + 146\theta_v^2 - 76.7\theta_v^3$.
However, considering the dielectric spectrum of pure water in Fig. 2.5, the real dielectric permittivity starts to decrease above frequencies of $\approx$ 3 GHz and seems to converge to a lower plateau beyond 100 GHz. The two numbers, $\varepsilon_r(0)$ and $\varepsilon_r(\infty)$,

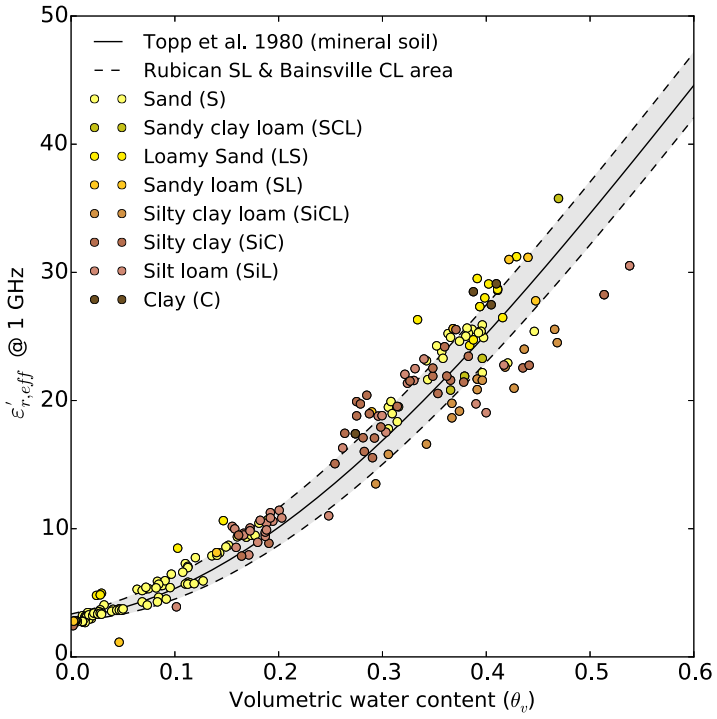

Fig. 2.6.: Dielectric permittivity (measured at 1 GHz frequency) versus water content for different soils classified after their texture class (defined after USDA, 1987, see Fig. 6.2). The grain size disribution curve of the measured data can be found in Fig. A.1. Regression curve after Topp et al. (1980).

which indicate the high and low dielectric permittivity limits are called the static and high-frequency permittivity (Kaatze, 2000). In contrast to the real part, the imaginary effective dielectric permittivity, which corresponds to the electrical losses, strongly rises and reaches a maximum at the inflection point of the real part. This relaxation pattern of the complex dielectric permittivity was first described in the formulation by

Debye (1913) as:

$$\varepsilon_r^*(\omega) = \varepsilon_r(\infty) + \frac{\varepsilon_r(0) - \varepsilon_r(\infty)}{1 + i\omega\tau}, \tag{2.42}$$

where τ corresponds to the characteristic relaxation time. Real and imaginary part of ε_r^* are given by:

$$\varepsilon_r'(\omega) = \varepsilon_r(\infty) + \frac{\varepsilon_r(0) - \varepsilon_r(\infty)}{1 + (\omega\tau)^2} \quad \text{and} \quad \varepsilon_r''(\omega) = \frac{\varepsilon_r(0) - \varepsilon_r(\infty)\omega\tau}{1 + (\omega\tau)^2}. \tag{2.43}$$

The characteristic relaxation frequency can be calculated by:

$$f_c = \frac{1}{2\pi\tau}. \tag{2.44}$$

Molecular structure of water

Water consists of polar molecules made of 2 hydrogen and 1 oxygen atom that build a regular tetrahedron. The oxygen atom is in the middle of the tetrahedron and the four vertices consist of the two positively charged hydrogen atoms and two negatively charged electron pairs (Kaatze, 2015). This non-uniform electric charge distribution of the water molecule creates a permanent electric dipole moment. When an electric field is applied the dipoles tend to re-orientate themselves in the direction of the field lines. However, each molecule is embedded in a dense water molecule network. The negatively charged ends of each molecule bind to the hydrogen atoms of neighboring water molecules via hydrogen bonds, which in turn tend to form localized tetrahedral structures (Fig. 2.7a). Here, the number of neighbors each molecule binds divers between the molecules and depends on the thermodynamic state of the substance. For instance, ice shows the highest probability density of molecules that bind exactly four neighboring molecules by hydrogen bond (Kaatze, 2015). Liquid water, in contrast shows a higher diversity with 4 or 5 bonding partners in most cases. In the wait-and-switch relaxation model, the structures generally restrict the reorientation of single water molecules until an appropriate defect exists (e.g. orientational deviations due to thermal fluctuations or ionic defects) and when a suitable new hydrogen or electron bond partner (a '5th neighbor') exists (Kaatze, 2015; Popov et al., 2016, see Fig. 2.7b). The

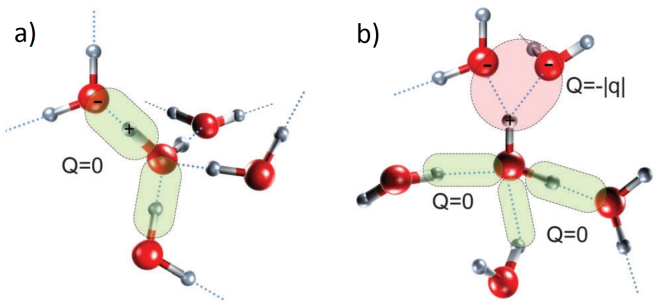

Fig. 2.7.: (a) local tetrahedral ordering of water molecules (red: oxygen, white: hydrogen) without defects and with zero net charge of normal hydrogen bonds (green shaded area). (b) The defect of hydrogen bond network with a negative charge associated with the bifurcated hydrogen bond (pink shaded area; from Popov et al., 2016).

waiting period until the switching to the new bonding neighbor and the subsequent reorientation process can occur is embodied in the relaxation time τ; or with other words, the relaxation time is the average life-time of the bulk hydrogen-bonds. Since the number of defects and potential bonding partners in liquid water is relatively high, the waiting period for the switch is relatively short, with relaxation times in the pico-second range (in comparison to ice with relaxation times in the micro-second range). So, for lower frequencies and longer time periods, the switching between different dipole directions of the molecules occurs within the time-frame of each circle, since there is sufficient time to overcome the potential energy barrier and to break the hydrogen bonds. However, when the frequency becomes too high, the time period between each reversal of the applied electric field is too short to reach this energy level. For water, frequencies of above $\approx$ 1 GHz create an increasing phase shift between the electric field and the polarization of the molecule, since the bulk of molecules become increasingly unable to follow the fast time-varying field. Considering the Debye equation (2.42, 2.43), ε_r' corresponds to the in-phase part and ε_r'' carries the information of the part which is out of phase. The interaction of the lagging dipoles in the hydrogen bonding network with the field creates losses due to heat, which are maximum at the relaxation frequency.

Temperature-dependence

The energy level, which is necessary to overcome the bonding forces is called activation enthalpy $\Delta H^{\#}$ and generally decreases with increasing temperature. Thus, the relaxation time and therefore all aspects of the relaxation itself are temperature-dependent phenomena. According to the Eyring relation the relaxation time under atmospheric conditions can be calculated by (Kaatze, 2000; Wagner and Scheuermann, 2009):

$$\tau(T) = \frac{h}{k_B T} k_t \exp(\Delta G^{\#}/RT), \tag{2.45}$$

where h, k_B and R are the Planck, Boltzmann and the gas constant, k_t is a transmission coefficient ($\approx$ 1) and the enthalpy of activation or the Gibbs free energy $\Delta G^{\#}$ is given by $\Delta G^{\#} = \Delta H^{\#} - T\Delta S^{\#}$. Here, $\Delta S^{\#}$ corresponds to the activation entropy of water. At room temperature (T=298.15 K) the activation enthalpy $\Delta H^{\#} = 16.4$ kJ/mol and activation entropy $\Delta S^{\#} = 20.4$ J/(K mol) (Buchner et al., 1999). Inserting these values into Eq. 2.45 reveals that water has a relaxation time of $\tau_w \approx 9.3$ ps ($f_r = 17$ GHz) at room temperature and under atmospheric pressure. The temperature-dependence of water can also be incorporated into a Debye model using the non-linear regression analysis of measured data in a temperature range between 0 and 50 °C as shown in Kaatze (1989), where:

$$\varepsilon_r(0,T) = 10^{1.94404 - 1.991 \cdot 10^{-3} K^{-1}(T - 273.15K)} \tag{2.46}$$

$$\varepsilon_r(\infty, T) = 5.77 - 2.74 \cdot 10^{-2} K^{-1}(T - 273.15K) \tag{2.47}$$

$$\tau(T) = 3.745 \cdot 10^{-15} s(1 + (7 \cdot 10^{-5} K^{-2}(T - 300.65K)^2) \exp^{\frac{2.2957 \cdot 10^3 K}{T}} \tag{2.48}$$

The energy losses in pure water are solely due to dielectric relaxation effects and reach a maximum at the characteristic relaxation frequency f_r. Apart from the dielectric re-

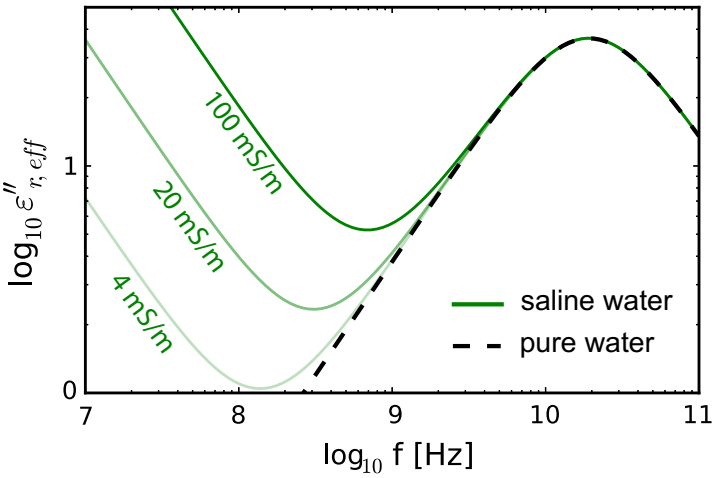

Fig. 2.8.: Imaginary effective dielectric permittivity of saline water for 3 different electrical conductivities in comparison to pure water.

laxation of water at around 17 GHz (at 20°C), there is another inferior relaxation mechanisms for water that can also be described using a Debye relaxation model (Buchner and Hefter, 2009). However, the relaxation is only effective at low Infrared frequencies (>300 GHz) and therefore far above the considered maximum frequency of this thesis. Other resonant-type mechanisms that are due to intermolecular vibrations are centered at even higher frequencies in the far-infrared frequency range (>1 THz; Fukasawa et al., 2005). Beyond that, in the ultraviolet frequency range (>750 THz) the electronic polarization occurs, which is based on the displacement of the negative electron cloud from the positive core in the atoms (Santamarina et al., 2001).

Electrical conductivity in saline water

In contrast, saline water (e.g. ground water) contains ions that flow in the direction of the applied external electric field. The conduction current of the free ions is constant and determines the quasi direct current electrical conductivity σ_{dc} of water. The dielectric permittivity losses ε'' together with σ_{dc} determine the imaginary part of the effective dielectric permittivity as given in Eq. 2.32. In the Debye equation the losses due to the electrical conductivity of the water can be incorporated by adding another loss term:

$$\varepsilon^*_{r,eff}(\omega) = \varepsilon_r(\infty) + \frac{\varepsilon_r(0) - \varepsilon_r(\infty)}{1 + i\omega\tau} - i\frac{\sigma_{dc}}{\varepsilon_0 \omega}. \tag{2.49}$$

Fig. 2.8 shows the influence of σ_{dc} on the loss part of the complex effective dielectric permittivity in saline water in comparison to pure water. The losses due to σ_{dc} (green lines) prevail over the losses due to the dielectric relaxation effect of pure water (dashed black line) at frequencies below $\approx$ 1 GHz and generally increase inversely with frequency.

2.3.2. Polarization due to interfaces

The mixture of all single components that build a soil (mineral grains, liquid solution, clay aggregates, air), as described in section 2.2 leads to further polarization and dielectric relaxation effects, which are attributed to the interfaces between the different component phases. Therefore, for soils with a large specific surface (e.g. clay), these effects can be especially pronounced. Furthermore, water can also be intercalated between clay layers and create hydrated minerals (Sposito et al., 1999). Also low-specific surface soils (e.g. silty sand) can show polarization mechanism that are due to differences of the conductivity and polarizability of the components, which leads to charge accumulation at interfaces (Santamarina et al., 2001).

Physically Bound water

Physically bound water[5] layers build up at the fluid-solid interfaces. The adsorbed water molecules are subject to van der Waals surface forces and hydrogen bonding to the predominately negatively charged surfaces of the clay mineral particles in the diffuse electrical double layer (EDL) (Pachepsky et al., 1996; Teschke et al., 2001; Wagner and Scheuermann, 2009). The bound molecules also underlie dielectric relaxation in the time-variant electric field, as observed for the free water molecules. However, the polarizability of absorbed water is lower than the polarizability of free water and the bonding forces between water and soil exists at a lower energy state than that of free water. Here, the matric potential is suggested as a measure of these bonding forces. Wagner and Scheuermann (2009), Wagner et al. (2013) and Schwing (2015) analyzed in theoretical and experimental investigations the relationship between the hydraulic properties and the frequency-dependent dielectric response of a soil.
In contrast to free water, bound water molecules are tightly bound to the solid surfaces, which prevents them to rotate freely. The effect is restricted to the closest two or three water layers and therefore primarily plays a role at high-specific surface soils (Santamarina et al., 2001). Bockris et al. (1963) differentiated between two mechanisms that both cause dielectric relaxations with respect to bound water layers in the vicinity of a mercury electrode surface (Wagner and Scheuermann, 2009): in the 'desorptive relaxation', bound water molecules in the first or second layer switch into vacancies of the second or third layer due to thermal desorption. In contrast,

[5] in contrast to chemically bound crystalline water

the 'rotational relaxation', which is similar to the relaxation of free water is limited to the first layer alone. Here, with increasing proximity of the water layer to the surface, an increasing activation enthalpy $\Delta H^{\#}$ is required in order to overcome bonding forces. The activation enthalpy of bound water and therefore also Gibbs free energy $\Delta G^{\#}$ is assumed to be higher than that of free water, which explains that the characteristic relaxation frequencies is shifted to lower frequencies: i.e. to break the bonds of absorbed water and in order to switch and re-orientate, longer time periods are required. Or and Wraith (1999) established the following empirical relation for the free activation energy between the distance d of absorbed water molecules to the particle surface of swelling clays:

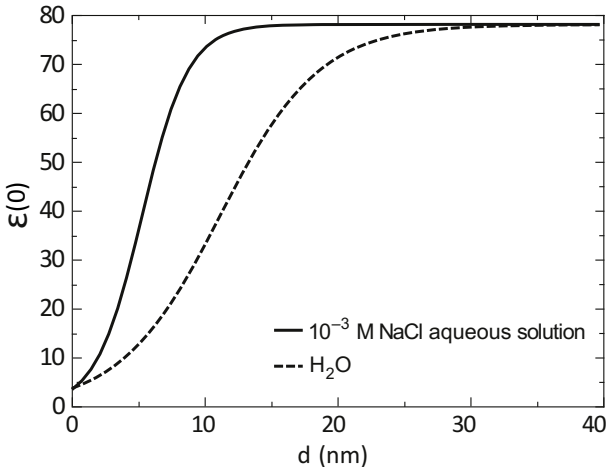

Fig. 2.9.: Static relative dielectric permittivity as a function of distance from a mica particle surface saturated by pure water (H_2O with $\varepsilon_f(0)$ =79, $\varepsilon_p(0)$ =3.8, λ = 15nm) and an aqueous electrolyte solution (NaCl with $\varepsilon_f(0)$ =79, $\varepsilon_p(0)$ =3.7, λ =6.9 nm). Fitting curves and data from Teschke et al. (2001); Wagner and Scheuermann (2009).

$$\Delta G_d^{\#}(d,T) = \Delta G_w^{\#}(T) + \frac{a_{ow}R}{d}, \tag{2.50}$$

where $\Delta G_w^{\#}$ is the free activation energy of free water and a_{ow} is an empirical constant (a_{ow} = 1261 Å· K). The static permittivity $\varepsilon(0)$ is lower in comparison to free water and also depends on the distance of the water layer to the surface. According to Teschke et al. (2001) it can be calculated assuming the distance from a mica particle surface as:

$$\varepsilon(0,d,T) = \frac{\varepsilon_f(0,T)}{1+\left[\frac{\varepsilon_f(0,T)}{\varepsilon_p(0,T)}-1\right]\exp(-\frac{2d}{\lambda})}, \tag{2.51}$$

where d is the distance from the particle surface, which can be related to the volumetric water content θ_v, the soil bulk density ρ_b and the specific surface area S_{sp} using $d = \theta_v/(S_{sp}\rho_b)$ (Wagner and Scheuermann, 2009). $\varepsilon_f(0,T)$ and $\varepsilon_p(0,T)$ are the static permittivity of free water and that of the particle surface and λ is the wave length of the EM field. Fig. 2.9 shows the static dielectric permittivity of pure water and an aqueous electrolyte solution with the distance from mica particles as described in Teschke et al. (2001) and Wagner and Scheuermann (2009). It can be observed that the static permittivity decreases in saline water considering a particular distance to the particle surface. Boyarskii et al. (2002) introduced a semi-empirical model that allows to consider the bound water relaxation in the examination of the dielectric response of different soils. Based on his experiments with relaxation times he suggests that after a distance of 10 water molecule layers from the particle surface, water can be regarded

as free water with a relaxation time τ_w of 7.7 ps at 27°C. With decreasing distance of the molecule from the surface, the relaxation time increases. Thus, bound molecules in the first two layers from the particle surface show relaxation times τ_{bw} between 50 ps and 500 ps (corresponding to frequencies between 320 MHz and 3.2 GHz).

Maxwell-Wagner effect

The Maxwell-Wagner effect (MWE), or sometimes called Maxwell-Wagner-Sillars effect also refers to polarization and relaxation mechanisms. However, it does not describe an orientational relaxation as that of the dipole molecule, but a polarization due to separation and accumulation of free charges at barriers in the migration path, which is generally at the interface between particles and the solution. Due to different particle and intrusion sizes, this spatial relaxation effect can develop at different scales and generally also occurs in soils with low-specific surface (Santamarina et al., 2001), and thus e.g. clay-free sandy soils or sedimentary rocks. The MWE occurs in any medium with at least two phases of different conductivity and polarizability. It is named after the work of Maxwell (1881) and Wagner (1913) who first solved complex permittivity equations for layered media and dispersed inclusion (Santamarina et al., 2001). It also serves as a general term for a set of different mixture models that describe the spatial polarization phenomena for varying geometries. The Maxwell relaxation alone for instance, describes the relaxation of layered media with different permittivity, which are immersed in a solution and which are oriented perpendicular to the applied field. The Wagner effect in contrast, describes the case where the solid phase is the host medium, which contains low-specific surface inclusions. For spherical particles with low volume fraction (d_2<0.2) the complex dielectric permittivity of the mixture model that describes the MWE is given by (Santamarina et al., 2001):

$$\varepsilon^*_{mix} = \frac{2\varepsilon^*_1 + \varepsilon^*_2 + 2d_2(\varepsilon^*_2 - \varepsilon^*_1)}{2\varepsilon^*_1 + \varepsilon^*_2 - d_2(\varepsilon^*_2 - \varepsilon^*_1)}\varepsilon^*_1, \qquad \tau = \frac{2\varepsilon'_1 + \varepsilon'_2 - d_2(\varepsilon'_2 - \varepsilon^*_1)}{2\sigma_1 + \sigma_2 - d_2(\sigma_2 - \sigma_1)}\varepsilon_0. \tag{2.52}$$

Here, d_1 and d_2 correspond to the volume fraction of host medium and spherical particles. ε^*_i, ε'_i and σ_i refer to the complex permittivity, real relative permittivity and conductivity of the host or the particle. This equation predict a Debye relaxation that can be rewritten using Eq. 2.49 (Santamarina et al., 2001). According to Cassidy (2009), the effect accounts for very high values of the complex effective permittivity especially at frequencies <1 MHz, but must also be considered in low-frequency GPR applications in case of fine-grained saturated materials. For soils, a distribution of MWEs is expected.

Electrical double layer polarization

The diffuse electrical double layer (EDL) builds on top of the negatively charged mineral surface in moist soils. It consist of the inner compact layer, the Stern layer (Stern,

1924) and an outer diffusive layer (Gouy, 1910; Chapman, 1913) with counter-ions and co-ions in the pore solution near the mineral to water interfaces. Here, the number of counter-ions equals the number of surface charges and generally decreases with increasing distance from the surface (Wagner and Scheuermann, 2009). Apart from the dipole relaxation of bound water, which also takes place in the EDL, two mechanisms can be described that are controlled by the restricted movement of the counter-ions. The Stern layer polarization arises due to the restricted movement of sorbed counter-ions adjacent to the particle surface and allow local movements in the presence of structural surface charges (Santamarina et al., 2001). The counter-ions in the diffusive layer in contrast can move further from the surface, but are linked to the mineral surfaces by the Coulomb interaction (Leroy and Revil, 2009). In the electric field, the double layer polarization arises due to the relative displacement of the whole double layer counter-ion cloud with respect to the charged particle. These polarization effects are especially distinct in the case of conductive pore water and in case of soils containing swelling clay minerals with high cation-exchange capacities. Leroy and Revil (2009) suggests that low-frequency dispersion phenomena in clays in the 1 Hz to 1 MHz frequency range can be strongly controlled by the Stern layer polarization, but that this phenomenon can overlap with the Maxwell-Wagner effect.
Furthermore, Rotenberg et al. (2005) suggest a model that accounts for cation diffusion in the inter-layer gallery of clay and possible adsorption/reaction at the clay surface. The model is suggested to explain the ionic contribution to the effective permittity for compacted clay and the relaxation behavior in the MHz-GHz frequency range in addition to the relaxation of physically bound water.

The Cole-Cole relaxation model

The complex dielectric permittivity of pure water describes a relaxation in the microwave range (see Fig. 2.5), which can be described by a single Debye relaxation (Eqs. 2.42, 2.43). In case of saline water the dielectric losses can be complemented by adding a dc-conductivity term to the model, as demonstrated in Eq. 2.49 and Fig. 2.8, respectively. However, for mixtures like soil the Debye model is too simple in order to describe the polarizations, which are due to the many interfaces. In order to compensate for that Cole and Cole (1941) introduced a stretching factor ($\beta = 1 - \alpha$), which enables to generalize the Debye model as:

$$\varepsilon^*_{r,eff}(\omega) = \varepsilon_\infty + \frac{\triangle\, \varepsilon}{1 + (i\omega\tau)^{1-\alpha}} \tag{2.53}$$

with $0 \leq \alpha < 1$ and where the relaxation strength $\triangle\, \varepsilon = \varepsilon_r(0) - \varepsilon_r(\infty)$. The Cole-Cole model can be interpreted as as sum of Debye models with different relaxation times.

3. Methods

The chapter introduces the main geophysical methods that were used throughout the thesis in order to assess the frequency-dependent EM response of soils and their influence on ground-penetrating radar (GPR). All methods generally cover different frequency ranges and measure either in time- or in the frequency-domain. Here, GPR and dielectric spectroscopy, by means of the coaxial transmission line technique (CTL), are the main focus of the thesis from a methodological perspective. The time-domain reflectometry (TDR) principle is also briefly described and for the spectral-induced polarization (SIP) we refer to a detailed description as given in Kruschwitz (2008). Fig. 3.1 shows the frequency-range of the methods together with the effective electrical parameters (real effective dielectric permittivity $\varepsilon'_{r,eff}$ and real effective conductivity σ'_{eff} as given in Eqs. 2.28 and 2.29) for a fine-grained soil. According to Revil (2013) the frequency-dependence of the electrical properties in the considered frequency range are mainly due to the double layer polarization, interfacial polarization and the dipolar polarization.

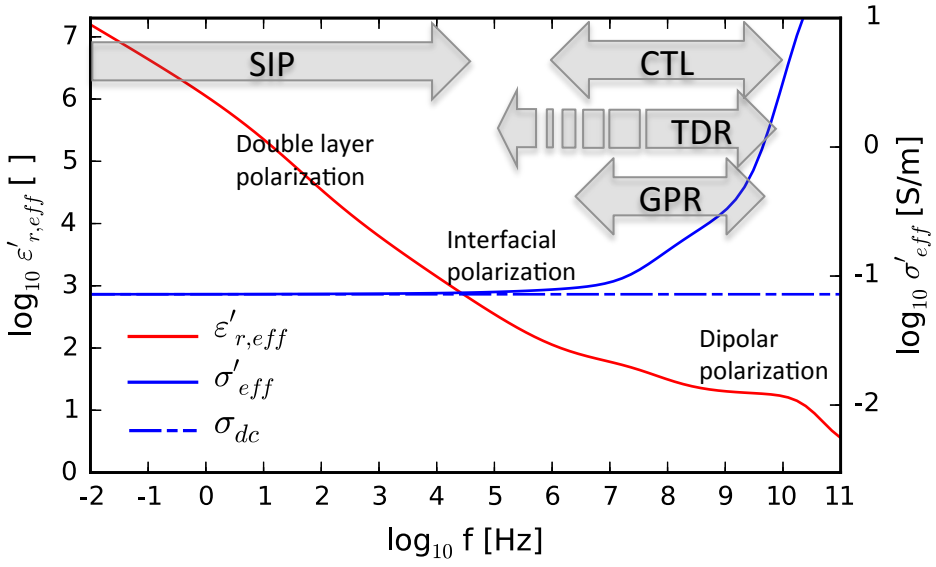

Fig. 3.1.: Real effective permittivity (red line) and conductivity (blue line) spectrum of soil indicating the frequency range of measuring methods (SIP, CTL, TDR and GPR) and polarization effects (after Revil, 2013).

3.1. Ground-penetrating radar

Ground-penetrating radar (GPR) is a non-destructive geophysical technique, which uses reflections of transmitted radio waves in order to probe structures in the subsurface. The very first applications and patents for subsurface soundings using EM waves were carried out by Leimbach and Löwy in 1910 in order to investigate ore layers using dipole antennas of different size (Ambronn, 1926). The first impulse device for subsurface sounding of structures was patented in 1926 by the Dr. Hülsenbeck & Co. enterprise and serves as a very early precursor for the present-day GPR. Hülsenbeck pointed out that apart from the possibility to measure electrical conductivity, any dielectric change in the subsurface will create reflections of EM waves (Daniels, 1996). However, a breakthrough of GPR with starting commercialization was not achieved until the 1970s (Francke, 2014). Some early application areas comprised the measurements of arctic ice shields (Cook, 1960), ice and permafrost thicknesses (Annan and Davis, 1976; Davis et al., 1976) as well as cavity detection (Morey, 1974) and mining (Cook, 1973; Tierbach, 1974). Since then, the application areas were permanently expanded. Nowadays, GPR is frequently used in the fields of civil and geotechnical engineering (Saarenketo and Scullion, 2000; Yelf, 2007; Francke, 2014), sedimentology (Lang et al., 2017), geology, groundwater hydrology (Igel et al., 2013a) as well as for environmental engineering, such as for landmine and UXO detection (Takahashi et al., 2011; Igel et al., 2013b).

3.1.1. Principle and setup

In order to produce EM waves a signal generator is used, which sends the generated high-frequency pulses to a transmitter antenna (Tx; Fig. 3.2) using glass fiber or coaxial cables. The antenna radiates the pulses in form of EM waves into the ground. In order to achieve sufficient ground coupling of the EM energy, the GPR antennas are located within a preferably small distance to the ground surface. Furthermore, high-frequency antennas (>100 MHz) are generally shielded to the upside in order to avoid the radiation of energy away from the ground (Annan, 2009). In the subsurface the waves generally propagate with reduced velocity and under the influence of attenuation. At dielectric contrasts (impedance contrasts) the waves get reflected back to the surface were they are recorded using a receiver antenna (Rx; Fig. 3.2). The received signals are transmitted to a control unit were they can get stored and displayed in forms of (un-processed) radargrams. In order to achieve a 2-D image of the underground, transmitter and receiver antenna are pulled across the ground during the recording. Traces are recorded in a certain time window after each incremental step along the survey line, which is triggered by a survey wheel (see Fig. 3.2). Thus, a 2-D profile (B-scan) is basically a lineup of traces that had been recorded for a certain

survey distance.

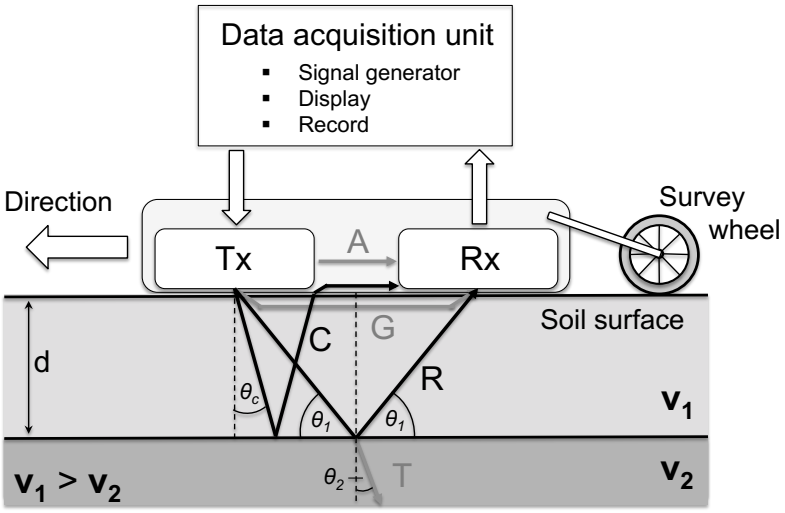

Fig. 3.2.: Overview of the main components of a GPR system and the signal paths between transmitter (Tx) and Receiver (Rx) antenna with respect the wave propagation in two planar soil layers with varying velocities v_1 and v_2 (A: direct air wave; G: direct ground wave; R: reflected wave; C: reflected & critically refracted wave; T: refracted wave; modified from Annan, 2009).

The transmitted GPR signals in the ground can generally be divided into spherical waves and a planar wave front, which travels at a critical angle θ_c (Annan, 2009). The direct wave A traveling through air between transmitter and receiver and the ground wave G traveling directly under the surface become indistinguishable from the air-ground reflection, when the distance between transmitter and receiver is very small. In most conventional GPR systems the receiver antenna is installed directly next to the transmitter antenna (common offset method). The ray path of the EM waves generally underlies all known optical principles. Assuming an impedance contrast between two soil layers in the subsurface, all travel directions of the incident (I), reflected (R) and transmitted (T) waves are governed by Snell's law (Annan, 2009), as:

$$\frac{\sin\theta_1}{v_1} = \frac{\sin\theta_2}{v_2}, \tag{3.1}$$

where θ_1 is the angle of the incident ray path in the medium with velocity v_1 and θ_1 corresponds to the angle of the refracted wave front in the medium with variant velocity v_2. The corresponding field strengths are related by $I + R \cdot I = T \cdot I$. The individual field strength of the transverse electric (TE) and transverse magnetic (TM) fields is determined by the impedance contrast between the layers and the angle of incidence θ via:

$$R_{TE} = \frac{Y_1 \cos\theta_1 - Y_2 \cos\theta_2}{Y_1 \cos\theta_1 + Y_2 \cos\theta_2} \tag{3.2}$$

$$R_{TM} = \frac{Z_1 \cos\theta_1 - Z_2 \cos\theta_2}{Z_1 \cos\theta_1 + Z_2 \cos\theta_2}, \tag{3.3}$$

where Z_i and Y_i correspond to the impedance and admittance ($Y_i = 1/Z_i$) of the two layers (Annan, 2009).
The pulse width W of a GPR signal is directly related to the bandwidth B, which depending on the definition, can be related to the center frequency f_c of the signal. In chapter 6 f_c is defined according to Wang (2015) as the center-point of the half-band width. If the following relation is used (Annan, 2009):

$$W = \frac{1}{B} = \frac{1}{f_c}, \qquad \text{with} \qquad f_c = \lambda_c \cdot v, \tag{3.4}$$

with λ_c being the wavelength at center frequency and v the velocity, the lateral resolution length Δl and range resolution length Δr can than be calculated as:

$$\Delta l \approx \sqrt{\frac{d\lambda_c}{2}} \qquad \text{and} \qquad \Delta r \geq \frac{Wv}{4}. \tag{3.5}$$

Here, the lateral resolution length determines how well adjacent points at a certain distance d from the antenna can be distinguished from each other, whereas range or radial resolution length refers to the distance of successive objects in the same beam path.

3.1.2. Factors influencing the GPR performance

One fundamental factor leading to penalties in the GPR performance are the losses due to absorption of the EM energy, i.e. the intrinsic losses due to dispersive electrical properties of soils (as described in section 2.3). However, these losses causing attenuation and dispersion of the waves generally add up to other influencing factors. Here, other factors affecting the GPR apart from the absorption of the EM energy are very briefly described (see Fig.3.3).
On the one hand, there are characteristics of the GPR system, as for instance the dynamic range, which refers to the ratio between maximum and minimum signal power a receiver can give a distinguishable output signal (modern GPR has a total system dynamic range >130 dB; Grimm et al., 2017). Amongst other, the dynamic range controls the maximum depth range a potential survey target can be detected. Furthermore, there can be transmission and ground coupling losses between the antenna and the ground, for example due to topography, which can cause tilting of the antenna. In case of rain events, puddles can cause transmission losses due to the high reflectivity of water. Additionally, there are energy losses due to the geometrical spreading of the propagating EM wave in the ground. However, there are also further geological characteristics, which cause attenuation. Scattering of the EM energy is due to heterogeneities like stones, debris and roots, but also local density and moisture variations in the soil. Here, frequency or wavelength plays a significant role, since at microwave frequencies (very high GPR frequencies) the size of the heterogeneities can become in

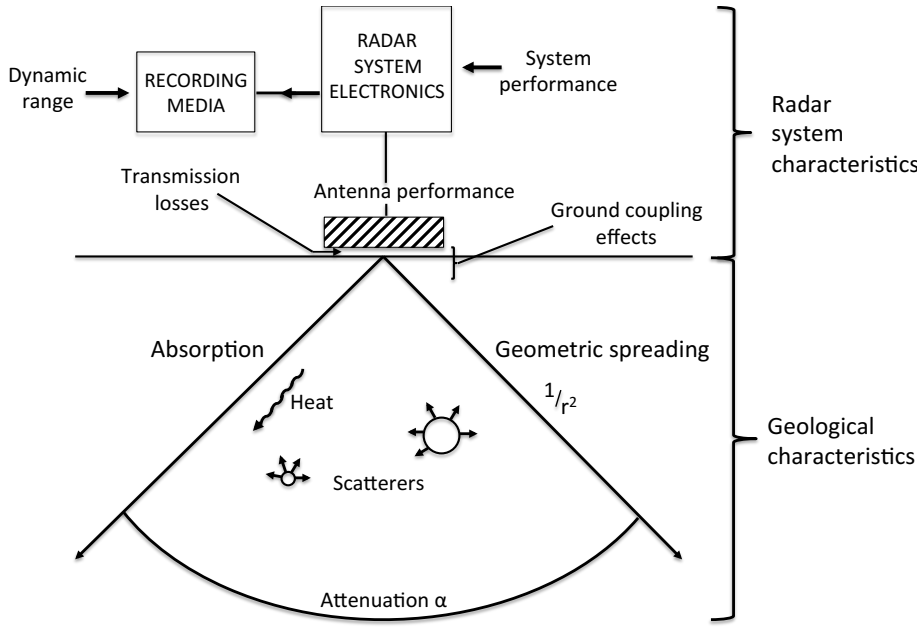

Fig. 3.3.: Overview of factors influencing GPR performance. The radar system characteristics are treated as a black box. Attenuation in the ground is due to scattering and absorption. EM Waves decay in the far field with respect to the distance r from the antenna (geometrical spreading; modified from Reynolds, 1997).

the order of the wavelength, which causes Mie-scattering (Takahashi et al., 2011), i.e. resonance or anti-resonance of the signal with the scattering object can either lead to strong amplification or attenuation of the reflected signal.
For the low-to intermediate GPR frequency range, i.e. in the case the heterogeneities are small in comparison to the wave length, Rayleigh scattering becomes more important. Here, the strength of the scattered signal and thus, the cross section area of the scatterer increases with the 4^{th} power of frequency (and also with the 6^{th} power of the object radius). The scattering occurs omni-directional, which causes attenuation of the EM energy. Thus, the total attenuation α_t in a soil can be calculated by:

$$\alpha_t = \alpha_i + \alpha_s, \tag{3.6}$$

where α_i corresponds to the intrinsic attenuation and α_s refers to the scattering attenuation. For the purpose of the thesis, attenuation α solely refers to the intrinsic attenuation and we assume homogeneous soils.

3.2. Dielectric spectroscopy

For the experimental characterization of the relaxation behavior of different soils, dielectric spectroscopy by means of the coaxial transmission line (CTL) technique was carried out. The laboratory intensive method is frequently used for the dielectric material characterization at MHz to GHz frequencies in various fields of applications, like

material sciences (Misra et al., 1990), biology (Athey et al., 1982) but also geological or soil physical research (Wagner et al., 2011; Lauer et al., 2012).

3.2.1. Principle and setup

The method consists of a vector network analyzer (VNA) generating EM waves in the frequency-domain and a coaxial cell in which the soil sample is placed (Fig.3.4). I used a Rhode & Schwarz ZVL 13 portable network analyzer and two different cells and cell holders for the soil samples. The first cell is a standard 7/16 airline conductor (7-16m-f; Rosenberger GmbH, Friedolfing, Germany) with a volume of 8.33 cm^3 and the cell holders consist of two RPC-N 50 Ω adapters (RPC-Nm-7-16m and RPC-Nf-7-16f). The second, bigger cell and setup was developed by Lauer et al. (2012) especially for measuring undisturbed soil samples. As described in Fig. 3.4 the bigger

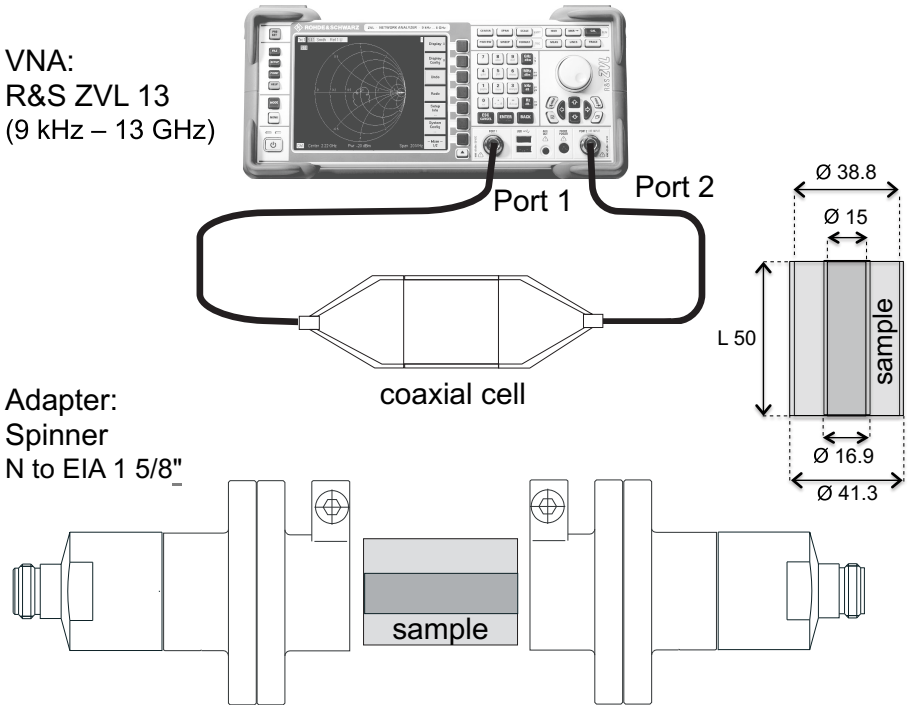

Fig. 3.4.: Overview of dielectric spectroscopy components with a vector network analyzer (VNA) in a 2-port CTL and description of the 'big' coaxial cell dimensions with adapter components (modified from Lauer et al., 2012; Wagner et al., 2013).

sample cell consists of a cylindrical inner and outer conductor made from copper with an effective volume of 42.29 cm^3. The open ends of the sample cell had been sealed using thin Teflon disks (2 mm thickness), in order to avoid leakage of the moist soil samples. The cell holders consists of two commercial coaxial N to 1.625-inch adapters (Spinner GmbH, Munich, Germany) as used in RF-applications (Lauer et al., 2012).

The CTL technique assumes propagation in the transverse EM (TEM) mode (Gorriti and Slob, 2005c), which means that the magnetic and electric field components are normal (transverse) to the propagation direction. For different frequencies the scattering parameters (S-parameters) are measured, i.e. for each frequency step, amplitude and phase components (vectors) of the transmission and reflection parameters are stored in a matrix with complex numbers. The two-port system, as depicted in Fig. 3.5 measures in both directions and is related by the complex S-parameter matrix and the reflected and incident power waves via:

$$\begin{pmatrix} b_1 \\ b_2 \end{pmatrix} = \begin{pmatrix} S_{11} & S_{12} \\ S_{21} & S_{22} \end{pmatrix} \cdot \begin{pmatrix} a_1 \\ a_2 \end{pmatrix}, \tag{3.7}$$

where a_N refers to the incident waves at port N and b_N to the reflected waves (with $N = \{1,2\}$). S_{11} and S_{22} correspond to the ratio of the reflected wave from port 1 (b_1) to the incident wave at port 1 (a_1), whereas S_{12} and S_{21} correspond to the transmitted wave coming out from port 1 (b_1) to the incident wave at port 2 (a_2) and vice versa (b_2/a_1). Each S-parameter is determined by measuring both magnitude and phase of the incident, reflected or transmitted signals when the output is terminated in a perfect Z0 load (i.e. for $S_{11} \rightarrow a_2 = 0$; Sischka, 2010).

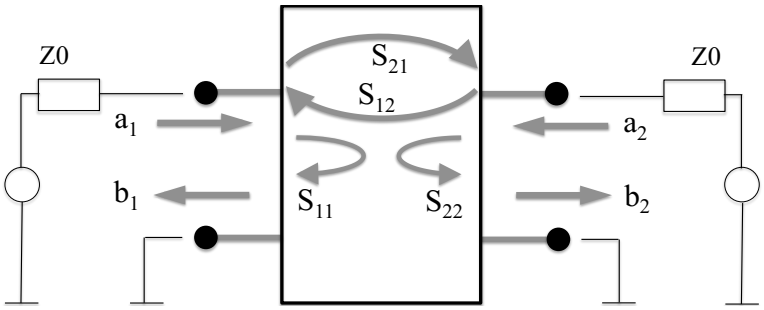

Fig. 3.5.: Schematic overview of S-parameter calculation in a two-port system using a combination of incident (a) and reflected or transmitted (b) voltage amplitude ratios measured in both directions (see Eq.3.7; modified from Sischka, 2010).

For automatic permittivity calculation from S-parameters the Agilent 85071 Materials Measurement Software was used. Three different standard algorithms provided by the software showed most reasonable and comparable results in a certain frequency range:

- The 'Reflection/Transmission μ and ε' (Refl/Tran u&e) algorithm, which was developed by Nicolson and Ross (1970) and Weir (1974) to calculate both permittivity and permeability from the S-parameters (S_{11}/S_{11} or S_{22}/S_{12}), but which can have discontinuities for low loss samples with a sample length of $>1/2$ wavelength (Keysight-Technologies, 2017).

- The 'Reflection/Transmission ε Precision' (Refl/Tran e Prec'n) algorithm developed at the National Institute of Standards and Technology (NIST; Baker-Jarvis

et al., 1990), which calculates permittivity from the transmission and reflection coefficients (S_{ij}, no calculation of μ; Keysight-Technologies, 2017). The algorithm is best for long, low-loss samples (Hewlett-Packard, 1993).

- The 'Transmission ε Fast' (Tran e Fast) algorithm (unpublished), which is an iterative method that estimates permittivity, calculates the transmission parameters therefrom and minimizes the difference between the transmission parameters and the measured values (S_{12}/S_{21}, no calculation of μ; Keysight-Technologies, 2017). The algorithm is also best for long, low-loss samples (Hewlett-Packard, 1993).

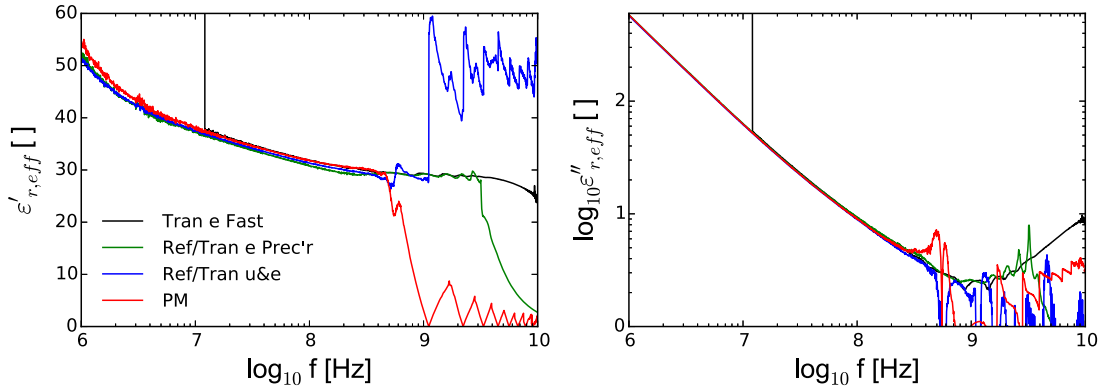

Fig. 3.6.: Comparison of complex permittivity calculation from S-parameters of a lossy soil using different algorithms provided in the Agilent software and the implemented Propagation Matrix (PM) method.

These standard algorithms provided by the software were complemented by another algorithm, in order to increase the flexibility with respect to variations of certain cell components (e.g. thickness and number of sealing teflon disks, samples holder length, layered samples). Therefore, the Propagation Matrices (PM) method was implemented, which enables to translate the multisectional transmission line model into matrix notation. The analytical reconstruction technique relates the S-parameters to the total reflection and transmission of the line seen as a two-port network (Gorriti and Slob, 2005c,b,a). It is especially useful for high-loss frequency-dependent media, but becomes unstable for very high-frequencies.
Fig. 3.6 shows the result of complex effective dielectric permittivity calculation from S-parameters using the different algorithms for a moist fine-grained soil. The 'Tran e fast' algorithm is the only algorithm, which enables to calculate permittivity above 3 GHz frequencies. However, it fails to calculate permittivity at frequencies below 10 MHz. In contrast, the two other standard algorithms provided by the Agilent software ('Prec' and 'u & e') and the implemented PM method show reasonable results predominantly below the GHz frequency range, but cannot resolve the very-high frequencies. Furthermore, depending on the water content (and thus also conductivity), the frequency limit for the 'Tran e fast' algorithm to resolve permittivity at low-frequencies

varied (see 3.7). So, with increasing soil conductivity, the more the minimum resolvable frequency shifted to higher frequencies. Therefore, in cases the 'Tran e fast' algorithm could not resolve the low- frequency part, we combined it with the spectrum calculated by the PM method (at 200 MHz cutoff frequency). Even so the other algorithms showed very similar results at low-frequency in most cases, the results of the PM methods were slightly more congruent with the Fast-method providing a continuous permittivty spectrum between 1 MHz and 10 GHz.

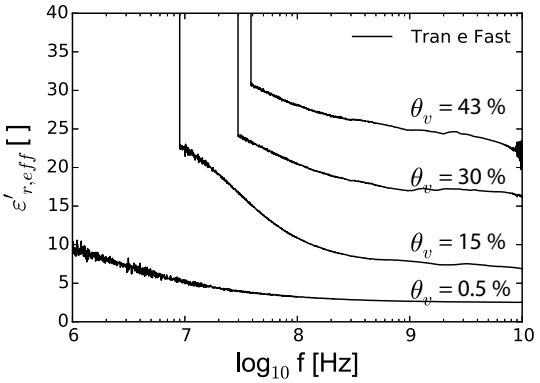

Fig. 3.7.: Real permittivty calculated using the 'Tran e Fast' algorithm for a lossy soil at different volumetric water content θ_v.

For both cells we used a full two-port TOSM (Through, Open, Short and 50 Ω-Match) calibration with the calibration plane either at the adapter ends (including the adapters; small cell) or excluding the adapters (big cell). For the cell holders of the big cell, no 50 Ω-Match adapter was available, which hindered their consideration into the standard electrical calibration. So we used a Short adapter to calculate the electric length of the cell holders and different calibration standards like alcohols, air and teflon with known electrical parameters in order to determine the best calibration parameters. The result of a calibration using different alcohols is exemplary shown in Fig. 3.8. All alcohols (methanol, ethanol and isopropyl) have typical relaxation times and strength and precise temperature-dependent relaxation models can be found in the literature Kaatze (e.g. 2007); Gregory and Clarke (e.g. 2012).

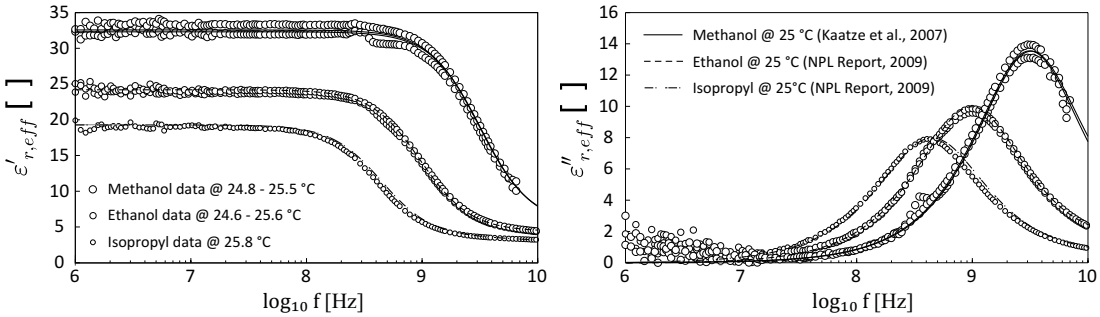

Fig. 3.8.: Complex effective dielectric permittivity of different alcohols measured with the CTL technique and the 'small' cell (circles). Reference data (dashed and continuous lines) from dielectric relaxation models as provided in Kaatze (2007); Gregory and Clarke (2012).

3.2.2. Sample preparation and installation

All soil samples, which are investigated in this thesis were collected in-situ in the field and transported in airtight packaging. In the laboratory, the small cell was filled in sophisticated steps and under constant compaction with the soil. A fixture was build, which allowed to use one cell holder together with the empty cell as a bin, in which the sample could be filled. The fixed vertical setup was especially useful when measuring liquids for reference, since it avoided leakage (see Fig. 3.9d). In case of dielectric spectroscopy of soils with the big cell, a practical, since time-saving infilling facility was available (Fig. 3.9c), which enables to prepare the sample separately before connecting it to the cell holders in the coaxial transmission line (Fig. 3.9a). Thus, the sample was sealed with two teflon disks at the outer ends, which made it portable. This property helped to accurately determine the sample weight using a sensitive scale (Fig. 3.9b) before and after oven drying, since it avoided greater material loss after disassembling the sample from the transmission line.

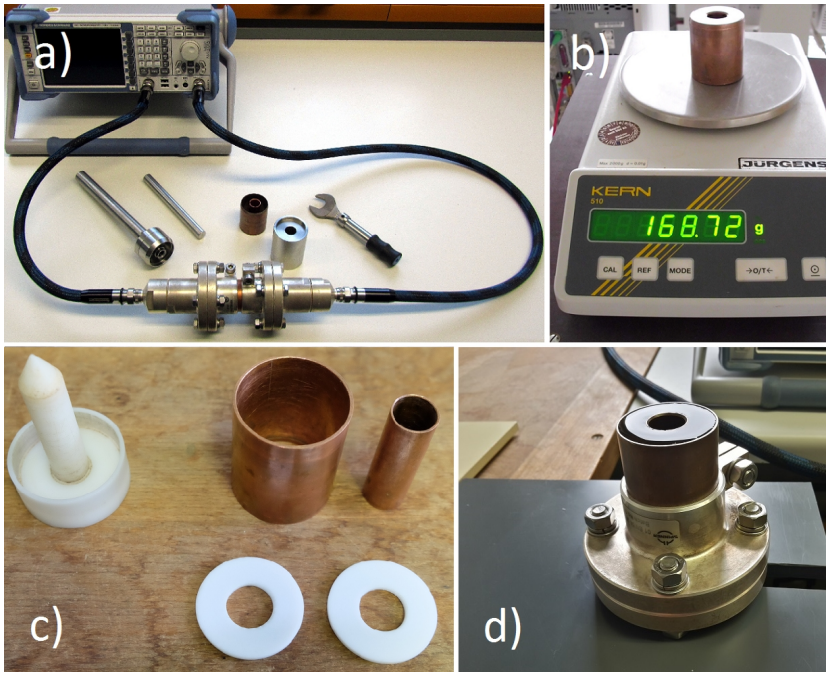

Fig. 3.9.: Overview of installation and preparation tools for dielectric spectroscopy using the 'big' cell: a) coaxial tranmission line together with tools for undisturbed soil sampling; b) scale for weighing the sample; c) soil-infilling facility, inner and outer conductor of the cell and sealing teflon disks; d) vertical fixture for the cell holder for measurements of liquids (illustrated example) and saturated samples.

3.3. Time-domain reflectometry

The Time-domain reflectometry (TDR) is generally rooted in electrical engineering of the 1930s with the focus on the detection of cable faults in wide-band transmission systems (Hewlett-Packard, 1964; Rako, 2007). The TDR system works similarly to the radar technique. It generates a fast rise-time pulse, which travels in form of EM waves through the cable until it gets reflected back from a potential cable fault causing an impedance contrast or mismatch in the cable. The pulse amplitude over time can be recorded using an oscilloscope. Thus, for a calibrated system, the 2-way travel-time of the reflected signal can directly be assigned to the distance of the defect in the cable. In the 1960s, first high-performance systems with integrated very-fast pulse generators (in the nano-second range) and sampling head were introduced for pulse-echo reflectometry (Rako, 2007), which enabled to detect impedance contrasts at a very small scale (Hewlett-Packard, 1964). The connection between moisture content, dielectric permittivity and the velocity of EM waves in different media, such as soils was already described earlier (e.g. von Hippel, 1954). From the 1970s, TDR became a frequently used method for measuring the dielectric permittivity of materials (Fellner-Feldegg, 1969; Cole, 1977), and also for accessing the moisture content of soils (Hoekstra and Delaney, 1974; Topp et al., 1980). A compact review of advances in TDR for soil moisture measurements can be found in Robinson et al. (2003).
In contrast to cable fault testing, soil moisture measurements by TDR require a probing head, which serves as the moisture sensor and which gets immersed into the soil. In many cases, the sensor consists of a two-rod or three-rod probe with length between 7.5 to 30 cm (Campbell, 2013), which is connected via coaxial cable to the pulse generator, sampling and digitizing unit. For soil moisture measurements the rods have to be fully immersed into the the soil. A generated step voltage pulse travels along the rods and gets reflected back from the ends of the rods. The travel-time of the reflected pulse directly depends on the soil moisture content. As shown in section 2.3, water has strong polarizability and therefore, a medium exhibits an increased dielectric permittivity when saturated with water. Fig. 2.6 showed that the measured dielectric permittivity of soils increase with the volumetric water content and that a regression curve can be formulated (Topp et al.,

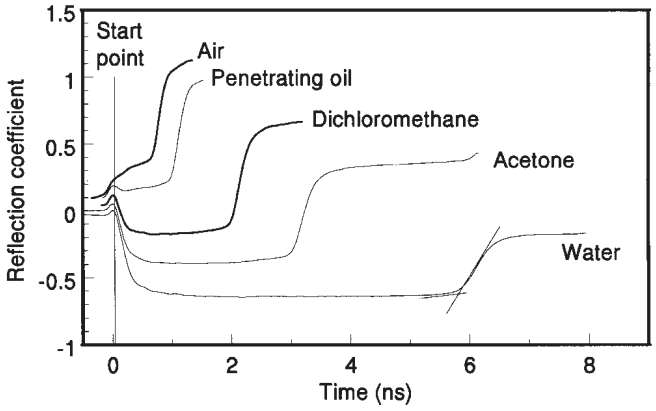

Fig. 3.10.: TDR waveforms demonstrating the travel time increase with increasing permittivity for different materials (from Robinson et al., 2003).

1980). Furthermore, velocity v decreases with increasing permittivity (Eq. 2.20 together with Eqs. 2.37, 2.36). In terms of the reflected TDR pulse, which travels in the round trip propagation time t [s] along the rods of the transmission line with the length l [m], velocity can be expressed as (Robinson et al., 2003):

$$v = \frac{2l}{t}. \tag{3.8}$$

After rearranging, the round trip time gives:

$$t = \frac{2l\sqrt{\frac{\varepsilon'_{r,eff}}{2}\left(\sqrt{1+\tan^2\delta}+1\right)}}{c_0}. \tag{3.9}$$

Using this formula together with a regression curve, as for instance defined by Topp et al. (1980), enables to assess the volumetric moisture content θ_v of soils by TDR. Fig. 3.10 shows TDR waveforms for different materials. The time at which the reflection from the rod ends occur can be picked at the intersect of the tangent on the ascending part of the curve with the horizontal extension of the lower plateau. The round trip travel time is the difference between that intersection point and the start point at the beginning of the rod.

Apart from permittivity measurements of soils using TDR it is also possible to ac-

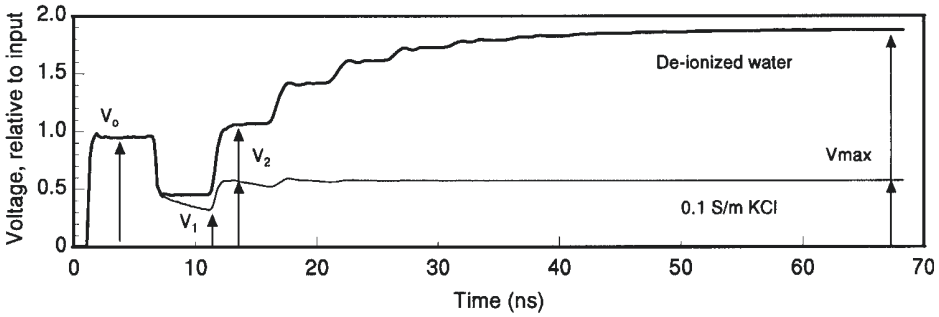

Fig. 3.11.: TDR signal (as normalized voltage amplitude) for very long travel-times for water with varying electrical conductivity (de-ionized and with 0.1 S/m; from Robinson et al., 2003).

cess the electrical conductivity. Here, different concepts exist. One frequently used approach to derive conductivity from the measured TDR waveform in the laboratory uses the maximum voltage plateau (V_{max}), which can only be calculated at very long travel-times after all multiple reflections faded away (see Fig. 3.11; Giese K, 1975; Heimovaara, 1994). Another concept was proposed by Topp et al. (1988), who introduced an approach, which was described as 'broadband' conductivity in Robinson et al. (2003), since it also accounts for losses due to dielectric relaxations (see Eq. 2.26). Since very short travel-times are used in order to calculate the conductivity

term, we refer to it as the high-frequency electrical conductivity σ_{HF} instead. Here, σ_{HF} can be expressed in terms of the ratio of the initial voltage V_0 to the voltage magnitude when entering the medium V_1 and the voltage magnitude of the reflected wave V_2, via (see Fig. 3.11):

$$\sigma_{HF} = \frac{\varepsilon'_{r,eff}}{120\pi l} \ln\left[\frac{V_1(2V_0 - V_1)}{V_0(V_2 - V_1)}\right]. \tag{3.10}$$

Another, but very similar approach to measure high-frequency conductivity was introduced by Dalton et al. (1984); Dasberg and Dalton (1985), who only compared V_1 and V_2 to each other, as:

$$V_2 = V_1 \exp -2\alpha l, \tag{3.11}$$

where α corresponds to the attenuation coefficient. Thus, electrical conductivity can be calculated using:

$$\sigma_{HF} = \frac{\varepsilon'_{r,eff}}{120\pi l} \ln\left[\frac{V_1}{V_2}\right]. \tag{3.12}$$

One commercial provider for field moisture sensors uses an empirical concept in order to derive the electrical conductivity of the soil, which is physically lean on the former approach by Dasberg and Dalton (1985). IMKO (2017) for instance uses rods that are coated by PVC, which enables to measure also in highly conductive soils. It uses a very fast step-pulse and measures the reflected voltage in terms of a dimensionless TDR-amplitude in distinct small time intervals (see Fig.3.12). An internal algorithm picks a

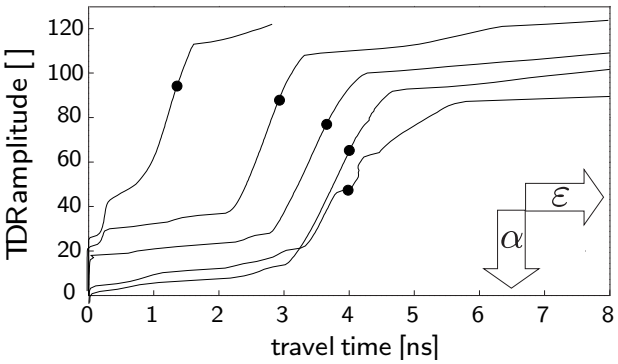

Fig. 3.12.: TDR signal measured for different materials with varying moisture content using a TRIME-PICO 64 field moisture sensor. The Dots refer to the data, which are internally processed in order to derive electrical conductivity and moisture content of a soil (IMKO, 2017) or attenuation α and permittivity ε, respectively (Loewer and Igel, 2016).

point near the inflection point of the ascending curve. Using elaborate volumetric water content and conductivity measurements of different media, an empirical relationship between TDR-travel time and soil water content as well as electrical conductivity and the TDR-amplitude is established (IMKO, 2017). However, it should be emphasized that the measured conductivity value rather refers to a high-frequency conductivity, which also contains losses due to dielectric relaxations effects. In the course of the

thesis it is shown that the TDR-amplitude near the inflection point can be calibrated for attenuation measurements with an effective measurement frequency of ≈ 1 GHz.

4. Dielectric spectroscopy of soils and prediction of GPR performance

This chapter is a post-print version and was published on May 14, 2015 by IEEE under the following title:
Loewer, M., Igel, J. & Wagner, N. (2016): Spectral Decomposition of Soil Electrical and Dielectric Losses and Prediction of *In Situ* GPR Performance. IEEE Journal of Selected Topics in Earth Observations and Remote Sensing, 9(1), pp. 212-220, doi: https://doi.org/10.1109/JSTARS.2015.2424152.

Abstract

The performance of high-frequency ground-penetrating radar (GPR) for high-resolution imaging of the near surface can essentially be controlled by the soil electromagnetic (EM) properties. One of these properties influencing sensing depth and image resolution of GPR is the intrinsic attenuation. We investigated the frequency-dependent electrical and dielectric properties of a broad range of soil samples. In order to derive the effective complex dielectric permittivity between 1 MHz and 10 GHz, we applied the coaxial transmission line (CTL) technique. A generalized dielectric response model, consisting of one Debye and one Cole-Cole type relaxation and a constant low-frequency conductivity term was used to analyse the dielectric relaxation behaviour. Splitting the spectra into individual loss processes shows that dielectric relaxation mechanisms play a crucial role in most natural soils. Especially for high-frequency applications, attenuation cannot be described by a dielectric constant and dc-conductivity alone. Therefore, a simple conductivity-attenuation relation without dielectric losses can highly overestimate the GPR performance. As an alternative to the CTL technique in the lab, we suggest to use time-domain reflectometry (TDR) for the in-situ assessment of high-frequency electrical properties and deduced prediction of GPR performance.

4.1. Introduction

GPR utilizes radar-wave reflections from impedance contrasts, which are caused by natural or artificial disturbances in the subsurface. This technique operates in a frequency band in which electrical losses due to the mobility of charges are not the dominant mechanism and in which the dielectric relaxation of the pore water does not prevail. For soils, this GPR band is generally located between the lower MHz and the lower GHz frequency range, in which the upper frequency boundary strongly depends on the soil moisture. For applications that require high resolution images from depths less than 1 m, GPR antennas with GHz center frequencies are used.
One application area of these high-frequency sensors comprises military and postwar issues, as the detection of landmines, unexploded ordnances (UXOs) and improvised explosive devices (IEDs) (Miller et al., 2004; Van der Bosch et al., 2006; Takahashi and Sato, 2008). For these applications a reliable prediction of GPR performance is essential in order to know, e.g., the maximal depth of investigation or other limitations and to identify cites at which GPR is not a suitable technique. As landmines are buried very shallow within the upper 10 cm of the soil, attenuation has rather minor influence on the GPR performance. For shallow investigation depths, the limiting factors are generally restricted to soil heterogeneity and micro-topography, which can mask the landmine signal (Igel, 2008), Takahashi et al. (2012), (Takahashi et al., 2011). In contrast, apart from scattering effects, radar images of deeper buried targets like IEDs, which are an increasing threat during the last years, can be essentially influenced by the intrinsic attenuation. Provided a dielectric contrast between target and soil exists, the soil dependent absorption of electromagnetic (EM) energy can control the ability to distinguish a buried explosive device from its surrounding medium.
Intrinsic attenuation is entirely controlled by the frequency-dependent complex effective dielectric permittivity, or equivalently the complex effective electrical conductivity (Knight and Endres, 2005). Much work has been done in the past decades in order to understand the physical causes for the absorption of the EM waves in soils and in order to predict the soil dielectric properties in the radar frequency range (Shen et al., 1985; Hallikainen et al., 1985; Dobson et al., 1985; Taherian et al., 1990; Olhoeft and Capron, 1994; Arcone et al., 2008; Stillman and Olhoeft, 2008; Arcone and Boinett, 2012)). Moreover, there have been efforts to gain further subsurface information from analysing the frequency-dependent attenuation in GPR data (Irving and Knight, 2003; Bradford, 2007; Cassidy, 2008).
In contrast, our investigation is focused on a qualitative and quantitative description of the individual loss processes that occur in a broad spectrum of soils. In the majority of natural soils, dielectric relaxation effects at soil- water interfaces will crucially contribute to the electromagnetic losses. It is a fact that with increasing clay and silt content the GPR performance of a moist soil will decrease due to the relaxation effects. However, these effects are hard to measure in the field, since they occur in the high-

frequency range. On the basis of our laboratory measurements, we are able to show the contribution of each loss mechanism to the intrinsic attenuation. Furthermore, our approach enables to chose and calibrate proper tools that can predict the soil-dependent performance of a certain GPR system in the field.

4.2. Wave propagation in soils

4.2.1. Soil properties and intrinsic attenuation

Soil can be considered as a complex and heterogeneous mixture of different phases in varying fractions. Dependent on the soil texture, structure and mineralogy, water will undergo attraction forces of varying origin and strength. In contrast to well graded clay free sand for instance, clayey soils attract water in a much higher extent. The huge specific surface areas of clay minerals and their high cation exchange capacity results in strong molecular forces at the solid-liquid interface (see Wagner and Scheuermann, 2009; Wagner et al., 2011). Due to the complex nature of the soil systems, the interaction of electromagnetic waves with the individual soil components strongly depends on the frequency of the applied EM field. Therefore, the constitutive electromagnetic parameters electrical conductivity σ, dielectric permittivity ε and magnetic permeability μ become frequency-dependent and complex. Fig. 4.1 schematically illustrates a variety of different loss mechanisms that contribute to the complex effective dielectric permittivity from the very low up to the microwave frequency band of the EM spectrum for a moist porous medium. In the GPR frequency range only a few of these mechanisms are active: the bound water relaxation (B), the free water relaxation (M1), the Maxwell-Wagner effect (MW) and the counter-ion or surface relaxation (S) in some cases. For the parameters electrical conductivity and magnetic permeability simplifying assumptions are often made. Low-frequency processes of electrical conductivity such as induced polarization in the electrical double layer (DL) or polarization caused by constrictivity of pores are negligible at radar frequencies. Thus, the losses due to electrical conduction are assumed to be described by the direct current electrical conductivity σ_{dc} (C). Furthermore, for most soils magnetic losses can be neglected and magnetic permeability is set equal to its free space value μ_0 (Topp et al., 1980).
In order to split the experimental results into different polarization mechanisms or energy storage and energy loss parts, we express the constitutive electromagnetic material properties in terms of a complex relative effective permittivity:

$$\varepsilon^*_{r,eff}(\omega) = \varepsilon'_{r,eff}(\omega) - i\varepsilon''_{r,eff}(\omega) \tag{4.1}$$

with

$$\varepsilon'_{r,eff}(\omega) = \varepsilon'_r(\omega) + \frac{\sigma''(\omega)}{\varepsilon_0 \omega} \tag{4.2}$$

and

$$\varepsilon''_{r,eff}(\omega) = \varepsilon''_r(\omega) + \frac{\sigma'(\omega)}{\varepsilon_0\omega} = \varepsilon''_r(\omega) + \frac{\sigma_{dc}}{\varepsilon_0\omega} \tag{4.3}$$

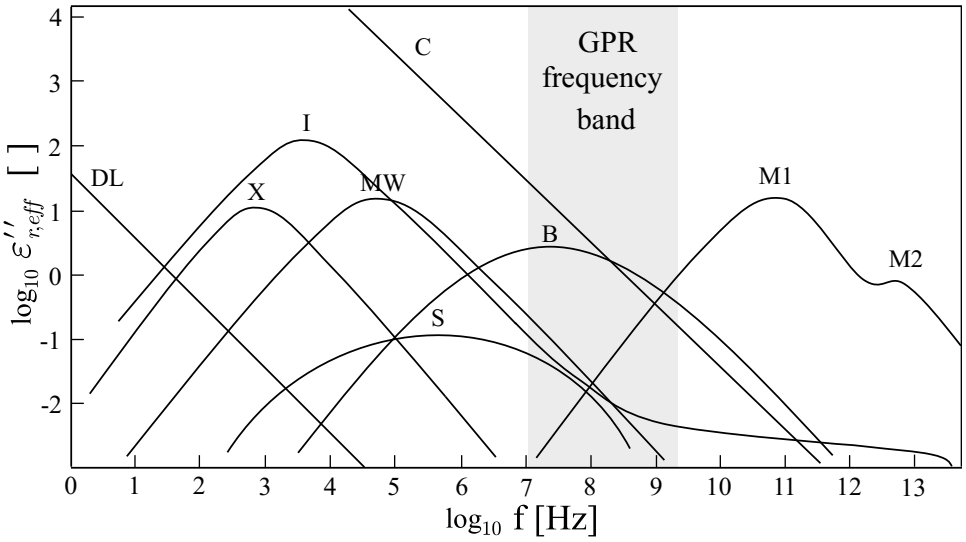

Fig. 4.1.: Overview of dielectric relaxations and electrical conduction taking place in moist porous media from the very low up to the microwave frequency range. Mechanisms include C: dc-electrical conductivity, DL: charged double layer, X: crystal water, I: ice relaxation, MW: Maxwell-Wagner relaxation, S: surface conductivity, B: bound water relaxation, M1: principle free water relaxation, M2: second free water relaxation (modified from (Hasted, 1973)).

or equivalently in terms of a complex effective electrical conductivity:

$$\sigma^*_{eff}(\omega) = \sigma'_{eff}(\omega) + i\sigma''_{eff}(\omega) \tag{4.4}$$

with

$$\sigma'_{eff}(\omega) = \sigma'(\omega) + \omega\varepsilon_0\varepsilon''_r(\omega) = \sigma_{dc} + \omega\varepsilon_0\varepsilon''_r(\omega) \tag{4.5}$$

and

$$\sigma''_{eff}(\omega) = \sigma''(\omega) + \omega\varepsilon_0\varepsilon'_r(\omega) \tag{4.6}$$

where ε_0 is the free space permittivity. Aside from the direct current conductivity σ_{dc} all parameters depend on the angular frequency $\omega = 2\pi f$, where f is the frequency. In order to predict the soil-dependent performance limits of GPR, it is necessary to determine the intrinsic attenuation. The intrinsic attenuation α can either be calculated by the effective complex dielectric permittivity, the effective complex conductivity or by taking the real parts of both effective parameters using the expression

$$\alpha(\omega) = \frac{\omega}{c_0}\sqrt{\frac{\varepsilon'_{r,eff}(\omega)}{2}\left(\sqrt{1+\left(\frac{\sigma'_{eff}(\omega)}{\omega\varepsilon_0\varepsilon'_{r,eff}(\omega)}\right)^2}-1\right)}. \tag{4.7}$$

In order to express the attenuation in its typical units (dB/m), we multiplied $\alpha(\omega)$ by the factor 8.686.
In low-loss media, intrinsic attenuation can be considered as frequency-independent over a certain frequency range, the "GPR plateau" (Annan, 2005). A typical example for a low-loss soil is well graded clay free sand, which is depicted in Fig. 4.2. At 0 % volumetric water content, intrinsic attenuation is very low and almost entirely frequency-independent. However, this clearly changes when small amounts of water are present in the soil. The intrinsic attenuation strongly rises with increasing water content from frequencies above approximately 1 GHz. Loamy and clayey soils, in contrast, are rather high-loss media and show considerably stronger intrinsic attenuation as well as frequency-dependence across the whole frequency range (Fig. 4.2). Most of the soils in nature have attenuation spectra, that are somewhere between these depicted examples.

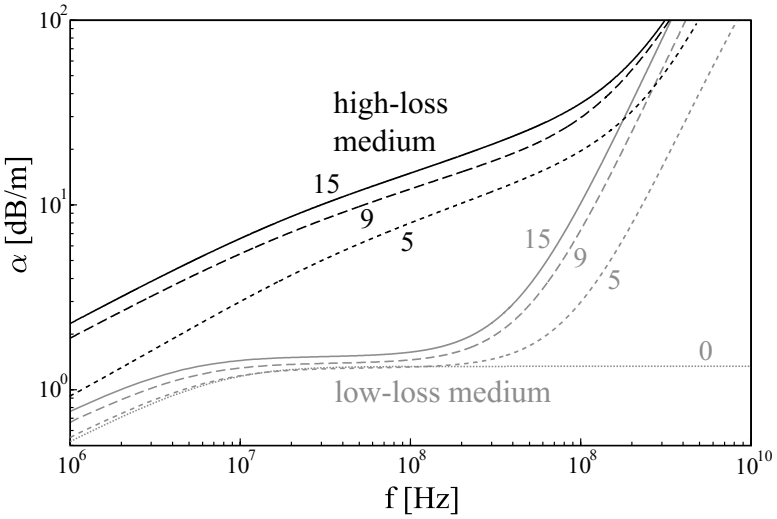

Fig. 4.2.: Intrinsic attenuation of two different soils for varying volumetric water contents between 0 to 15% .

4.2.2. Influence on GPR performance

In our proposed approach, the GPR system itself is regarded as a black box and factors like antenna gain and coupling effects are disregarded. Thus, considering a nearly homogeneous soil with a flat surface, the limiting factor for the performance of a certain radar system is basically reduced to the intrinsic attenuation. Fig. 4.3 shows radar profiles from two different soils were an air filled plastic canister has been buried in 30 cm depths. The target has the typical dimension of an IED, which is commonly buried in depths up to 1 m. The measurements have been carried out using a GSSI GPR antenna with a center frequency of 900 MHz. The processing steps comprised header gain and static correction, dewowing and divergence compensation, as well as a bandpass filter.

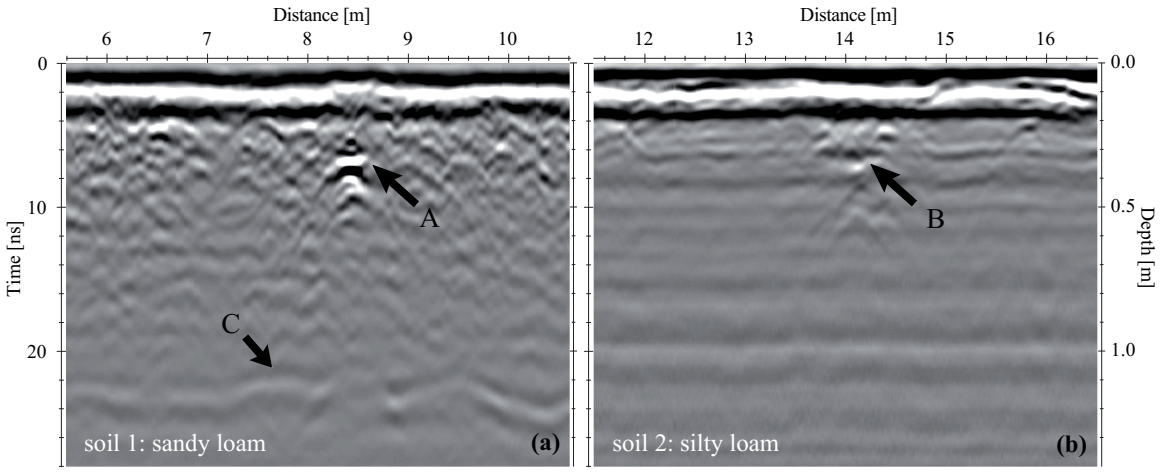

Fig. 4.3.: 900 MHz radar profiles of a sandy loam (a) and silty loam (b) where plastic targets have been buried (A & B). A material interface between the top soil and a gravel layer (C) is visible in soils 1, but is missing in soil 2. Each section was processed using header gain and static correction, divergence compensation, dewowing and a bandpass filter.

In soil 1 (Fig. 4.3a), we can observe that the reflection hyperbolas of the plastic canister are clearly visible (A). In contrast, in soil 2 (Fig. 4.3b) they are much weaker (B). Furthermore, reflections from the interface between soil material and a gravel layer at a depth of approximately 1 m can clearly be noticed in soil 1 (C). However, no energy from depth larger than 60 cm can be observed in soil 2, even though the gravel layer does exist in the same depth. Instead, ringing effects are prominent in soil 2 that are most probably caused by the antenna mismatch.

4.3. Methodology

In order to investigate the quality and quantity of the individual loss mechanisms in the depicted soils (Fig. 4.3), several samples had been extracted from the test lanes. Furthermore, geoelectric measurements had been carried out in order to map the heterogeneity and dc-conductivity distribution. Both soils were quite homogeneous and the mean dc-conductivity was 10 and 40 mS/m for soil 1 and 2, respectively. However, the results show that in order to predict the attenuation in a certain soil, measuring the dc-conductivity and adding the information of the water content will not suffice.

4.3.1. Laboratory measurements

In experimental laboratory investigations, we measured the effective complex dielectric permittivity of the soil samples using the coaxial transmission line (CTL) technique with a R&S ZVL network analyzer (see Wagner et al., 2010; Lauer et al., 2012, for details) for details between 1 MHz and 10 GHz. The complex dielectric permittivity was calculated from the measured scattering parameters (S-parameters). We used

a combination of the quasi-analytical propagation matrix method (PM, (Gorriti and Slob, 2005c)) for the frequency range from 1 MHz to 200 MHz and the iterative fast transmission method (FAST, Agilent (2014)) for frequencies above 200 MHz. Calibration measurements with the reference standards methanol, ethanol and isopropyl showed good agreement with literature values. After the EM measurement the filled CTL-cell with known volume was weighted. Subsequently, each of the soil samples was oven-dried (at 105 °C for 24 hours) and weighted in order to determine its volumetric water content and dry density in the cell. The volumetric water content of the soil samples from the GPR test lanes (Fig. 4.3) was similar with 15 % in soil 1 and 18 % in soil 2, respectively. The bulk density also just slightly varied. An overview of the measured soil parameters is given in Tab. 4.1. Here, soil 1 corresponds to the sandy loam and soil 2 is the silty loam. Both soils have the same amount of clay (19 %), whereas soil 2 has an increased amount of silt (73 %). In order to underline the results of our investigation, we complemented the depicted soil samples from the GPR test lanes with a clay loam that comprises an increased clay fraction (Tab. 4.1).

Tab. 4.1.: Properties of the investigated soils

	sandy loam	**silty loam**	**clay loam**
ω [g/g]	0.207	0.182	0.186
n	0.37	0.32	0.38
θ_v [cm^3/cm^3]	0.15	0.18	0.18
ρ [m/cm^3]	1.6	1.4	1.4
clay fraction [%]	19	19	36
silt fraction [%]	19	73	42
sand fraction [%]	62	8	22

Apart from the selected examples, which are treated in the paper in more detail, we investigated the electromagnetic soil properties of 27 soil samples. All soil samples varied in grain size distribution from pure sand to heterogeneous mixtures with varying silt and clay content and different mineralogy. In each measuring sequence, they were stepwise saturated using de-ionised water until full-saturation was reached.

4.3.2. Decomposition of polarization mechanisms

The measured permittivity spectra of the soils were parameterized by means of a two term dielectric response model consisting of one Debye- and one Cole-Cole relaxation and a dc-conductivity term:

$$\varepsilon^*_{r,eff}(\omega) = \varepsilon_\infty + \frac{\Delta\varepsilon_1}{1+i\omega\tau_1} + \frac{\Delta\varepsilon_2}{1+(i\omega\tau_2)^\beta} - i\frac{\sigma_{dc}}{\omega\varepsilon_0}, \tag{4.8}$$

with $0.5 \leq \beta \leq 1$. ε_∞ corresponds to the high-frequency limit of the permittivity, $\Delta\varepsilon_1$ and $\Delta\varepsilon_2$ are the relaxation strength of the Debye- and Cole-Cole relaxations, τ_1 and τ_2 are the relaxation times and β is the stretching exponent of the Cole-Cole type process (Wagner et al., 2010; Lauer et al., 2012; Schwing et al., 2013).
In order to invert for the best curve-fitting parameters, we used a Levenberg-Marquardt scheme provided by the Geophysical Inversion and Modelling Library (GIMLi) (Rücker et al., 2016). For all parameters, a logarithmic transformation was used in order to fix the parameters to a certain range. The starting guess, as well as lower and upper boundaries for each model parameter is given in Tab. 4.2.

Tab. 4.2.: Boundary conditions and inversion start values

parameter	start value	lower boundary	upper boundry
$\Delta\varepsilon_1$	10.0	0.0	100.0
$\Delta\varepsilon_2$	1000.0	0.0	10000.0
τ_1 [s]	1.0e-12	1.0e-13	1.0e-11
τ_2 [s]	1.0e-8	1.0e-11	1.0e-6
β	0.75	0.5	1.0
σ_{dc} [S/m]	1.0e-2	1.0e-9	1.0e1
ε_∞	2.95	1.0	10.0

In order to account for the different quantitative variation of the low- and high-frequency parameters, the data were weighted using an absolute and relative error. For the inversion, the absolute error for the real and imaginary part of dielectric permittivity was set to 0.05 and the relative error was set to 1 %. Furthermore, a regularization parameter of $\lambda = 100$ was used for all data sets.

4.4. Results

The frequency spectra of the measured effective complex relative dielectric permittivity $\varepsilon_{r,eff}$, the effective complex electrical conductivity σ_{eff} and the calculated intrinsic attenuation α for the three soils described in Tab. 4.1 are depicted in Fig. 4.4. The effective complex conductivity was calculated from the effective complex dielectric permittivity (Eq. 4.5, 4.6). This representation is helpful, since it allows to see at

which frequency the effective complex conductivity is constant and approaches dc-conductivity. Furthermore, one can observe at which frequency dielectric losses are setting in. The intrinsic attenuation was calculated by the real parts of the effective complex parameters using Eq. 4.7. In accordance to the GPR sections (Fig. 4.3), it can be observed that the intrinsic attenuation of both soil samples from the GPR test lanes strongly differ. At a measuring frequency of 900 MHz, which corresponds to the center frequency of our GPR antenna, the silty loam (soil 2) attenuates EM waves over two times stronger then the sandy loam (soil 1, compare Fig. 4.4e with Fig. 4.4j). In contrast, the clay loam with increased clay fraction has an attenuation rate (Fig. 4.4o), which lies in-between the attenuation rates of the GPR test lanes. However, the individual contribution of the loss mechanisms behind the overall attenuation differ from each other.
Apart from the measured data, Fig. 4.4 shows the fit of a curve (red line) that was inverted using the dielectric response model (Eq. 4.8). The contribution of each relaxation process to the total response is highlighted by two different colors and a dashed line, which refers to the contribution by the dc-conductivity. The exact values of these parameters, including the variance of each parameter, the RMS error and χ^2 are given in Tab. 4.3.

Tab. 4.3.: Results of the Inverse Modelling using Eq. 4.8

	sandy loam	**silty loam**	**clay loam**
ε_∞	3.32 ($\pm$ 3.5 %)	2.80 ($\pm$ 10.3 %)	2.60 ($\pm$ 9.6 %)
$\Delta\varepsilon_1$	4.35 ($\pm$ 2.6 %)	6.07 ($\pm$ 4.7 %)	4.30 ($\pm$ 5.7 %)
τ_1 [ps]	5.90 ($\pm$ 3.0 %)	6.31 ($\pm$ 4.8 %)	6.16 ($\pm$ 6.3 %)
$\Delta\varepsilon_2$	53.34 ($\pm$ 2.4 %)	57.46 ($\pm$ 0.1 %)	223.54 ($\pm$ 2.4 %)
τ_2 [μs]	428.7 ($\pm$ 5.3 %)	16.8 ($\pm$ 0.3 %)	718.0 ($\pm$ 4.8 %)
β	0.54 ($\pm$ 0.002)	0.78 ($\pm$ 0.001)	0.58 ($\pm$ 0.001)
σ_{dc} [S/m]	0.012 ($\pm$ 0.1 %)	0.044 ($\pm$ 0.1 %)	0.004 ($\pm$ 0.6 %)
abs. RMS	0.27	0.78	0.40
rel. RMS	6.59 [%]	3.00 [%]	3.90 [%]
χ^2	2.06	2.51	2.48

The color maps underneath all spectra in Fig. 4.4 are model covariance matrices (MCM's). They show the relative variance of the model parameters, as well as the relative correlation of the model parameters amongst each other. It can be seen that the relaxation time τ_1 negatively correlates with the relaxation strength $\Delta\varepsilon_1$ of the free water relaxation process. In contrast, the relaxation time τ_2 correlates positively with the relaxation strength $\Delta\varepsilon_2$ of the interfacial relaxation process. The observation can be explained by the fact that the two relaxations are taking place at the opposite end

of the measured spectrum. Therefore, considering the spectra of $\varepsilon''_{r,eff}$ (Fig. 4.4b,g,l), a shift of the relaxation frequency would go along with an increase or decrease of the relaxation amplitude. Furthermore, the permittivity value in the high-frequency limit ε_∞ positively correlates with the relaxation time of the free water relaxation τ_1, but negatively correlates with the relaxation strength $\Delta\varepsilon_1$. This observation does not surprise, since the permittivity in the high-frequency limit of the soil is primarily controlled on the one hand, by the constant frequency-independent permittivity of the soil matrix and on the other hand by the free water permittivity. Increasing the optical permittivity ε_∞ therefore goes at the expense of a decreased relaxation magnitude $\Delta\varepsilon_1$ and an increased relaxation time τ_1 of free water. The values in brackets behind the parameters in Tab. 4.3 basically show the exact variation for all parameters from the diagonal of the matrix.
Going back to the spectra, it can be observed that the fit of the response model (red line) is in good accordance to the measured data. All spectra (Fig. 4.4b,g,l) quantitatively show which loss mechanism (dc-conductivity or relaxations 1 and 2) does prevail at a certain frequency. Comparing the real parts of the effective electrical conductivity of soil 1 and soil 2 (Fig. 4.4c and Fig. 4.4h), we notice that soil 2 has a much higher electrical conductivity, which has already been found by means of dc-geoelectrical measurements. However, we can also observe that the intermediate-frequency relaxation effect is stronger in soil 2 than in soil 1. This can be explained by the fact that we find much more silt in soil 2 than in soil 1 (73% vs. 19%), which yields a higher inner surface area and therefore, contributes to a more pronounced grain-water interface relaxation effect. Furthermore, in the GPR frequency range above 100 MHz, the losses due to dielectric relaxation mechanisms are higher then the losses due to the dc-conductivity for all investigated soils. The importance of considering also the dielectric relaxation effects in the intermediate frequency range, as low as 100 MHz and beyond, to the intrinsic attenuation is highlighted by means of the clay loam (Fig. 4.4k-o). This clay-loam has a very low electrical conductivity of 4 mS/m compared to the other soils. Nevertheless, the attenuation rate is high with 52 dB/m at a centre frequency of 900 MHz. The model results obtained with the inversion approach indicate that these attenuation rates are predominantly controlled by the intermediate-frequency dielectric relaxation effect, which in turn can be attributed to the amount and mineralogy of clay and silt present in the soil.

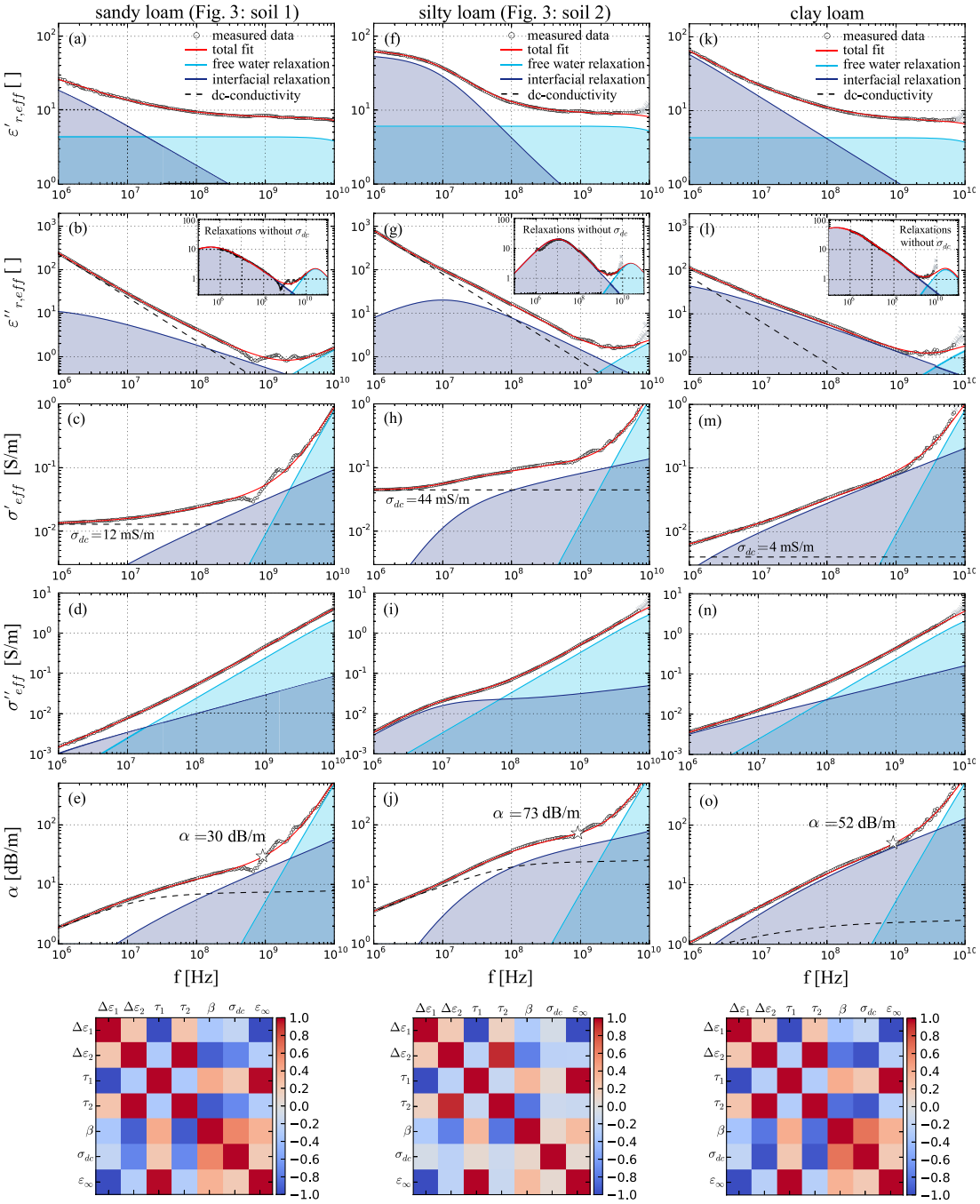

Fig. 4.4.: Real and imaginary part of the complex relative effective dielectric permittivity ($\varepsilon_{r,eff}$), as well as of the complex effective electrical conductivity (σ_{eff}) and the calculated intrinsic attenuation (α) for three different soils. The spectra on the left and in the middle columns refer to soil samples taken from the GPR test lanes (Fig. 4.3). The measured complex permittivity data were inverted by means of a dielectric response model consisting of one Debye- (free water relaxation, light blue) and one Cole-Cole relaxation (interfacial relaxation, dark blue) processes. The influence of the dc-electrical conductivity is marked by the black dashed line. The soils have different grain-size distributions but were measured at almost the same water content. The sub-figures within the spectra of $\varepsilon''_{r,eff}$ show the losses subtracted by the contribution of dc-conductivity. The star in the attenuation spectra denotes the intrinsic attenuation at a frequency of 900 MHz. The color map underneath the spectra are model covariance matrices (MCM's) and show the correlation of the model parameters amongst each other.

Taking into account the inversion results of the 27 soils that we have measured using the CTL technique, we found that for most soils the number of relaxation processes can be limited to one high- and one intermediate-frequency relaxation process considering the GPR frequency band, plus the dc-electrical conductivity loss term. The high-frequency relaxation mechanism (light blue curve) is assigned to the free water polarization and shows relaxation times τ_1 between 5.6 ps and 6.3 ps, which corresponds to frequencies between 25 - 28 GHz. These relaxation frequencies are not typical values for free water hydrogen network fluctuations at the measured room temperature of 23 °C (8.7 ps, corresponding to 18 GHz), as for instance given by Kaatze (2000). However, these lower relaxation times can be attributed to single water molecule relaxation, as mentioned in Wagner et al. (2013) for clay rock. In contrast, the intermediate frequency process is suggested to be linked to different cooperative relaxation mechanisms taking place at the grain-water interfaces. They correspond to polarization effects due to interactions between the aqueous pore solution and mineral phases (e.g. confined and interface water polarization, counter ion relaxation and a distribution of Maxwell- Wagner effects). In recent research, Wagner et al. (2013) determined the Gibbs energy of activation for interface water of a moist clay rock and could show that the processes due to the Maxwell-Wagner effects strongly prevails over the "bound" or interphase water relaxation effects. Thus, the intermediate relaxation process that we observed in our data is probably dominated by the Maxwell-Wagner process while the bound water and the counter-ion relaxation effects play a minor role. The relaxation times τ_2 of the low-frequency process are low with 17 μs to 718 μs, corresponding to relaxation frequencies between 222 Hz and 9.4 kHz. Furthermore, we observed that fine-grained soils show larger relaxation strength $\Delta\varepsilon_2$ than coarser grained soils. The calculated electrical conductivity σ_{dc} in (Tab. 4.3) was compared to geoelectric measurements in the laboratory that were carried out at samples of the same individual soils using a Lippmann 4-point light hp at a measuring frequency of 1 Hz. As a result, only minor differences between the geoelectric measurements and the dc-conductivity from the inversion of our data, could be observed.

4.5. Measuring intrinsic attenuation in the field

The CTL technique in combination with a network analyser can provide broadband spectra of all relevant complex electromagnetic soil properties. They allow for predicting the contrast between the soil and a buried target. Furthermore, they allow for predicting the intrinsic attenuation and thus, the depth of investigation and further characteristics as the sharpness and opacity of the radargrams. Besides the problem of scattering (Igel, 2008; Takahashi and Sato, 2008; Takahashi et al., 2011), which is not discussed in this paper, these features define the performance of GPR and the limitations that are caused by certain soils. However, current developments of the CTL technique are too time-consuming and too complex as it could easily be applied in the

field prior to GPR investigations.

4.5.1. Low versus high-frequency conductivity

In some cases, GPR operators use geoelectrics or electromagnetic methods prior to a field campaign, in order to decide if GPR will succeed at the location (Doolittle et al., 2007). Since these techniques work at much lower frequencies (e.g. in the Hz to kHz range) then GPR, we questioned to what extend these low-frequency measurements can be used in order to forecast the soil response at GPR-frequencies. Based on the laboratory results by means of the CTL technique, we show that measuring the dc-electrical conductivity will not suffice to derive the intrinsic attenuation.
In Fig. 4.5 we plotted the attenuation that was calculated using Eq. 4.7 by considering only the losses due to the dc-conductivity σ_{dc} against the attenuation considering both, σ_{dc} and the losses due to dielectric relaxation, ε_r''. The plot shows the results of 27 different soils each of them measured at various water contents. The samples are grouped according their grain-size distribution using the World Reference Base for Soil Resource (FAO, 2015). The complex dielectric permittivity of all soil samples was measured and the dielectric response model (Eq. 4.8) was used in order to deduce σ_{dc}. Fig. 4.5 shows the result of the attenuation comparison at 6 frequencies between 1 MHz and 4 GHz. The insets show by way of example the attenuation spectrum and the dielectric model decomposition for one soil in order to describe which loss mechanism is expected to prevail at the respective frequency. At a frequency of 1 MHz, the attenuation that considers only σ_{dc} matches very well with the overall attenuation. By increasing the frequency, we see an increasing mismatch between both attenuations. Considering the spectra in each plot, this observation can be attributed to the increasing influence of the dielectric relaxation losses. Therefore, at a frequency of 1 GHz for instance, the overall attenuation would be underestimated by a factor of 4, considering a sand or a sandy loam and the mismatch is in the order of 10 and beyond for silty clay loams. Therefore, low-frequency measurement techniques, which do not consider dielectric relaxation, cannot be used to determine intrinsic soil attenuation. This holds particularly for high-frequency GPR applications and for soils with higher silt and clay contents.

4.5.2. Measuring intrinsic attenuation using TDR

As low-frequency techniques are not suitable, we considered time-domain reflectometry (TDR) as a tool that can be used in the field to determine intrinsic attenuation. The technique generally uses voltage pulses, with bandwidth from kHz to some GHz. A comprehensive review of the method can be found in Robinson et al. (2003). In most cases TDR is used as a soil moisture sensor in the field. In analogy to GPR the TDR pulse propagates with a velocity that depends on the real dielectric permittivity of the soil. However, in the same analogy, the decay of the pulse amplitude travelling along

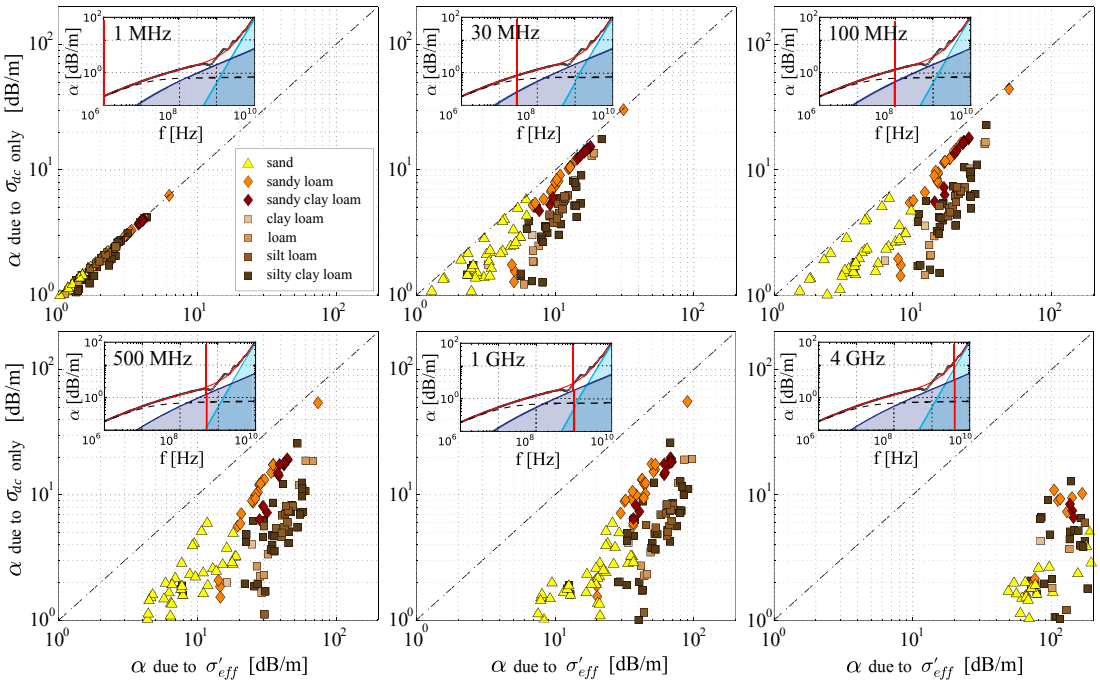

Fig. 4.5.: Attenuation calculated from σ_{dc} only vs. attenuation taking also dielectric losses into consideration for 6 frequencies from 1 MHz - 4 GHz. A number of 27 soil samples, grouped by their grain size distributions are shown. Complex dielectric permittivity of all soil samples was measured using the CTL technique. In order to deduce σ_{dc}, a dielectric response model was fitted. Depicted is the result of the attenuation comparison at 6 different frequencies. The insets show by way of example the attenuation spectrum and the dielectric model decomposition for one soil.

the TDR rods can be used to determine the attenuation of the soil. With respect to high-frequency GPR application, a TDR system with a effective measuring frequency at approximately 1 GHz was needed. We found a commercial available unconventional amplitude sampling TDR system that uses the first total reflection from the end of the probe, but also the relative variation of the TDR voltage amplitude at that reflection in order to calculate high-frequency parameters travel time and corresponding attenuation. In contrast to conventional sampling TDR systems, the wires are coated in order to span the application area of the TDR system to salty environments. The coating acts as a high-pass filter, cutting of all low-frequency content from the voltage pulse (Stacheder, 1996).

Fig. 4.5 shows the comparison between the TDR amplitude, which has been measured using a TRIME Pico 64 TDR-sensor in combination with the HD2 mobile moisture meter (IMKO GmbH, Ettlingen, Germany, www.imko.de) and the intrinsic attenuation (in dB/m) at 1 GHz frequency derived from the CTL method for different materials. The regression curve in Fig. 4.6 shows how well these parameters correlate. The attenuation can be calculated from the TDR amplitude (A_{TDR}) by using the regression curve

$$\alpha = 228 - 2.5 \cdot A_{TDR}. \tag{4.9}$$

However, it has to be mentioned that under very heterogeneous soil conditions the results can be misleading as scattering and coupling effects may also influence the TDR amplitude. Furthermore, an increased number of stones in the soil can not only falsify the result, but can also cause trouble with the installation of the TDR probe into the soil. However, in very heterogeneous environments scattering effects will dominate GPR performance penalties and the intrinsic attenuation will play a minor role at these locations.

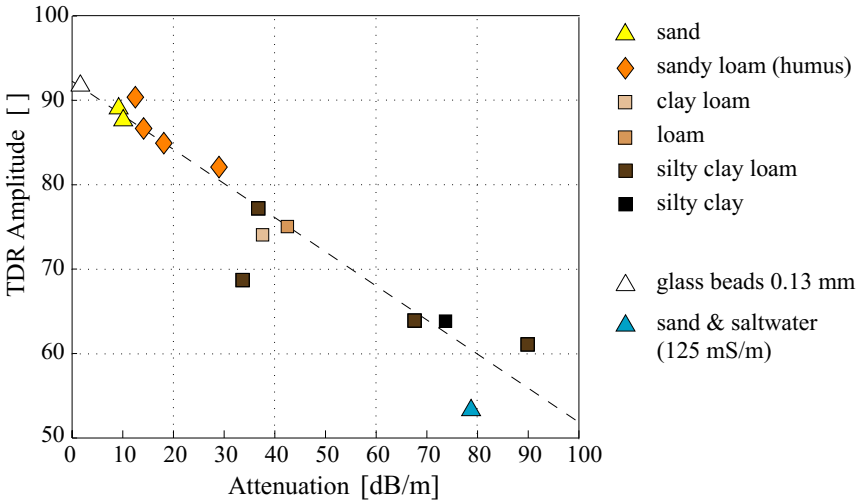

Fig. 4.6.: TDR amplitude exported from TRIME Pico 64 soil moisture TDR-sensor for different soils and materials plotted against the intrinsic attenuation at 1 GHz. The attenuation of the materials has been measured using the CTL technique. The dashed line refers to a regression curve that describes the general correlation between both parameters.

4.6. Conclusion

Our laboratory investigations using the CTL method span a variety of soils with different texture (particle size distribution), structure (bulk densities) mineralogy as well as water contents between dry and nearly full saturation. We found that even in sandy soils we will have dispersion in the attenuation spectra and a "GPR plateau" can only be observed in pure sand. This should be considered for example in simulation of EM wave propagation. The attenuation analyses of our samples show that relaxation effects due to free water, interphase water as well as interfacial processes such as Maxwell-Wagner cannot be neglected in high-frequency GPR applications. In the GPR frequency range, the measured permittivities can be fitted by two polarization processes and a dc-conductivity term. Due to the representative volume of 45 cm^3 of our coaxial line cell and the broad frequency spectrum of the measurement, we are able to accurately measure the complex dielectric permittivity of soils. The dc-conductivities from the model fit are comparable to the direct measurements of conductivity with a laboratory 4-point geoelectric device at 1 Hz. Furthermore, we could confirm that in the GPR

frequency range the intrinsic attenuation is not only controlled by the dc-conductivity, but strongly influenced by dielectric relaxation losses. Based on the laboratory results, we found a field method for the prediction of the GPR performance by measuring the intrinsic attenuation using TDR.
As for the relaxation model fit, we are going to extend the frequency spectra to low frequencies, in order to confirm the relaxation frequency and amplitude of the observed relaxation processes. This will allow to determine the low frequency relaxation taking place at the mineral-water interface more accurately and accordingly to get more accurate relaxation models.

5. A combined permittivity and conductivity model (CPCM)

This is a pre-copyedited, author-produced version of an article accepted for publication in Geophysical Journal International following peer review. The version of record, Loewer, M., Günther, T., Igel, J. Kruschwitz, S., Martin, T. & Wagner, N. (2017): Ultra-broadband electrical spectroscopy of soils and sediments – A combined permittivity and conductivity model, Geophysical Journal International, 210(3), pp. 1360-1373, is available online at: https://doi.org/10.1093/gji/ggx242.

Abstract

We combined two completely different methods measuring the frequency-dependent electrical properties of moist porous materials in order to receive an extraordinary large frequency spectrum. In the low frequency (LF) range, complex electrical resistivity between 1 mHz and 45 kHz was measured for three different soils and sandstone, using the spectral induced polarization (SIP) method with a four electrode cell. In the high frequency (HF) radio to microwave range, complex dielectric permittivity was measured between 1 MHz and 10 GHz for the same samples using dielectric spectroscopy by means of the coaxial transmission line (CTL) technique. The combined data sets cover 13 orders of magnitude and were transferred into their equivalent expressions: the complex effective dielectric permittivity and the complex effective electrical conductivity. We applied the Kramers-Kronig relation in order to justify the validity of the data combination. A new phenomenological model that consists of both, dielectric permittivity and electrical conductivity terms in a Debye- and Cole-Cole type manner was fitted to the spectra. The combined permittivity and conductivity model (CPCM) accounts for the most common representations of the physical quantities with respect to the individual measuring method. A maximum number of four relaxation processes was identified in the analysed frequency range. Amongst these are the free water and different interfacial relaxation processes, the Maxwell-Wagner effect, the counterion relaxation in the electrical double layer and the direct-current electrical conductivity. There is evidence that free water relaxation does not affect the electrical response in the SIP range. Moreover, direct current conductivity contribution (bulk and interface) dominates the losses in the LF range. Interfacial relaxation processes with relaxations in the HF range are broadly distributed down to the LF range. The slowest observed process in the LF range has a minor contribution to the HF response.

5.1. Introduction

In an electric field, moist porous materials like soils and sediments show characteristics of both, conductors and dielectrics. In a time-varying field, the dominant characteristic of the medium can vary with respect to frequency. This variation primarily depends on the water content and the amount of mobile and bound charge carriers in the medium. It therefore determines not only the outcome of any geoelectrical or electromagnetic survey, but also helps us to predict certain media characteristics from the response of the medium to the time-varying fields. Much work has been done in the past in order to determine the nature and frequency range of the underlying processes of this response in different kind of geological materials (e.g. Knight and Nur, 1987; Chelidze et al., 1999; Lesmes and Frye, 2001; Santamarina et al., 2001; Binley et al., 2005; Kupfer, 2005; Chen and Or, 2006; Leroy and Revil, 2009; Revil and Florsch, 2010; Kemna et al., 2012). However, the interaction of EM fields with moist soils and sediments and the underlying processes behind their response are still debated (e.g. Ishida et al., 2000; Weller et al., 2013; Revil, 2014; Weller et al., 2014, 2016). Kremer et al. (2016) recently modeled the SIP response of saturated sandstone between the 100 Hz and 10 kHz frequency range and found that the Maxwell-Wagner effect cannot explain the high response values in the transition range between low-frequency (LF) and high-frequency (HF) polarization alone.
At HF, conventional field moisture sensors, which are primarily based on electromagnetic (EM) wave propagation techniques like time-domain reflectometry (TDR) rely on petrophysical relations and on proper calibration for the individual soil type in order to derive the true water content of the soil (Topp et al., 1980; Roth et al., 1990; Schwartz et al., 2009). The same generally applies to sensing techniques like ground-penetrating radar (GPR), which try to monitor and map the temporal and spatial variations of the subsurface physical state parameters (e.g., Huisman et al., 2003; Igel et al., 2013a; Loewer and Igel, 2016). The main reason for that laborious principle with the requirement of calibration models is that the electrical and dielectric response of a moist material is strongly frequency-dependent and changes with respect to its physico-chemical composition (e.g., Robinson et al., 2003; Kelleners et al., 2005; Loewer et al., 2016b).

In the HF range, between MHz and microwave frequencies, investigations of the complex dielectric properties of moist porous materials are predominantly carried out using dielectric spectroscopy by means of the coaxial transmission line technique (CTL) together with a vector network analyser (an overview can be found in Kupfer and Wagner (2013) or Olmi and Bittelli (2016)). Most of the studies primarily focus on the precise knowledge of the moisture content and the different water states. However, in order to assess all interdependencies of moisture measurements, factors like temperature, texture, pressure, hydraulic state, matric potential, clay content and mineralogy were varied under controlled laboratory condition in preceding studies (Wagner and Scheuermann, 2009; Wagner et al., 2011; Lauer et al., 2012; Wagner et al., 2013).

In contrast to the HF measurements, research that covers the LF side of the spectrum generally focuses on information about the characterisation of the host material. The spectral induced polarization (SIP) technique, which measures the complex electrical resistivity in the mHz to kHz frequency range tries to derive hydro-geological parameters like average pore throat diameter, specific internal surface, grain size distribution, porosity and permeability of the sample from its complex electrical EM response (e.g., Lesmes and Morgan, 2001; Binley et al., 2005; Börner, 2009; Kemna et al., 2012; Kruschwitz et al., 2016).

However, both methods are rarely combined. One of the reasons is that the HF and LF measurement techniques naturally focus on different media properties by measuring different physical quantities at nearly opposing sides of the EM spectrum. However, measurement techniques are getting more and more precise due to the elimination of parasitic effects like the electrode polarization. Two- and four-electrode impedance methods can nowadays measure up to the MHz frequency region as shown by Volkmann and Klitzsch (2015). Therefore, a joint method of interpreting the ultra-broadband spectra becomes necessary.

Fortunately, the way of interpreting the results of the individual methods has an important characteristic in common. The relaxation phenomenon, which is a consequence of the time lagged response to the changing EM field. The first theoretical explanation of a response function dates back to the seminal work of Debye (1929). The theory according to Debye is based on Einsteins theory of rotational Brownian motion of polar molecules like water. He related the relaxation time τ as the time that is required for the dipole moments of the molecules to revert to a random distribution after switching off the applied field assuming no interaction between the molecules (Coffey, 1980). In both measurement principles however, the dispersive data are commonly fitted by different kind of phenomenological models (Tarasov and Titov, 2013; Weigand and Kemna, 2016). The most prominent and more flexible counterparts of the Debye model with additional shape factors are the Cole-Cole model, the Cole-Davidson model, the Havriliak-Negami model and the Jonscher model (e.g. Börner, 2009; Grosse, 2014). All relaxation models are characterised by a mean relaxation time, a relaxation strength or chargeability and symmetrical or asymmetrical shape factors that describe the broadness of the relaxation time distribution. Hilfer (2002) gives an theoretical justification of the appropriate empirical developed relaxation model, based on the theory of fractional time evolutions. Dissado and Hill (1987) suggested a theory based on hirachically coupled relaxation processes leading to a relaxation time distribution that explain the deviation from the Debye-type relaxation pattern.

For HF measurements like with the CTL technique, the relaxation models are commonly expressed in terms of the complex dielectric permittivity. For LF measurements as SIP, they are commonly expressed using the complex electrical resistivity and phase or the complex electrical conductivity. The relaxation times, strengths and shape factors, which are derived by the fitting process, are then correlated with different petrophysical or hydrophysical parameters. However, the complex nature of

a moist porous material is responsible for various dielectric and electrical dispersion phenomena overlapping each other and spanning beyond the measurement ranges of the individual measurement techniques. Therefore, fitting a spectrum with limited bandwidth can result in large uncertainties, which can be reduced by interpreting a much broader spectrum. We illustrate that CTL and SIP data can complement each other, even so they apparently measure different physical quantities in a completely different way. Furthermore, we show that the most commonly used models of each individual technique can be combined in order to receive an accurate yet simple phenomenological model that complies with causality in an extraordinary large frequency range.

5.2. Theory

So far, no universal physico-chemical model has been developed that enables to explain the broadband frequency-dependent response of moist soils and sediments in an EM field (Tarasov and Titov, 2013), even though some well-developed approaches for certain materials exist (e.g. Lesmes and Morgan, 2001). Revil (2013) developed an ultra-broadband model for unsaturated media consisting of three domains, which are separated by a critical frequency at LF and at HF in order to account for a characteristic frequency-dependent behaviour. However, the postulated plateau-like domain in the intermediate part of the quadrature conductivity could not be observed in our data.

5.2.1. A phenomenological description

In contrast to these approaches, the scheme in Fig. 5.1 generally reflects the typical and most common way of analysing and interpreting dispersive dielectric and electrical data: A decomposition into phenomenological models (e.g. of Debye or Cole-Cole types) expressed by generalized electrical or dielectric relaxation functions, which enable to explain the observed dispersive signature of the data. The basic difference between the SIP and CTL method are the physical quantities they measure and the frequency range in which the individual relaxation phenomena are pronounced. In consolidated porous media and in the absence of conductive minerals, we commonly observe one or two dominant peaks (τ_3, τ_4) at LF, in the effective quadrature conductivity σ''_{eff} (grey lines; Kruschwitz et al., 2016).

At the HF side of the spectrum, the dielectric characteristic of the material becomes dominant, since conductive processes decline. The transition range between LF and HF, therefore depicts the frequency band, where conductive and dielectric processes are both pronounced, but where dielectric phenomena start to prevail over conductive phenomena with increasing frequency. Between the MHz and lower GHz ranges, we observe one or two additional relaxation peaks. However, the relaxation times (τ_1, τ_2) of these processes are commonly identified in the effective quadrature permittivity

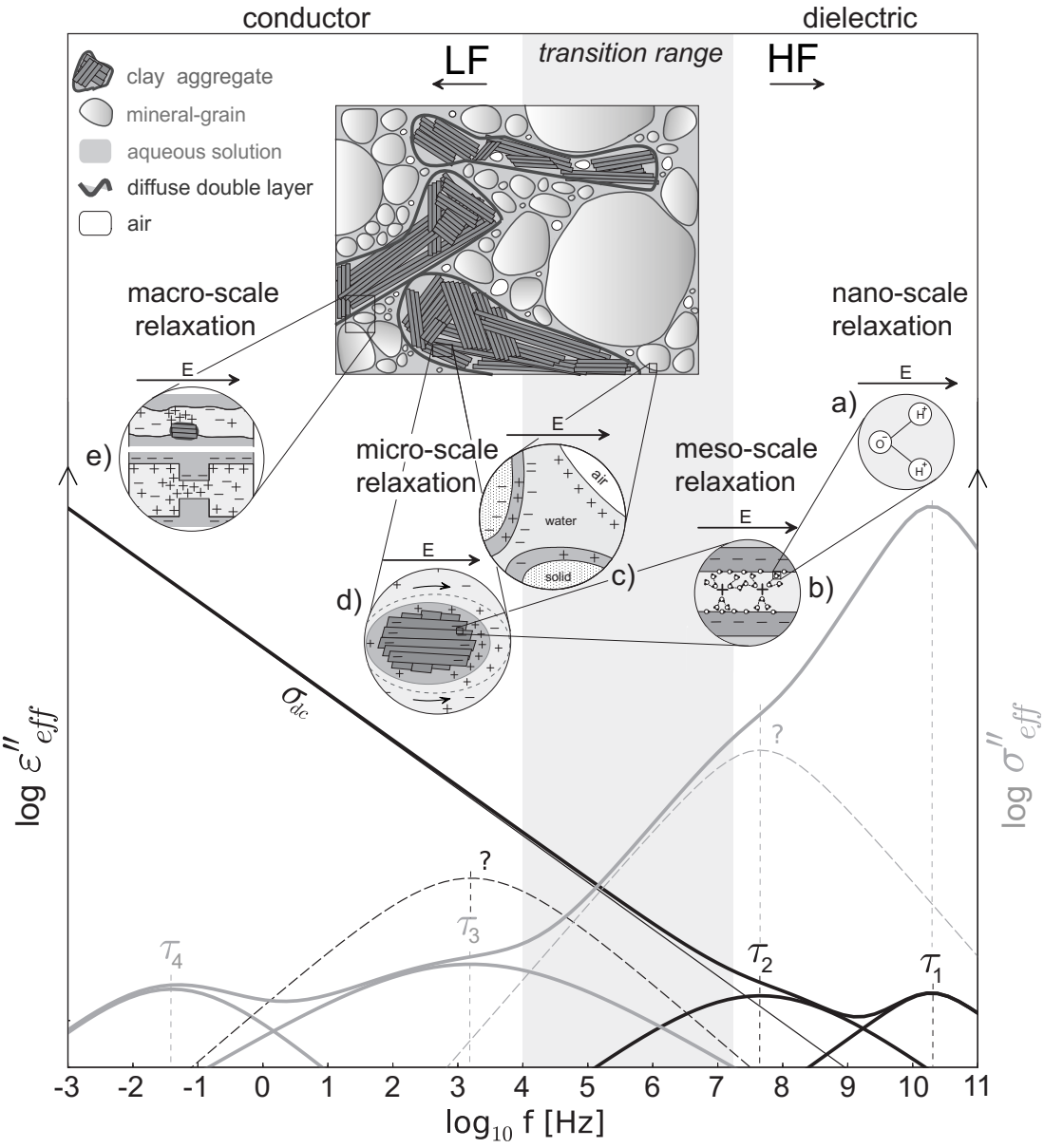

Fig. 5.1.: Interpreting dispersive soil and sediment data using phenomenological models in the SIP method at LF (by means of the effective quadrature conductivity, grey line) and by the CTL method at HF (by means of the effective quadrature permittivity, black line). Two relaxation processes (τ_1, τ_2 at HF and τ_3, τ_4 at LF) are identified in the specific frequency range of the individual measuring techniques. Processes beyond the individual frequency range are barely resolvable (question marks). The relaxation phenomena occur at different spatial scales of the porous multi-phase medium (a: free water dipole relaxation, b: adsorbed water and HF counterion relaxation, c: Maxwell-Wagner effect, d: double layer relaxation, e: membrane relaxation; after Sposito and Prost, 1982; Titov et al., 2002; Wagner et al., 2007; Revil and Skold, 2011; Schön, 2015; Schwing, 2015, p.49).

ε''_{eff} (black lines). At LF, the quadrature permittivity and all its underlying relaxation phenomena become dominated by the direct-current electrical conductivity σ_{dc}. The strong increase in the effective quadrature conductivity of the SIP data above 10 kHz

is caused by the relaxations that are taking place at HF (τ_2 and τ_1). However, the relaxation strength and times and especially the broadness of the HF process (τ_2) cannot be resolved with the SIP method (indicated by the dashed grey relaxation process). However, since the processes in the transition range (τ_2 and τ_3) overlap each other, the choice of the τ_2-relaxation parameters can strongly effect the relaxation parameters of process τ_3 and vice versa. The same applies to the CTL method at HF and the relaxations that are taking place below its frequency range at LF (dashed black relaxation process). In order to resolve these overlapping relaxation processes (τ_3, τ_2) the SIP and CTL methods are combined and fitted by means of a combined relaxation model.

5.2.2. Physical processes

The physical explanation for the relaxation phenomena occurring in a certain frequency range are commonly done in further steps, independent from the phenomenological models. The scheme in Fig. 5.1 indicates that each relaxation mechanism does not only have a certain time-scale, but also a characteristic spatial scale (macro-scale to nano-scale) that is related to the size of the polarizing units in the complex multi-phase material. The smaller the mass or scale involved, the higher becomes the characteristic relaxation frequency (Santamarina et al., 2001, pp. 360–361).

There is a huge amount of simplified physical descriptions and models available that account for the different polarization and relaxation mechanisms in moist porous media. Overview is given by Hasted (1973), Santamarina et al. (2001), Kupfer (2005) and Comparon (2005). For moist soils and sediments at room temperature and at atmospheric pressure in the frequency range up to 100 GHz, the physical processes can be reduced to the following (see also Fig. 5.1):

1. the dipolar orientational relaxation of free and immobile water (sketch a in Fig. 5.1, nano-scale, τ_1-peak; see Kaatze, 2000),

2. the dipolar orientational relaxation of physically bound and hydrated water at the mineral-water interfaces (GHz range; see Hoekstra and Doyle, 1971; Ishida et al., 2000; Polizos et al., 2013), together with the relaxation processes referred to as adsorption/desorption rates of counterions in clay interlayers with relaxation times in the range between 2 and 8 ns (sketch b in Fig. 5.1, meso-scale, τ_2-peak; see Rotenberg et al., 2005),

3. the distribution of different spatial relaxations that occur at the interface of spatially separated phases, as for instance in media with spheroidal inclusions or in systems with spherical particles (Maxwell-Wagner type, sketch c in Fig. 5.1, micro-scale, τ_3-peak, kHz–MHz range; see Knight and Nur, 1987; Santamarina et al., 2001, pp.352–355),

4. the counterion relaxation taking place in the inner (Stern) and outer (diffusive) electrical double layer (EDL) along the surfaces of grain minerals (e.g. Schwarz,

1962; Revil and Skold, 2011) and clay aggregates (sketch d in Fig. 5.1, micro-scale, τ_3-peak, Hz–kHz range; see Ishida et al., 2000),

5. the membrane relaxation (short and long narrow pore polarization) (sketch e in Fig. 5.1, macro-scale, mHz to lower kHz range (lower micro-scale), τ_4- and possibly τ_3-peak; see Marshall and Madden, 1959; Bücker and Hördt, 2013)

6. the electrode polarization in the presence of conductive minerals (not shown in this study) with very different relaxation times, depending on the particle size, mineral type and solution conductivity (e.g. Gurin et al., 2015; Mao et al., 2016)

7. the quasi-direct current electrical conductivity due to the free flow of charged particles in the bulk solution and at interfaces (σ_{dc}; e.g. Schön, 2015).

Our inverse modelling approach suggests between three and four dispersive processes that are dominating a certain range within the frequency band of 1 mHz and 10 GHz. In order to apply a combined relaxation model on the combination of SIP and CTL data, we transferred all quantities into effective parameters (as already indicated in Fig. 5.1).

5.2.3. Complex effective electrical parameters

Due to the changing nature of the response to a time-varying EM field with respect to frequency, the response of each method is typically represented by different physical quantities. We use the complex relative dielectric permittivity to describe HF processes, where the capacitive or dielectric character generally prevails:

$$\varepsilon_r^*(\omega) = \varepsilon_r'(\omega) - i\varepsilon_r''(\omega) \tag{5.1}$$

where ε_r' and ε_r'' are the real and imaginary parts of the complex relative dielectric permittivity ε_r^* that is normalized by the vacuum permittivity $\varepsilon_0 = 8.854 \times 10^{-12}$ F m^{-1} and ω is the angular frequency and $i = \sqrt{-1}$ the imaginary unit. In contrast, LF measurements by means of SIP are expressed by the complex resistivity ρ^* (in Ω m):

$$\rho^*(\omega) = |\rho(\omega)|e^{i\varphi(\omega)} = \rho'(\omega) + i\rho''(\omega) \tag{5.2}$$

with the resistivity magnitude

$$|\rho(\omega)| = \sqrt{\rho'(\omega)^2 + \rho''(\omega)^2}, \tag{5.3}$$

where φ is the phase shift (in rad) between real (ρ') and imaginary part (ρ'') of the complex resistivity ρ^*, given by:

$$\varphi(\omega) = tan^{-1}\left[\frac{\rho''(\omega)}{\rho'(\omega)}\right]. \tag{5.4}$$

In order to express conduction and displacement currents in our samples with respect to frequency, we transferred all quantities into the constitutive parameters ε^* and the complex electrical conductivity σ^* (in S m^{-1}):

$$\sigma^*(\omega) = \rho^*(\omega)^{-1} \tag{5.5}$$

The HF data (CTL) are represented by means of the complex relative dielectric permittivity ε_r^*, whereas the LF data (SIP) are expressed in terms of the complex electrical conductivity σ^*. The basis of putting both data sets together is the fact that the measured quantities are no true quantities, but only combinations of these (Fuller and Ward, 1970). This means, both quantities contain elements of loss and energy storage and therefore of conduction and displacement currents. They can be equivalently expressed as total or complex effective (measured) quantities either in terms of permittivity (Knight and Endres, 2005):

$$\begin{aligned} \varepsilon^*_{r,eff}(\omega) &= \left[\varepsilon'_r(\omega) + \frac{\sigma''(\omega)}{\omega\varepsilon_0}\right] - i\left[\varepsilon''_r(\omega) + \frac{\sigma'(\omega)}{\omega\varepsilon_0}\right] \\ &= \varepsilon'_{r,eff}(\omega) - i\varepsilon''_{r,eff}(\omega) \end{aligned} \tag{5.6}$$

or conductivity:

$$\begin{aligned} \sigma^*_{eff}(\omega) &= \left[\sigma'(\omega) + \omega\varepsilon_0\varepsilon''_r(\omega)\right] - i\left[\sigma''(\omega) + \omega\varepsilon_0\varepsilon'_r(\omega)\right] \\ &= \sigma'_{eff}(\omega) - i\sigma''_{eff}(\omega), \end{aligned} \tag{5.7}$$

with the relation

$$\sigma^*_{eff}(\omega) = i\omega\varepsilon_0\varepsilon^*_{r,eff}(\omega) \tag{5.8}$$

and $\varepsilon^*_{r,eff}$ and σ^*_{eff} are called the complex effective relative dielectric permittivity and the complex effective electrical conductivity.

5.3. Materials and Methods

We measured and analysed three moist soils and one saturated sandstone using the combined LF and HF techniques. The investigated materials span a wide range of materials with some interesting physico-chemical characteristics. We expect that some of these characteristics can be interpreted from the measured EM spectra.

5.3.1. Materials

Soil A (loess) is a silty clay, whose major mineral component is quartz (see Tab. 5.1). The loess has the highest cation exchange capacity (CEC) of the analysed soils, which is due to the swellable layer silicates (vermiculite and smectite group). The grain size

analysis shows a poorly sorted clay and silt fraction (Fig. 5.2).

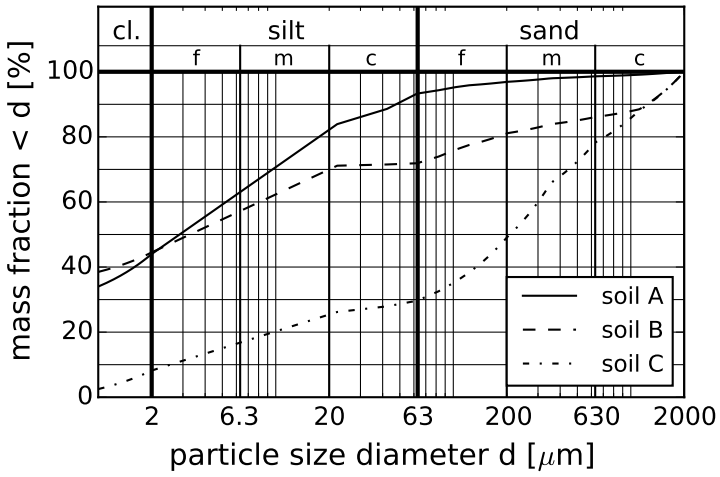

Fig. 5.2.: Grain-size analysis of the three soil samples showing per cent mass fractions of clay (cl.) and fine (f), medium (m) or coarse (c) silt and sand. The measurements were carried out by sieving (particles size diameter d $\geq$ 63 μm) and by the sedigraph method (for d $<$ 63 μm).

Soil B (laterite) is a clay, whose major and minor mineral components are quartz, gibbsite and hematite. The latter gives the laterite its typical red color. The soil has the highest clay content among the investigated samples, however the CEC is only at intermediate level. This is because the material has undergone extensive chemical weathering resulting in high kaolinite and gyppsite contents which have lower CEC than unweathered clay minerals. Instead, x-ray spectroscopy (EDX) and scanning electron microscopy (SEM) suggest an increased amount of titano-magnetite and magnetite traces. Both, its magnetic susceptibility κ_{LF} and the total frequency-dependence $\Delta\kappa$ thereof are considerably increased.

Soil C (humus) predominately consists of poorly sorted sand and to 30% of silt and clay, which come from a silicatic, calcitic or carbonatic origin. The CEC of the humus is very small and the magnetic properties are negligible. However, its total carbon content C_{tot} of 5% is increased. All soils were measured at in-situ volumetric water content θ_v between 30% and 37%. In contrast to the sandstone sample, the fluid salinities of the soils were unknown. The water contents and bulk densities ρ_b (in g cm^{-3}) had been calculated after oven drying of the measured samples at a temperature of 105 °C for 24 hours.

The Obersulzbacher (OBS) sandstone is a German sandstone from the Perm formation. It is quarried in Sulzbachtal, Germany, about 10 km north of Kaiserslautern (Rhineland-Palatinate). It is a pale yellowish fine to medium grained sandstone that consists of 52% quartz, 40% fragments, 7% feldspar and 1% accessories like muscovite and biotite. The cementation is mostly kaolinitic or ferritic. The physical properties of the sandstone shows Tab. 5.2. The porosity is relatively high (ϕ = 0.208) in

Tab. 5.1.: Physical and chemical properties of the three soil samples. The texture class is due to USDA (1987). The cation exchange capacity (CEC) was measured using the Cutriene method (Cu2+/CEC). The porosity ϕ was calculated assuming a particle density of 2.65 g cm^{-3}. The x-ray diffraction (XRD) shows major, minor and fractal components of minerals ([1]or smectite, [2]from x-ray spectroscopy (EDX) and scanning electron microscopy (SEM), [3]close to the detection limit). The volume specific susceptibility κ_{LF} (in 10^{-5} SI) has been measured using the MAGNON VFSM between 505 Hz and 5005 Hz. The total and relative frequency-dependence of κ_{LF} is given by $\Delta\kappa$ and κ_{FD}.

	soil A (loess)	soil B (laterite)	soil C (humus)
texture class	silty clay	clay	sandy loam
clay [%]	44.0	44.5	8.2
silt [%]	49.4	27.4	21.5
sand [%]	6.7	28.1	70.4
θ_v [%]	35.82	30.29	36.82
ρ_b [g cm^{-3}]	1.68	1.38	1.58
ϕ [%]	36.60	47.92	40.38
CEC [meq/100g]	18.5	5.2	0.5
C_{tot} [%]	0.26	0.38	5.41
pH (H_2O)	7.97	7.59	9.19
XRD major + minor components	quarz	quarz, gibbsite, hematite	quartz, calcite, dolomite
XRD traces	feldspar, musc.-illite, vermiculite[1], kaolinite	goethite, kaolinite, magnetite[2], titano-mag.[2]	feldspar, musc.-illite[3], chlorite[3]
κ_{LF} [10^{-5} SI]	39	3831	39
$\Delta\kappa$ [10^{-5} SI]	2	223	3
κ_{FD} [%]	5.1	5.8	7.7

comparison to the maximum porosities of Barea, Fontainebleau or Bunter sandstone (Schopper, 1982). In contrast and with respect to the high porosity, the permeability of k = 2.59 mD (with 1 Darcy [D] = 10^{-5} ms^{-1}) is relatively low. The OBS sandstone sample therefore, corresponds to a rather well sorted and fine-grained sandstone (Nelson, 1994). The formation factor F* was estimated from a multi-salinity measurement of the sandstone using the slope of a linear plot between the bulk resistivities ρ_0 of the fully saturated samples and the saturating fluid resistivities ρ_w (Waxman and Smits, 1968). We derived the cementation exponent m according to Archie's law with F* = aϕ^{-m} using a tortuosity factor a = 1 (Archie, 1942). According to Schön (2015), the calculated cementation factor of m = 2.19 corresponds to a highly cemented sandstone, which also matches the low permeability value. The magnetic susceptibility κ_{LF} is much lower in comparison to the soils. The total and relative frequency-dependence thereof are negligible. The sample has been oven dried at 40°C until weight stability prior to saturation. For the measurements it was saturated with NaCl fluid of 0.1 S/m in a desiccator.

Tab. 5.2.: Physical properties of the Obersulzbacher (OBS) sandstone. The porosity ϕ was measured using mercury intrusion porosimetry and S_{sp} by means of the BET method. The permeability was measured using a nitrogen-permeameter ([1]mean matrix density, [2]mean bulk density, [3]no representative mass).

Property	Value
Porosity ϕ [%]	20.79
Permeability k [mD]	2.59
Formation factor F^* [-]	31
Archie exponent m[-]	2.19
Specific surface area S_{sp} [m^2g^{-1}]	2.679
Grain density[1] ρ_s [$g\,cm^{-3}$]	2.65
bulk density[2] ρ_b [$g\,cm^{-3}$]	2.15
CEC[3] [meq/100g]	<2
magnetic susceptibility κ_{LF} [10^{-5} SI]	5
total frequency-dependence $\Delta\kappa$ [10^{-5} SI]	0
relative frequency-dependence κ_{FD} [%]	0.0

5.3.2. Measuring technique

Investigations of the EM properties for moist porous materials from LF to the microwave range are sparsely made (examples and references therein can be found in Comparon (2005), Wagner et al. (2007), Börner (2009), Revil (2013) or Bobrov et al. (2015)). One of the reasons is that with respect to frequency certain measurement techniques become not only advantageous over others, but they become necessary in order to avoid different kind of EM losses. Unfortunately, the change of a measuring technique commonly comes along with the change of the measuring cell in which the soil sample is embedded. In the HF range, coaxial cables and cells become necessary in order to avoid cable power losses due to the deploying radiation of the EM energy. On the other hand, LF measurements with HF techniques are limited by the cell size and geometry (e.g. ratio of the wavelength to the electric component length). Therefore, in order to measure the EM response spectrum from the mHz to the GHz frequency range of a sample, two different measuring techniques with two different cells were used.

For the LF measurements (1 mHz to 45 kHz) of complex resistivity we used the ZEL-SIP04-V02 impedance meter (Forschungszentrum Jülich). It has very high phase accuracy of 0.25 mrad up to 10 kHz (Zimmermann et al., 2008). The sample cell was developed by the Federal Institute for Materials Research and Testing (BAM) in Berlin. The configuration consists of a four-electrode arrangement, with two conduction current electrodes at the outer ends and two potential ring electrodes in between. Further information on the geometry of the SIP cell is described by Kruschwitz (2008) and Martin et al. (2015).

The HF measurements were carried out in the frequency range between 1 MHz and 10 GHz using a 2-port coaxial transmission line (CTL) together with a R&S ZVL13 vector network analyzer. The coaxial cell in witch the materials had been embedded

consists of an outer and inner conductor made from copper with a volume of 42.3 cm^3. In order to avoid leakage of the moist samples, each side of the cell was sealed with teflon disks. A detailed description of the coaxial cell and the utilized cell holders can be found in Lauer et al. (2012) and Wagner et al. (2013). The CTL technique generally measures the complex reflection and transmission parameters (scattering or S-parameters) of the device under test. We used a combination of the quasi-analytical propagation matrix (PM) method (1-200 MHz; Gorriti and Slob, 2005c) and the fast transmission method (200 MHz-10 GHz; Agilent, 2014) in order to derive the complex dielectric permittivity from the scattering parameters.

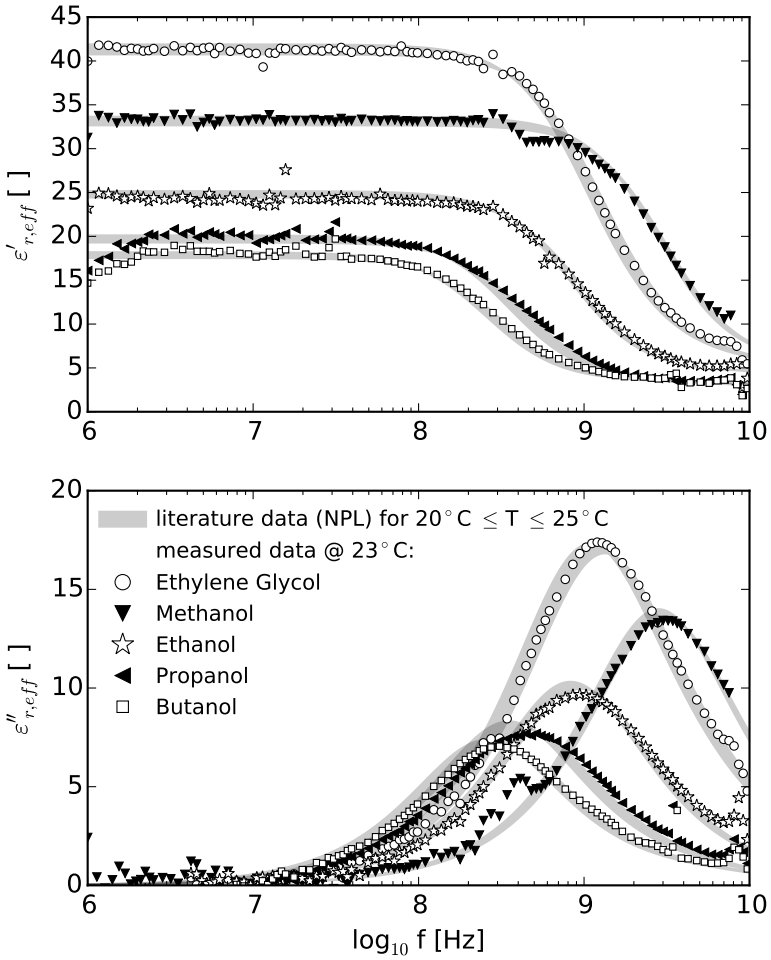

Fig. 5.3.: Real- and imaginary part of the dielectric permittivity of alcohols measured using the CTL technique at 23 °C in comparison with literature data for temperatures between 20° and 25°C (Gregory and Clarke, 2012).

5.3.3. Quality control

The investigated polarization effects at LF are usually in the order of a few milliradians, which for the SIP measurement setup is slighty greater than their standard deviation (Kruschwitz, 2008). Therefore, considerable effort was put into the SIP sample holder design to ensure accurate resistivity measurements of both saturated and unsaturated specimen. However, in case of unsaturated samples it is difficult to maintain adequate electrode coupling. Thus, all samples in this study were measured in relative moist or saturated condition. The accuracy of the SIP measurement setup was validated using calibration standards like water, brine and agar gel samples. Further information on the used SIP cell and data quality at LF is found in Kruschwitz (2008).

Calibration with reference liquids

In order to assess the data quality at HF, we measured different alcohols, whose typical relaxation parameters can be found in the literature (e.g. Gregory and Clarke, 2012). Fig. 5.3 shows the real and imaginary parts of the effective dielectric permittivity of pure alcohols (ethylene glycol, methanol, ethanol, 2-propanol and 1-butanol) that had been measured using the CTL technique (symbols). In comparison with the literature data (grey background), we calculated an RMS deviations of 0.42 for the real and of 0.32 for the imaginary part of the complex effective permittivity ε^*_{eff}, which we consider acceptable.

Kramers-Kronig relation

The soils and the sandstone had been measured by means of the individual method (SIP & CTL) at the same time, in order to avoid variations of the materials chemical state. However, since cells with different size and geometries had been used, the achieved density of the soils in the individual cell can vary. Furthermore, there is no data overlap but a gap between 45 kHz and 1 MHz, where both techniques reached their upper and lower measuring limits. However, the combined dataset (SIP & CTL) covers a continuous frequency spectrum. We transformed both data sets in its equivalent expression (Eqs. 5.6 and 5.7) and interpolated the combined dataset using a spline interpolation function in order to close the data gap between 45 kHz and 1 MHz. We applied the Kramers-Kronig (KK) relation on the interpolated dataset in its complex resistivity representation (Boukamp, 1993; Volkmann and Klitzsch, 2015):

$$\rho'(\omega) = \rho'(\infty) + \frac{2}{\pi}\int_0^\infty \frac{x\rho''(x) - \omega\rho''(\omega)}{x^2 - \omega^2} dx \tag{5.9}$$

and

$$\rho''(\omega) = \frac{2\omega}{\pi}\int_0^\infty \frac{\rho'(x) - \rho'(\omega)}{x^2 - \omega^2} dx. \tag{5.10}$$

The KK relates real and imaginary part of the physical properties to each other and enables to assess the validity of the joint and interpolated data set. Fig. 5.4 shows exemplary on soil A (loess) that the application of the KK relation on the real and imaginary part of the complex resistivity was successful, which applies to all presented data sets of this study. Besides the gap, the KK relation indicates a reasonable agreement

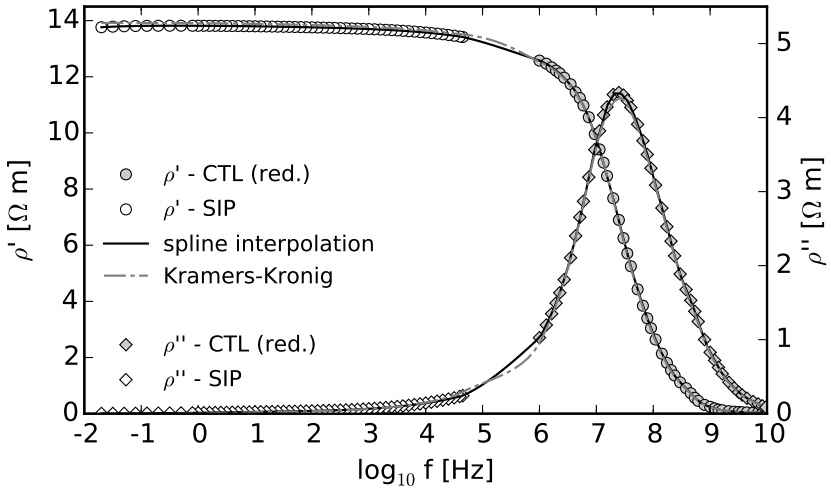

Fig. 5.4.: Real and imaginary resistivity of soil A (loess) measured with the CTL (red.: reduced data density) and the SIP techniques. Interpolation of both data sets using a spline interpolation scheme (black line). Result of the Kramers-Kronig relation applied on the real and imaginary part of the resistivity (dashed grey line).

between the measured and interpolated data, respectively. Data sets, which did not comply with the KK relation had been rejected. Most probable reason for a discrepancy are variations in the installation density or coupling effects at the SIP electrodes (which especially had been observed on unsaturated soil samples).

5.3.4. Combined permittivity and conductivity model (CPCM)

Previous studies have shown that the HF data of moist soils between 1 MHz and 10 GHz can be fitted using a generalized dielectric response model (Wagner and Scheuermann, 2009; Wagner et al., 2011, 2013). In most cases the dielectric model consisted of one Debye term for the relaxation of free water molecules, two Cole-Cole (CC) type models for the bound water and interfacial relaxations or the Maxwell-Wagner effect and a direct-current conductivity term. Loewer et al. (2016a) showed two combined data sets of SIP and CTL measurements for moist soils that can be fitted by three or four dielectric relaxation models, plus one loss term for the dc-conductivity. However, looking very closely to the phase at the LF spectrum between 1 mHz and 10 Hz, the ultra-broadband model that primarily consists of dielectric dispersion terms starts to fail at the lower end of the frequency spectrum. However, this part of the spectrum

naturally carries information on important hydro-geological parameters, which needs to be derived from a high resolution fit of the SIP response. The LF fit by means of CC type dielectric relaxation terms is worsening or even impossible in case of media with larger pore diameters like sandstones.

Generally, dispersive data of any physical quantity, measured with SIP or CTL can be fitted using a Debye decomposition approach, as has been shown by Nordsiek and Weller (2008) and more recently by Ustra et al. (2016). The result is a reasonable characterization of the measured data at the expense of a sum of Debye-type models with numerous free model parameters, which have to be assigned to appropriate petrophysical mechanisms in a second parametrization step of the obtained relaxation time distribution. In contrast, we combined the rather classical and generalized one-step parametrization approach that can be found in both individual methods. We fitted the data using a minimum number of parallel symmetrical dispersion models, preferably of the CC type for hierarchically coupled relaxations and the Debye type for the free water relaxation. The CC equation describes a distribution of relaxation times using a stretching factor, which enables a systematic analysis of the relationship between petrophysical parameters and appropriate model parameters. The new model uses CC or Debye terms based on the dielectric permittivity parameters for the HF range and CC terms based on the chargeability and conductivity parameters for the LF region. Thus, our combined permittivity and conductivity model (CPCM) reads:

$$\begin{aligned} \varepsilon^*_{r,eff}(\omega) &= \varepsilon_\infty + \sum_{k=1}^{K} \frac{\Delta\varepsilon_k}{1+(i\omega\tau_k)^{1-\alpha_k}} \\ &- i\frac{\sigma_{dc}}{\omega\varepsilon_0}\left[1+\sum_{n=1}^{N}\frac{m_n}{1-m_n}\left(1-\frac{1}{1+(i\omega\tau_n)^{c_n}}\right)\right], \end{aligned} \tag{5.11}$$

wherein ε_∞ corresponds to the high-frequency limit of the permittivity, $\Delta\varepsilon_k$ is the relaxation strength (with $\Delta\varepsilon_k = \varepsilon_{0,k} - \varepsilon_\infty$), m_n is the chargeability, $\tau_{k,n}$ is the relaxation time of the individual process, $c_{k,n} \leq 1$ are the stretching exponents (with $c_{k,n} = 1 - \alpha_{k,n}$) and σ_{dc} corresponds to the direct-current electrical conductivity (in S m$^-$1; often denoted by σ_0 at LF). The chargeability is defined by Seigel (1959):

$$m_n = \frac{\sigma_{\infty,n} - \sigma_{dc}}{\sigma_{\infty,n}}. \tag{5.12}$$

The CPCM (Eq. 5.11) can be re-formulated into a sum of classical Cole-Cole equations (Cole and Cole, 1941) in a combined expression of dielectric permittivity and

electrical conductivity terms:

$$\begin{aligned}\varepsilon^*_{r,eff}(\omega) &= \varepsilon_\infty + \sum_{k=1}^{K} \frac{\Delta\varepsilon_k}{1+(i\omega\tau_k)^{1-\alpha_k}} \\ &- \frac{i}{\omega\varepsilon_0}\left(\sigma_\infty - \sum_{n=1}^{N} \frac{\Delta\sigma_n}{1+(i\omega\tau_n)^{c_n}}\right),\end{aligned} \tag{5.13}$$

and equivalently, with respect to Eq. 5.8 the effective complex electrical conductivity (in S m$^-$1) can be expressed as:

$$\begin{aligned}\sigma^*_{eff}(\omega) &= i\omega\varepsilon_0\left(\varepsilon_\infty + \sum_{k=1}^{K} \frac{\Delta\varepsilon_k}{1+(i\omega\tau_k)^{1-\alpha_k}}\right) \\ &+ \sigma_\infty - \sum_{n=1}^{N} \frac{\Delta\sigma_n}{1+(i\omega\tau_n)^{c_n}},\end{aligned} \tag{5.14}$$

wherein $\Delta\sigma_n$ corresponds to the relaxation strength (with $\Delta\sigma_n = \sigma_{\infty,n} - \sigma_{dc}$). The high-frequency limit of all electrical conductivity terms is given by

$$\sigma_\infty = \sigma_{dc} + \sum_{n=1}^{N} \Delta\sigma_n = \sigma_{dc} + \sum_{n=1}^{N} (\sigma_{\infty,n} - \sigma_{dc}). \tag{5.15}$$

Together with

$$\frac{\Delta\sigma_n}{\sigma_{dc}} = \frac{m_n}{1-m_n}, \tag{5.16}$$

we can express Eq. 5.15 in terms of the chargeability as

$$\sigma_\infty = \sigma_{dc}\left(1 + \sum_{n=1}^{N} \frac{m_n}{1-m_n}\right). \tag{5.17}$$

5.3.5. Inverse modelling

For the model fitting, we used data and model represented in the effective complex dielectric permittivity (Eqs. 5.6 and 5.11). The CTL and SIP datasets have different length and frequency step increments (1991 data points over 4 frequency decades for CTL and 60 data points over 6.5 decades for the SIP method). The data sets would therefore have a different weight in the inversion process. In order to accounted for that, we determined a weighting factor that is calculated by the logarithm of the frequency band of the individual measuring method and the data density. The parameterization was carried out by a Levenberg-Marquardt inversion scheme provided by the Python Geophysical Modelling and Inversion Library pyGIMLi (Rücker et al., 2016).

In order to constrain the possible range of the individual model parameters, we used logarithmic functions as described by Kim and Kim (2011) to specify both lower and upper limits. Whereas some of the parameters were naturally constrained ($0 \leq m \leq 1$, $0 \leq c \leq 0.6$, $0.5 \leq \alpha \leq 1$), the ranges for the time constants had to be chosen carefully to avoid confusion between the individual relaxations. Tab. 5.3 shows the used values. The data error consists of an absolute and a relative part accounting for different error sources. Herein, the large-valued LF data are better constricted by the relative error, whereas the fit of the HF data was rather controlled by the absolute error. By trial-and-error, we chose absolute and relative errors of 0.09 and 0.015 for all data sets, respectively. We used a cooling scheme, i.e. the initial Lagrange multiplier $\lambda = 3$ in the Levenberg-Marquardt inversion scheme (Marquardt, 1963) is decreased by 20% in every iteration to improve convergence. In order to decide the best fit, we analysed relative root mean square errors (rRMS) and the chi-square value χ^2 that represents the difference between observed and modeled data.

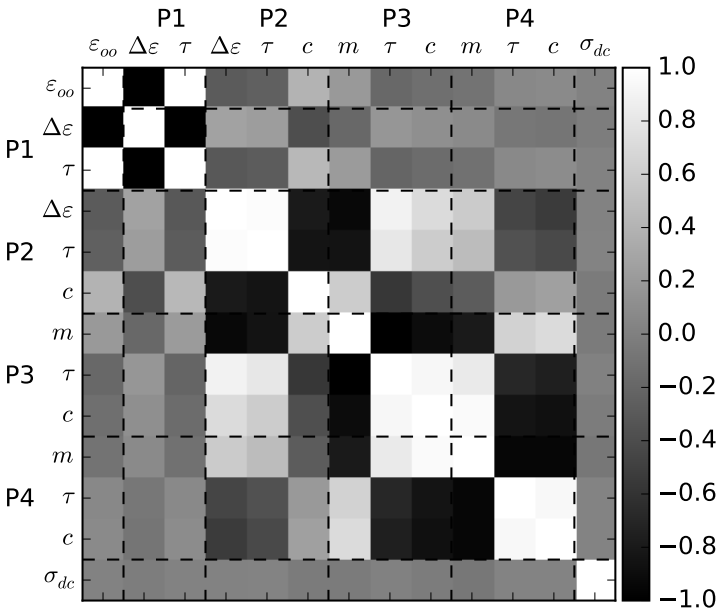

Fig. 5.5.: Model covariance matrix (MCM) showing the CPCM parameter covariances of the inverted complex effective permittivity data for soil A.

Moreover, the model covariance matrix (MCM) was computed and analysed. It provides uncertainties for the individual model parameters and indicates the dependencies among them. Fig. 5.5 shows by way of example the normalized MCM of soil A (loess). The data had been fitted using four relaxation processes (P1 - P4), one constant dielectric permittivity term for very high-frequencies (ε_∞) and a constant dc-conductivity term (σ_{dc}). The common observations in the MCMs of all materials are the strong interdependences of ε_∞ and the HF relaxation process (P1), as well as the independence of σ_{dc} from all other elements. Hence, in process P1 the correlation

between relaxation strength $\Delta\varepsilon$ and ε_∞ is better expressed as $\varepsilon_0 - \varepsilon_\infty$. Further strong covariances are observed amongst the relaxation parameters of each process.

5.4. Results & Discussion

We present all combined spectra in the most common way they are represented in the corresponding measuring technique: on the HF side in terms of the effective complex permittivity and on the LF side in terms of the effective complex electrical conductivity (Figs. 5.6 to 5.9). This is necessary since we are using a mixed model consisting of both, dielectric and electrical relaxation terms. We furthermore show the decomposition of the spectra into different polarization and loss processes. Thus, the peak of an individual relaxation can best be seen in the imaginary part of the corresponding model parameters ($\varepsilon''_{r,eff}$ for HF and σ''_{eff} for LF). Furthermore, due to the large bandwidth and wide span of data values of several orders of magnitude, we plot the data and models with double logarithmic scale. Unfortunately, this logarithmic overall picture can lead to false interpretations since important details are hidden. Therefore, we also present characteristic parts of the data on the semilogarithmic scale. Instead of the effective quadrature conductivity, we show the phase shift φ as given in Eq. 5.4. All fitting parameters for the soils and the sandstone together with the log standard deviation (given in percent in brackets) are given in Tab. 5.3. The accuracy of the fit in the LF range of the real effective conductivity (and quadrature effective dielectric permittivity) cannot be seen in the overall fit of the CPCM model, since all polarization effects are strongly dominated by the dc-electrical conductivity. Therefore, the semitransparent circles in the real effective conductivity of Figs. 5.6 to 5.9 show the data without the dc-electrical conductivity. Furthermore, the free water relaxation (P1) and ε_∞ were subtracted from these data and from the CPCM fit (semitransparent line), in order to highlight the fit of the remaining three relaxations (P2, P3, P4).

5.4.1. Soil A (loess)

The data sets and the fitting results for soil A (loess) are shown in Fig. 5.6. The data quality is very high regarding the smoothness and the low number of spikes (especially at HF) in comparison to all other investigated materials. This is reflected by the small rRMS error of only 2%. The data were inverted using the CPCM including $K = 2$ relaxation processes (Eq. 5.11) in terms of ε (P1 and P2) for HF and $N = 2$ LF relaxation processes in terms of σ (P3 and P4) and the constant parameters ε_∞ and σ_{dc}, which limit the upper and lower end of the $\varepsilon'_{r,eff}$ and σ'_{eff} spectra. We assign the HF process P1 to the relaxation of the free water molecule. With a mean relaxation time of 5.4 ps (corresponding to a relaxation frequency of 29 GHz), it is below the typical relaxation time of pure water at room temperature (8.7 ps or 18 GHz), as given by Kaatze (2000). However, the lower relaxation times of free water in moist porous media (instead of

Tab. 5.3.: Inversion results: upper and lower inversion boundaries, mean value and standard deviation (%) of the fitted model parameters. Fitting error and χ^2 is given at the bottom (* The τ inversion boundary of P2 for the sandstone was shifted to higher relaxation times; see Section 4.4).

			soil A - loess	soil B - laterite	soil C - humus	OBS sandstone
		boundaries				
	ε_∞	2 – 5	2.05 (133.81)	2.08 (49.99)	2.00 (92.50)	2.6 (140.95)
P1:	$\Delta\varepsilon$	1 – 100	15.97 (16.80)	14.37 (6.90)	19.60 (9.16)	9.39 (39.12)
	τ [ps]	1 – 10	5.39 (18.89)	8.29 (8.42)	7.35 (10.41)	5.2 (44.26)
	$1-\alpha$	(fix)	1.0	1.0	1.0	1.0
P2:	$\Delta\varepsilon$	1 – 1000	43.63 (3.97)	63.47 (5.88)	30.49 (8.95)	462.0 (19.25)
	τ [s]	1e-10 – 1e-7 (8e-5)*	3.93e-9 (5.70)	5.94e-8 (14.98)	3.60e-8 (25.07)	5.3e-5 (38.48)
	$1-\alpha$	0.5 – 1	0.72 (1.06)	0.56 (1.51)	0.55 (2.92)	0.5 (0.75)
P3:	m	0 – 0.8	0.2565 (10.48)	0.2567 (3.41)	0.1609 (2.84)	0.1224 (4.91)
	τ [s]	8e-9 – 1e0	1.01e-8 (51.12)	1.57e-6 (14.17)	2.52e-7 (19.69)	1.51e-3 (6.60)
	c	0 – 0.65	0.39 (2.29)	0.48 (1.63)	0.26 (0.64)	0.28 (4.23)
P4:	m	0 – 0.6	0.0049 (5.68)	0.0293 (10.09)	-	0.0749 (5.86)
	τ [s]	1e-3 – 3e2	0.007 (8.74)	1.171 (21.25)	-	5.234 (2.83)
	c	0 – 0.75	0.51 (1.71)	0.20 (9.83)	-	0.44 (2.60)
	σ_{dc} [S/m]	1e-9 – 10	0.0723 (0.16)	0.0090 (0.22)	0.0195 (0.20)	0.0096 (0.09)
	rRMS [%]		2.04	4.57	4.45	24.68
	χ^2		0.94	1.49	1.67	1.41

pure water) can be attributed to single water molecule relaxations, as suggested by Wagner et al. (2013) for unsaturated clay rock or anisotropy in the dielectric spectrum of hydration water suggested by Gekle and Netz (2012). We assign the P2 process to a combination of the bound or hydrated water relaxation and a HF counterion diffusion relaxation that is controlled by the adsorption/desorption rates of counterions at the clay surface (Rotenberg et al., 2005). The LF processes P3 and P4 are most probably attributed to a broad distribution of Maxwell-Wagner type interfacial relaxation effects and LF counterion diffusion relaxations in the electrical double layer (EDL). We do not expect dominant macro-scale relaxation effects that are controlled by the texture and pore geometry of the host medium, since the loess is a very fine grained and poorly sorted material (see Fig. 5.2).

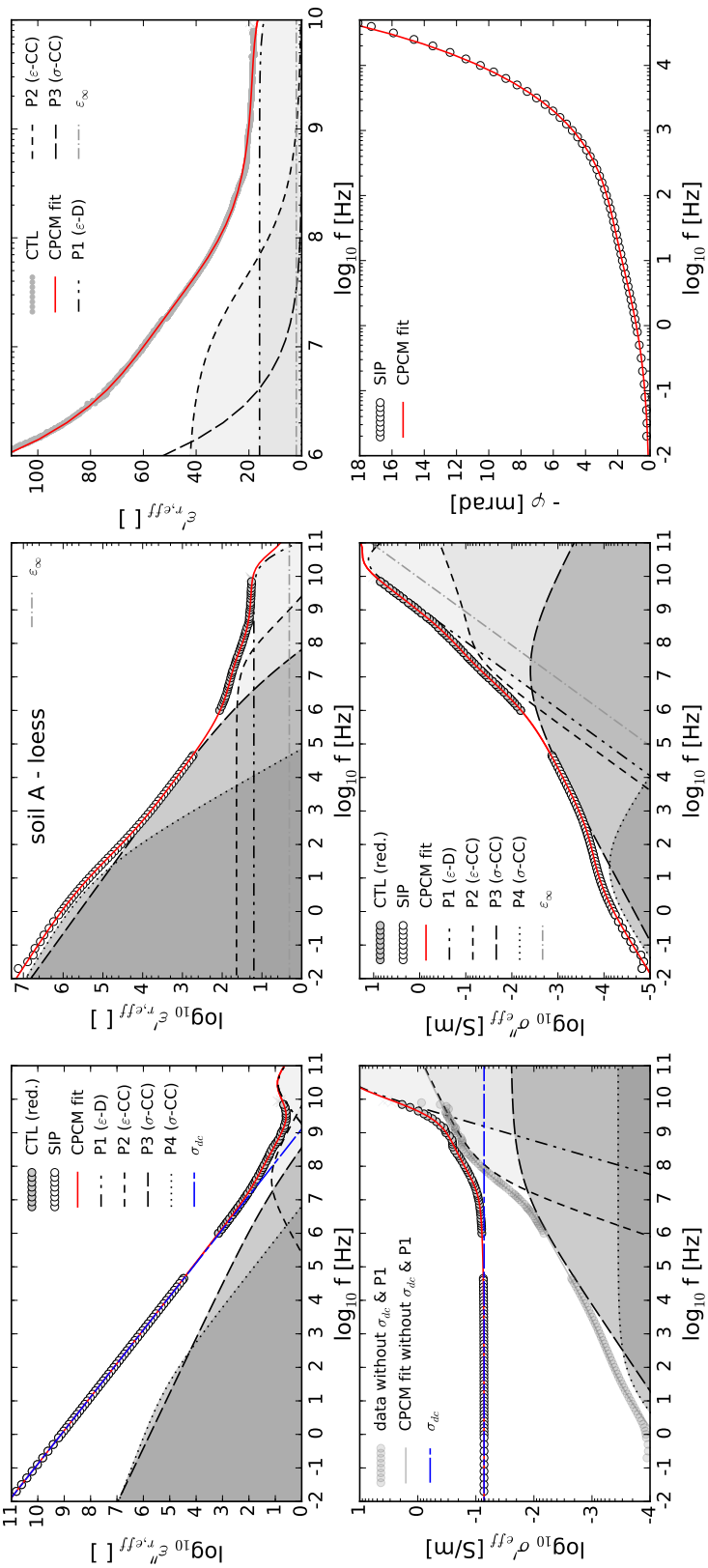

Fig. 5.6.: Soil A - loess. SIP and CTL data of measured and calculated complex effective dielectric permittivity and effective electrical conductivity, as well as resistivity phase φ. The data had been fitted using the CPCM (black line) consisting of 1 ε-Debye-, 1 ε-Cole-Cole-, and 2 σ-Cole-Cole relaxation processes (grey areas) and a dc-conductivity term.

5.4.2. Soil B (laterite)

Fig. 5.7 shows the data and inversion results of soil B (laterite). Just like the loess, the laterite can be fitted using $K = 2$ and $N = 2$ relaxation terms. In contrast however, the relaxation time of the free water relaxation process P1 ($\tau = 8.3$ ps) is in better agreement with the literature value for the relaxation time of pure water at room temperature (8.7 ps). Process P2 occurs at a lower relaxation frequency (2.7 MHz) and its shape is broader in comparison to the loess (1 - α = 0.56 instead of 0.72). This can be attributed to the lower CEC (Tab. 5.1) and therefore, a different adsorption/desorption rate of counter-ions and a smaller amount of bound water. The shape of process P3 is much steeper (c = 0.48) and taking place at much lower relaxation frequencies (100 kHz) in comparison with the loess, with c = 0.39 and f_{P3} = 15.8 MHz. In analogy to the loess, we also assign process P3 to a combination of the Maxwell-Wagner type relaxation (however less pronounced than in the loess) and the relaxation in the EDL. A striking difference to the loess is the shape and relaxation frequency of process P4 at the lower end of the spectrum. The phase at LF reaches a plateau around 2 mrad. Furthermore, the real part of the effective dielectric permittivity seems to depend only on frequency below 1 Hz with a slope of approx. 45°. The shape factor c of the process is very small (c = 0.2) indicating a broad distributed coupled process or a superposition of physically different processes. This observation can possibly be explained by the high amount of ferrimagnetic minerals in this soil and the resulting very high magnetic susceptibility and magnetic frequency-dependence compared to most other soils and rocks (Schön, 2015, p.426). The effect of magnetic susceptibility (permeability) is commonly neglected when interpreting high and low frequency polarisation data. However, Olhoeft and Strangway (1973) show that eddy current losses can be important in the study of the EM response of rocks with considerable amount of magnetic minerals. In contrast, Hubbard et al. (2014) give a another explanation for the LF phase responses they found in materials with semiconductive minerals like magnetite. They conclude that the dispersive response in the Hz frequency region is generated by the adsorption of redox-active ions such as Fe^{2+} to the surface of the semiconductive minerals. Hereby, the adsorption rate in the presence of redox-active ions is sensitive to the pH value. Nevertheless, the strength of this process is magnitudes smaller in our investigated sample in comparison to the data shown in Hubbard et al. (2014).

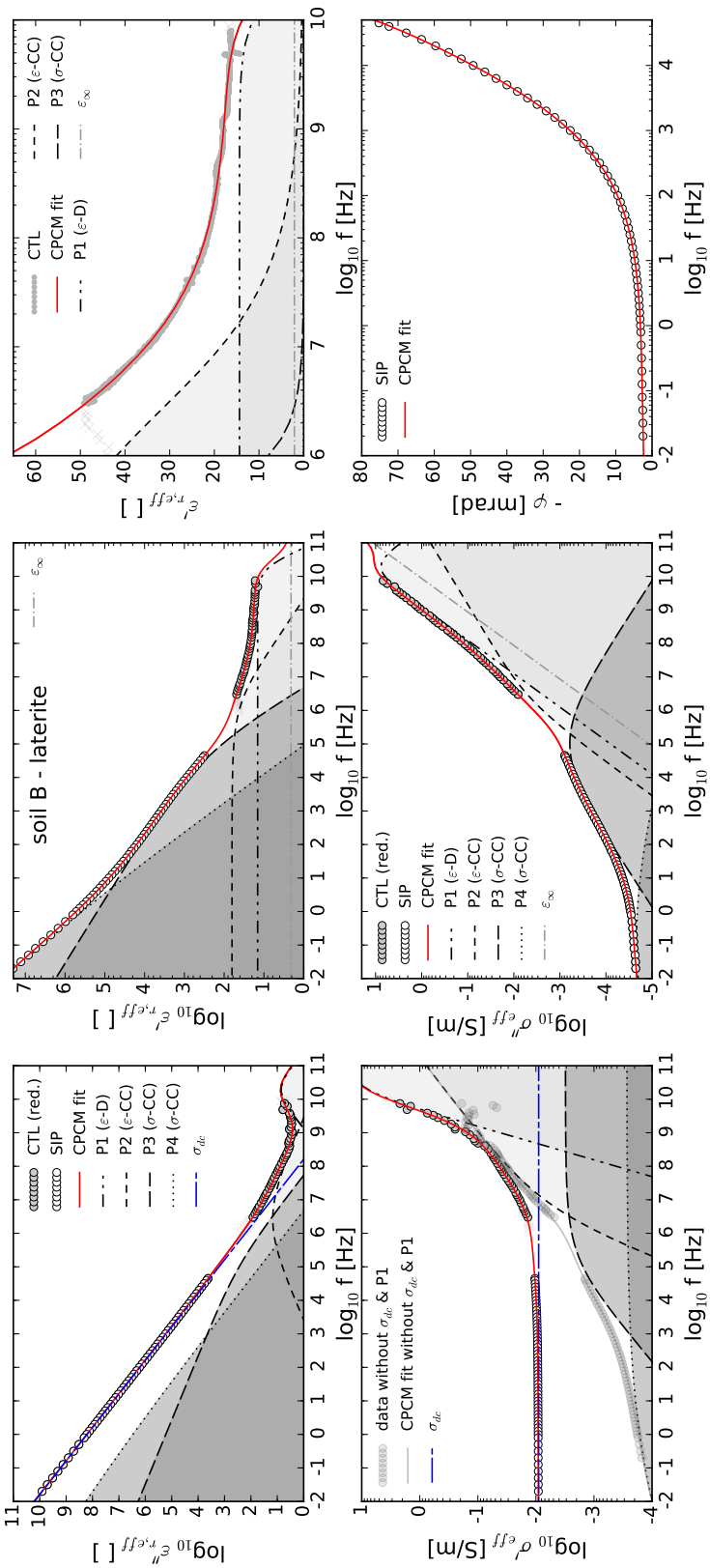

Fig. 5.7.: Soil B - laterite. SIP and CTL data of measured and calculated complex effective dielectric permittivity and effective electrical conductivity, as well as resistivity phase φ. The data had been fitted using the CPCM (black line) consisting of 1 ε-Debye-, 1 ε-Cole-Cole-, and 2 σ-Cole-Cole relaxation processes (grey areas) and a dc-conductivity term.

5.4.3. Soil C (humus)

Fig. 5.8 shows the data and inversion results of soil C (humus). In contrast to all other samples, the data can be fitted by just 3 relaxation models: one ε-Debye (P1) and one ε-CC model (P2) for the HF and one σ-CC model (P3) for the LF range. The loss processes of the humus are clearly dominated by the dc-electrical conductivity up to approximately 100 MHz, and at HF by the relaxation of the free water molecules (P1) at around 1 GHz and above. However, between 100 MHz and 1 GHz, the losses are dominated by the dielectric relaxation process P2. The humus has the highest sand (70%) and the smallest clay content (8%) and a very low CEC (0.5 meq/100g) in comparison to the other soils. Thus, the relaxation strength of the P2 process is much smaller, which we attribute to the smaller amount of bound water and the reduced adsorption/desorption rate. Furthermore, process P3 of the humus has a smaller chargeability of 0.16 and a broader distribution of relaxation times (c = 0.26) in comparison to the loess (with m = 0.26, c = 0.39) and the laterite (with m = 0.26, c = 0.48). The broad relaxation is probably a combination of different effects from the micro-scale to the lower macro-scale: at the one hand, a distribution of small texture-based relaxation effects in the SIP frequency range that are influenced by pore and pore throat sizes due to the increased sand fraction. On the other hand, the broad relaxation distribution of process P3 is due to the Maxwell-Wagner effect in the MHz region together with a broad counterion diffusion relaxation at kHz frequencies.

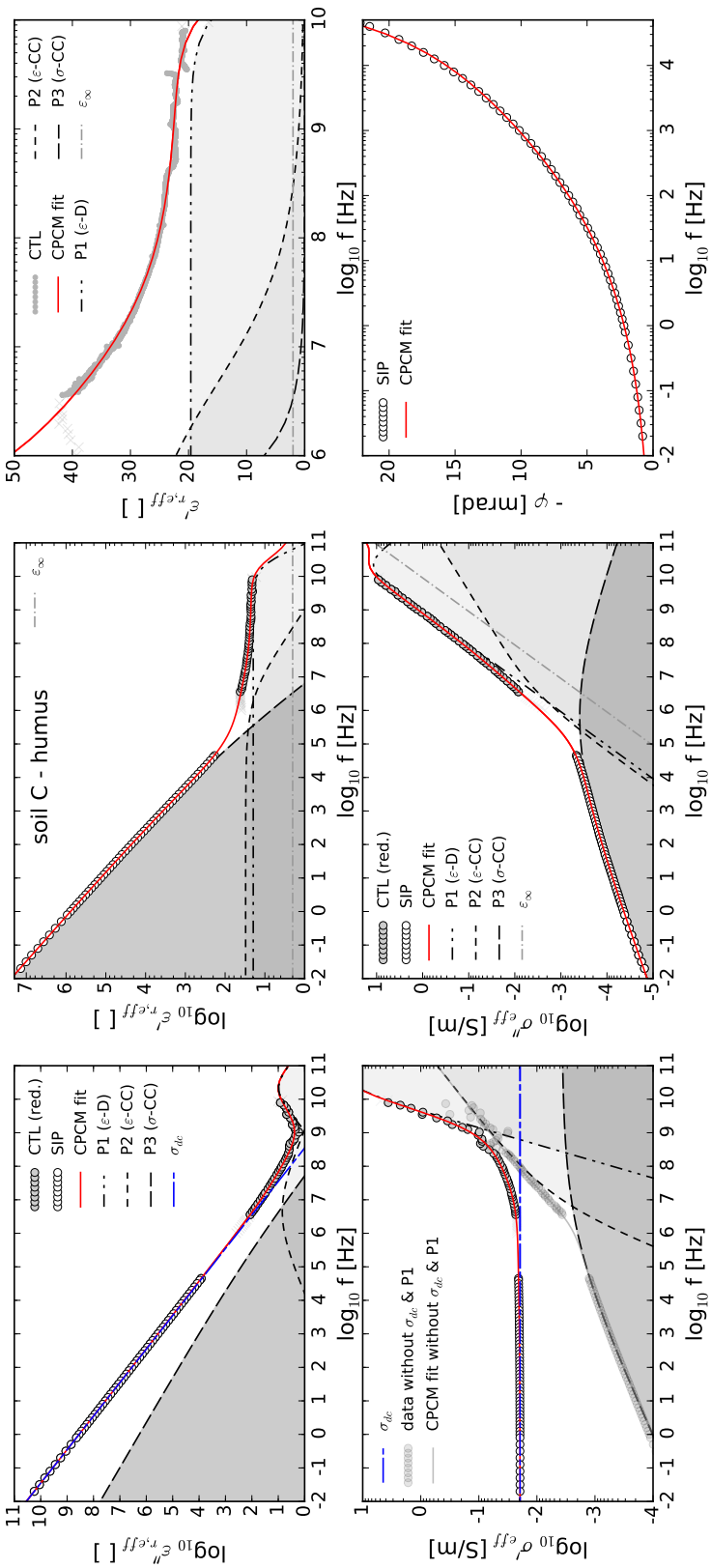

Fig. 5.8.: Soil C - humus. SIP and CTL data of measured and calculated complex effective dielectric permittivity and effective electrical conductivity, as well as resistivity phase φ. The data had been fitted using the CPCM (black line) consisting of 1 ε-Debye-, 1 ε-Cole-Cole-, and 1 σ-Cole-Cole relaxation processes (grey areas) and a dc-conductivity term.

5.4.4. OBS sandstone

Fig. 5.9 shows data and inversion result of the sandstone measurements with the properties described in Tab. 5.2. The sandstone spectra can be fitted by a model consisting of four relaxation processes. The relaxation frequency of the free water relaxation (P1) was poorly resolved, with a relative standard deviation of 44%. The relative RMS error is quite high (25%) in comparison to the soils. This is probably due to the relatively coarse pores of the rock sample and the small gap between the sample and the conductors of the coaxial cell. These gaps can cause scattering in the cell at microwave frequencies, which goes on the expense of the data quality. In contrast to the soils, the relaxation time of P2 is much longer (τ=5.3e^{-5} s, Tab. 5.3) and the inversion boundary had to be shifted down by two decades to accurately fit the data. The relaxation process is very broad (1 - α = 0.5) and basically spans across the micro-scale (Fig. 5.1). In contrast to the soils, we therefore attribute process P2 to the Maxwell-Wagner effect in the sense it was described in Knight and Nur (1987): In a saturated sandstone sample, the grain surfaces are completely coated with a conducting water film. In the electric field the free charges accumulate at either side of the grains and build up a network of water-grain capacitors. The polarization and relaxation strength of each capacitor sum up together and contribute to the overall response. In contrast to the soils, the phase spectrum and the quadrature effective conductivity show typical LF relaxation peaks (P3 and P4). The LF relaxation times of porous media like sandstone generally show strong correlations to the modal pore-throat diameter (Kruschwitz et al., 2010; Titov et al., 2010). As shown in Kruschwitz et al. (2016), the OBS sandstone belongs to media with one dominant pore throat size, but with two SIP relaxation times ('type 2'). The type 2 samples typically only show correlations for the higher-frequency relaxation (P3 in this study, with f = 105 Hz) between the relaxation-time and the modal pore throat diameter. However, the very low-frequency peak (P4, with f = 0.03 Hz) cannot be explained by this relationship alone, since similar relaxation times had been observed in sandstones with large variations of their dominant pore throat sizes (Kruschwitz et al., 2016). An explanation for this observation was attributed to the critical length scale along which relaxation occurs. The very low-frequency relaxation might either be controlled by the length of the narrow pores or the length of the wide pores, depending on their individual sizes. Even so, the relaxation time of P4 is close to the laterit, we can rule out the influence of magnetic minerals in the ferritic cement, since the magnetic susceptibility of the sandstone is very low.

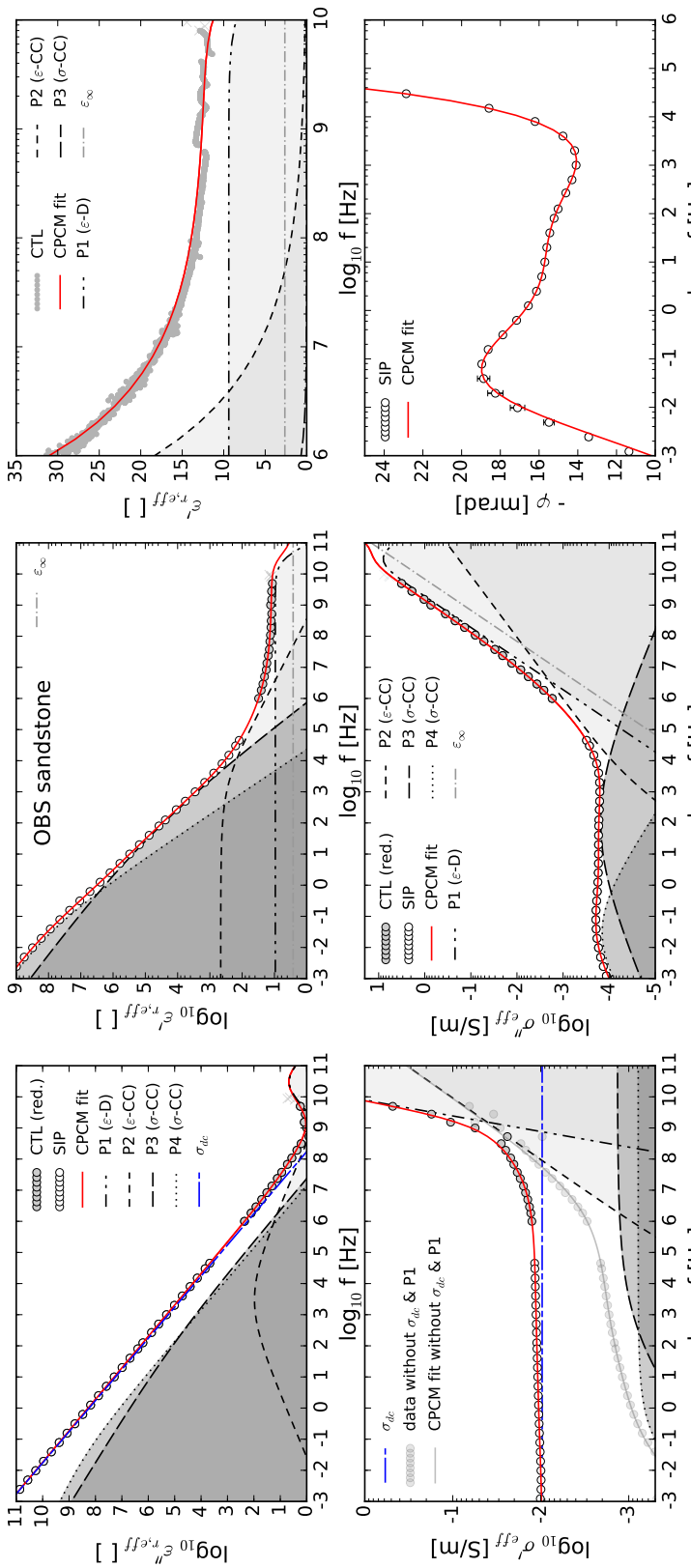

Fig. 5.9.: Sandstone OBS. SIP and CTL data of measured and calculated complex effective dielectric permittivity and effective electrical conductivity, as well as resistivity phase φ. The data had been fitted using the CPCM (black line) consisting of 1 ε-Debye-, 1 ε-Cole-Cole-, and 2 σ-Cole-Cole relaxation processes (grey areas) and a dc-conductivity term.

5.4.5. General discussion

The decomposition results (Figs. 5.6 to 5.9) show that the relaxation processes P2 and P3 overlap in the transition range between LF and HF (cf. Fig. 5.1). Thus, both processes contribute to the overall response of that frequency region. The data without σ_{dc}, P1 and ε_∞ (semitransparent circles and line) in the real part of the effective conductivity together with the decomposition result in the quadrature effective conductivity strongly support the CPCM. Considering SIP measuring setups that measure up to a frequency of 10 kHz, free water relaxation (P1) and ε_∞ does not affect the electrical response. For soils or rather fine-grained and clayey material the strong rise of the phase or quadrature effective conductivity is caused by the relaxation P3 (σ-CC model) that spans over several decades and that is assigned to the counterion relaxation in the EDL and to a distribution of interfacial relaxations of the Maxwell-Wagner type. For consolidated moist porous materials like sandstone, the strong rise above 1 kHz is caused by process P2 (ε-CC model, upper kHz range) that we assigned to the Maxwell-Wagner effect and furthermore, by the broad membrane relaxation (σ-CC model, process P3, lower kHz range). The latter effect can give an explanation for the high response values that were found in saturated sandstone shown in Kremer et al. (2016), which could not be attributed to the Maxwell-Wagner effect alone. In the HF range, interfacial relaxation processes are broadly distributed and span down to the LF range. The slowest observed process in the LF range (P4) has a minor or no contribution to the HF response.

5.5. Conclusions

The combined phenomenological model description based on permittivity and conductivity terms accounting for the ultra-broadband signature of the data, can open a new perspective of the observed relaxation phenomena. In an equivalent circuit, CC models are described by a serial and parallel arrangement of capacitors and resistors of a constant phase or fractional element. However, the arrangements differ between σ-CC models and ε-CC models (Tarasov and Titov, 2013). Our inverse modelling analysis suggest the application of one or two conductivity relaxation models at LF and two dielectric relaxation models at HF. Moreover, the decomposition approach reveals a transition range between LF and HF ranges with a strong overlap of the observed relaxation phenomena of different origin. Hence, parametrization approaches to obtain the time constants and strengths will strongly depend on the chosen decomposition model and the considered frequency range, as recently demonstrated by Weigand and Kemna (2016) for the SIP frequency range. We hope to induce with the ultra-broadband study a physical basis for the development of a general nomenclature for a better systematic analysis and understanding of the relaxation phenomena taking place beyond the frequency range of each individual method. The presented model can be applied sepa-

rately or combined for the two methods and due to its flexibility it can cover different kind of materials at different thermodynamic states with respect to their dominating relaxation characteristics. For instance, one can take care of the electrode polarization occurring in materials with conductive minerals by adding another σ-CC model at the appropriate LF range. Similarly, the ice relaxation at LF can be taken into account as shown by Stillman et al. (2010) for ice-silicate mixtures. There is a considerable amount of published data with systematic investigations that separately cover either the LF or the HF side of the spectrum. All data can be converted into their equivalent expression by assuming effective parameters. Thus, examining data beyond the scope of the commonly used individual frequency range will improve data assessment and interpretation. In future studies, systematic ultra-broadband investigations of moist soils and sediments considering temperature as well as mechanical and hydraulic state together with the demonstrated parameterization approach can help to identify and uncover underlying physical processes.

6. FDTD simulation of GPR in lossy and dispersive soils

This chapter was originally submitted to *Geophysics* on July 11, 2017 under the following title:

Loewer, M. & Igel (2017): Multi-Pole Debye Description of Lossy and Dispersive Media for realistic FDTD Simulation of GPR, Geophysics, submitted.

Abstract

Simulation of electromagnetic wave propagation in lossy and dispersive media requires a realistic description of the electrical and dielectric material parameters. We measured the complex dielectric permittivity of 5 soils with varying clay and silt content in the GPR frequency range using the coaxial transmission line technique. We fitted single and multi-pole Debye permittivity models and a constant dc-conductivity term to the data. FDTD simulations at 100 MHz and 1 GHz center frequencies were carried out on the basis of the different Debye pole media descriptions and compared to simulations with constant electromagnetic parameters. For sandy soils, constant parameters can be used for low GPR frequencies or one Debye relaxation for free water at high frequencies. However, for fine-grained soils like sandy loam or silty clay, 3 Debye relaxations are required for an adequate data fit. We show that for soils with a fine-grained texture, the frequency-dependence of the real part of the dielectric permittivity cannot be neglected. Therefore a multi-pole Debye description of the medium must be used for simulations: one Debye pole describing the relaxation of free water in the lower GHz region and two poles describing the bound water and interfacial relaxations in the upper MHz region.

6.1. Introduction

Ground-penetrating radar (GPR) is an electromagnetic (EM) subsurface sensing technique that enables to record reflected signals from interfaces with different electrical properties. The method has been successfully used for mapping structures and natural or artificial features in varied fields like archaeological prospection (e.g. Conyers,

2013; Neubauer et al., 2014), landmine detection (e.g. Sato et al., 2007; Giannakis et al., 2015), road and building inspection (e.g. Hugenschmidt and Kalogeropoulos, 2009; Benedetto et al., 2012) or for geological interpretations (e.g. Bristow and Jol, 2003; Nielsen et al., 2009). It furthermore has been used to investigate hydrocarbon spills (Cassidy, 2008; Bradford et al., 2010) and for measuring and monitoring the soil water content (Huisman et al., 2003; Allroggen and Tronicke, 2016). Since some years, GPR has also been used as a crosshole tomographic instrument for high-resolution mapping using ray-based reconstruction techniques or the advanced full-waveform inversion scheme (e.g. Meles et al., 2012; Klotzsche et al., 2013). Furthermore, an increasing amount of studies carry out simulations of the radar wave propagation prior or supplementary to a GPR survey (Cassidy, 2007). Most of them use finite-difference time-domain (FDTD) schemes to solve Maxwell's equations. However, in both the forward and the inverse problem the set of electrical and dielectric parameters in the model that are a priori known or which need to be iteratively determined, are predominately assumed to be frequency-independent (e.g. Oğuz and Gürel, 2002; Ernst et al., 2007; Busch et al., 2012, 2014; Gueting et al., 2015). Some study supposed to show prove for the real dielectric permittivity to be frequency-independent in the lower GHz-frequency range and at different water contents (Lambot et al., 2005). However, they limited their investigated material to sand, which often serves as the reference medium for GPR in laboratory studies. Most natural GPR field cites however, differ from sands and contain silt and clay minerals that can negatively affect the GPR performance (Doolittle et al., 2007). In a previous study it was shown that proper field measurements of the dc-electrical conductivity using resistivity or induction methods can strongly underestimate the effective conductivity, since losses due to the dielectric relaxations that occur at high GPR frequencies (HF) are neglected (Loewer et al., 2016b). Furthermore, at low GPR frequencies (LF) velocity dispersion shows distinct effects on the wavelet shape with increasing dc-conductivity. Other studies at LF that focus on lossy ground conditions get along with a single dielectric relaxation function, mostly of the Debye or Cole-Cole type (Annan, 1996).

Whereas the strength of the relaxation phenomenon above 1 GHz is usually linked to the relaxation of free water molecules, dielectric relaxation phenomena in the 10 MHz and above the 100 MHz region are generally related to interfacial relaxation effects as for instance the Maxwell-Wagner effect and the bound-water relaxation (Arcone and Boinett, 2012; Loewer et al., 2017). Thus, these LF relaxation phenomena could for example be indirectly linked to the composition of a moist porous material like soil. Following this theory, some afford has been made in the past, in order to derive clay and water content from GPR measurements using different processing techniques, as for instance shown by Wunderlich and Rabbel (2013) or Tosti et al. (2013). In these studies, correlations between an increased clay content of the soil and systematic changes of the waveform and the frequency spectrum thereof could be observed. With our study, we provide a link between these observations and dielectric spectroscopy measurements of different soils with varying texture. We want to address simplified

assumptions for the EM parameters in FDTD simulations and compare it with the case, where the frequency-dependence of the soil properties had accurately been measured and taken into account.

6.1.1. Incorporating dielectric relaxations in simulations

There are different approaches that enable to incorporate dielectric relaxation functions, for example of the Lorentz- or Debye-type into FDTD schemes. The most common are the recursive convolution (RC; Luebbers et al., 1991) and the auxiliary differential equation (ADE; Kashiwa and Fukai, 1990) or its modification by Young (1995). Teixeira et al. (1998) introduced multi-term Lorentz- and/or Debye models into the FDTD scheme using the piecewise-linear recursive convolution technique. By way of example he fitted two-pole Debye models to reported experimental data. However, both volumetric water content (10 %) and the conductivities of the model (0.4 to 2 mS/m for clay loams) had been very low in comparison to our analyzed materials. In contrast Bergmann et al. (1998) introduced a multi-term Debye- or Zener model and Kelvin-Voigt type model with a static conductivity, witch had been applied in FDTD simulations (Cassidy, 2001, 2008). Cassidy (2001) found that less than five relaxation mechanisms would be used to fit the measured dielectric spectra, but even two can provide a reasonable fit across the GPR frequency range. In contrast, we demonstrate that relatively small variations in the fit of the dielectric spectra can cause big differences in the simulation result. Other studies demonstrated that lossy and dispersive media can show a strong frequency-shift as well as wavelet dispersion, especially in soils with increased water and clay content (e.g. Irving and Knight, 2003; Bradford, 2007). Investigations on the nature of that behavior reveal different dielectric relaxation phenomena that are responsible for the frequency-dependent signature of the electrical media parameters.

6.1.2. Electrical loss and dispersion in field data

The influence of losses due to EM absorption is demonstrated in Fig. 6.1. The radargrams show GPR measurements of 2 soils, in which two metal plates with the dimension of 50 cm x 50 cm had been buried in 40 cm and 20 cm depth. The measurements were carried out using a ground-coupled 900 MHz antenna system. The soils strongly vary in texture and have different water contents, but exhibit only minor differences between their mean dc-electrical resistivities (sandy loam: 120 Ωm and clay: 77 Ωm), which were measured using geoelectrics.

However, strong variation can be observed by comparing the amplitude decay from the metal plate reflections at 20 cm and 40 cm depths in the two radargrams (dashed areas in Fig. 6.1). The clay attenuates the EM waves stronger than the sandy loam and the reflection from the deeper plate in the clay occurs at later travel times and looks more diffuse in comparison to the sandy loam. On the right hand side of Fig. 6.1 are the

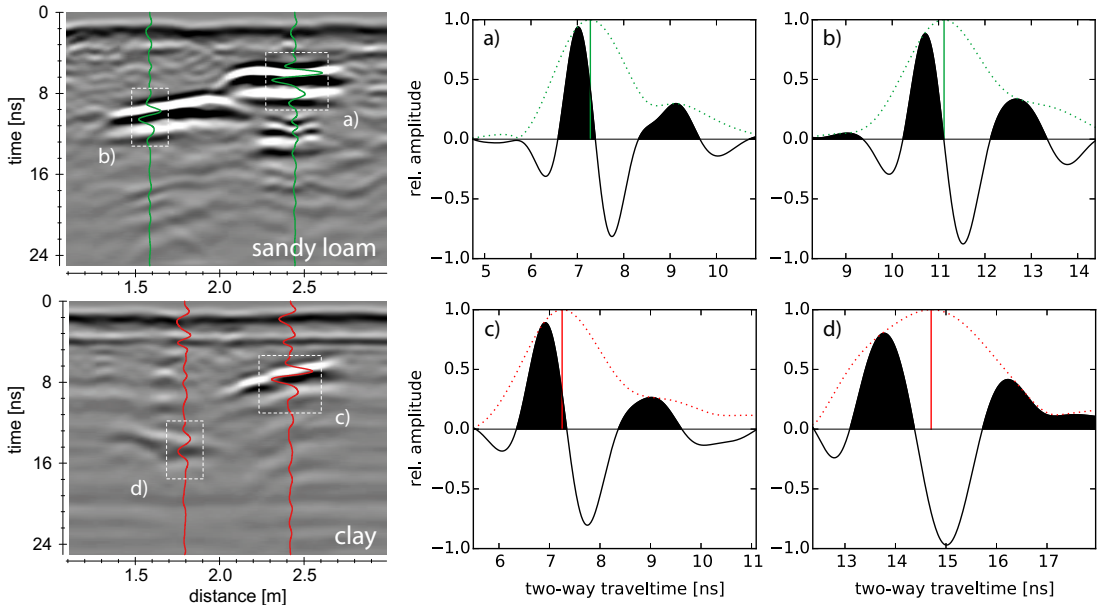

Fig. 6.1.: 900 MHz radar profiles and extracted wavelets with 2 metal plates burried at 20 cm and 40 cm depth (left). The sandy loam and the clay vary in texture and water content (see Tab. 6.1). Data processing complied of static shift, divergence compensation, bandpass filter and amplitude normalization. Attenuation (in dB/m) and wavelet elongation (we) was calculated using the wavelet envelopes (green, red) of the non-normalized amplitudes. The vertical colored line denotes the point where most energy of the wavelet is concentrated.

normalized traces of the reflected wave from the metal plates (a, b & c, d) that had been extracted from each radargram. We calculated the envelopes of the time traces (red and green lines) using the Hilbert transform in order to measure the combined maximum peak and trought amplitudes. Furthermore, we calculated an elongation factor as one measure of the wavelet dispersion using the half-width of the envelope (more details can be found in chapter 'Simulations'). The attenuation rate, which had been determined by comparing the maximum envelope amplitudes of the non-normalized traces is two times higher in the clay ($\alpha = 62$ dB/m) compared to the sandy loam ($\alpha = 33$ dB/m). Furthermore, the wavelet elongation factor (we) suggests that the wavelet had been stretched by 70% (we = 1.7) while propagating a distance of 20 cm (compare Fig. 6.1c and 6.1d) in the clay, whereas in the sandy loam wavelet elongation is only 20% (we = 1.2; compare Fig. 6.1a and 6.1b). Even so, dispersion and attenuation is much higher in the clay then in the sandy loam, the small differences in electrical resistivity cannot be responsibly for the reduced GPR performance alone. Thus, frequency-dependent dielectric relaxation effects in moist soil must be considered as well.

6.2. Materials and Methods

6.2.1. Soil materials

The soils investigated in this study cover a broad range of soil types with varying texture (Fig. 6.2). We arranged the five soil samples with regard to their texture class. Apart from water content (which is similarly for our samples) texture is the second most important parameter, which controls the frequency-dependence of the dielectric spectrum in the radio to microwave frequency range (see for instance the semi-empirical dielectric mixing models by Dobson et al. (1985); Hallikainen et al. (1985); Peplinski et al. (1995); Mironov et al. (2008), which require clay and silt content as input parameters). The physico-chemical properties of the soils are given in Tab. 6.1.

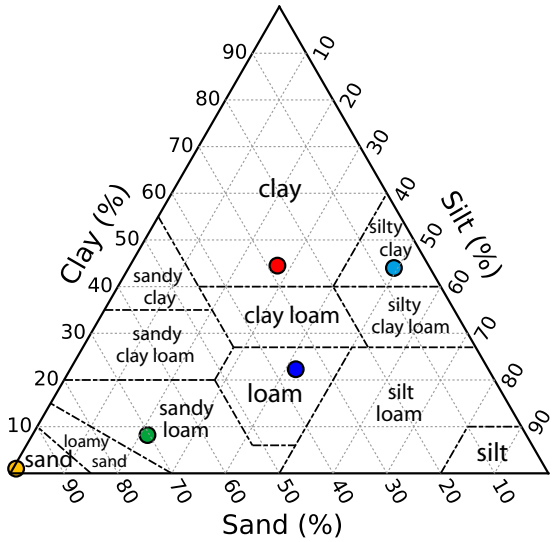

Fig. 6.2.: Soil texture triangle defined after USDA (1987) with the five investigated soils as in Tab. 6.1.

- The sand is pure quartz from the North Sea Island Borkum with 95 % content of fine to medium well-sorted dune sand. The sample has a porosity of 31 % and was saturated with tap water. The cation exchange capacity (CEC) and the total carbon content are negligibly small.

- The sandy loam is a humus soil sample from the SE Bavarian border and predominately consists of poorly sorted sand and 30% of silt and clay from silicatic, calcitic or carbonatic origin. The CEC of the humus is very small and its total carbon content is typically increased with C_{tot} = 5.4 %.

- The clay sample is part of a tropical laterite soil, which typically underwent strong weathering. The major and minor mineral components of the clay sample are quartz, gibbsite and also hematite, which gives the laterite its typical red

Tab. 6.1.: Physical and chemical properties of the five soils. The texture class is due to USDA (1987). The cation exchange capacity (CEC) was measured using the Cutriene method (Cu2+/CEC). The porosity ϕ was calculated assuming a particle density of 2.65 g cm^{-3}.

texture class	sand	sandy loam	clay	loam	silty clay
clay [%]	0.5	8.2	44.5	22.3	44.0
silt [%]	4.2	21.5	27.4	41.9	49.4
sand [%]	95.3	70.4	28.1	35.8	6.7
θ_v [%]	32.68	36.82	30.29	34.98	35.82
ρ_b [g cm^{-3}]	1.58	1.58	1.38	1.49	1.68
ϕ [%]	40.37	40.38	47.92	43.77	36.60
CEC [meq/100g]	0.3	0.5	5.2	7.7	18.5
C_{tot} [%]	0.06	5.41	0.38	0.18	0.26
pH (H_2O)	6.45	9.19	7.59	6.47	7.97

color. Obviously, the clay has the highest clay content among the samples, however the CEC is relatively low. This is due to the nature of the clay minerals, which are predominantly kaolinite and gyppsite with typically lower CECs.

- The loam sample shows the most balanced composition of clay, silt and sand fractions. Its major and minor mineral components are quartz, feldspar, muscovite-illite and chlorite. In comparison to the clay sample the fractions of clay and silt are switched. The CEC is slightly higher for the loam than for the clay.

- The last sample is silty clay, which belongs to a loess soil and whose major mineral component is quartz. The silty clay sample has the highest cation exchange capacity (CEC) of the analysed soils, which is due to the swellable layer silicates (vermiculite and smectite group). The silty clay sample has the smallest sand fraction of all analyzed soils and its clay and silt fractions are poorly sorted (see also Loewer et al., 2017).

The volumetric water content of the five soil samples varied between 37% and 48% and had been calculated together with the bulk densities ρ_b (in g cm^{-3}) after the spectroscopy measurement of the samples using oven drying at a temperature of 105 °C for 24 hours.

6.2.2. Dielectric permittivity measurements

All soils were initially measured at different volumetric water contents θ_v from dry to saturated. However, due to the complexity of the simulation study we concentrate on differences due to texture and show datasets with similar (high) water content. Thus, with respect to the measured dielectric spectra, our datasets exhibit similar values of high-frequency (HF) real permittivity ($\varepsilon'_{r,eff} \approx 20$) between 18 and 20, but span a certain distribution of polarization at low-frequencies (LF) in the real part and losses in the imaginary part of the dielectric permittivity (see Fig. 6.3).

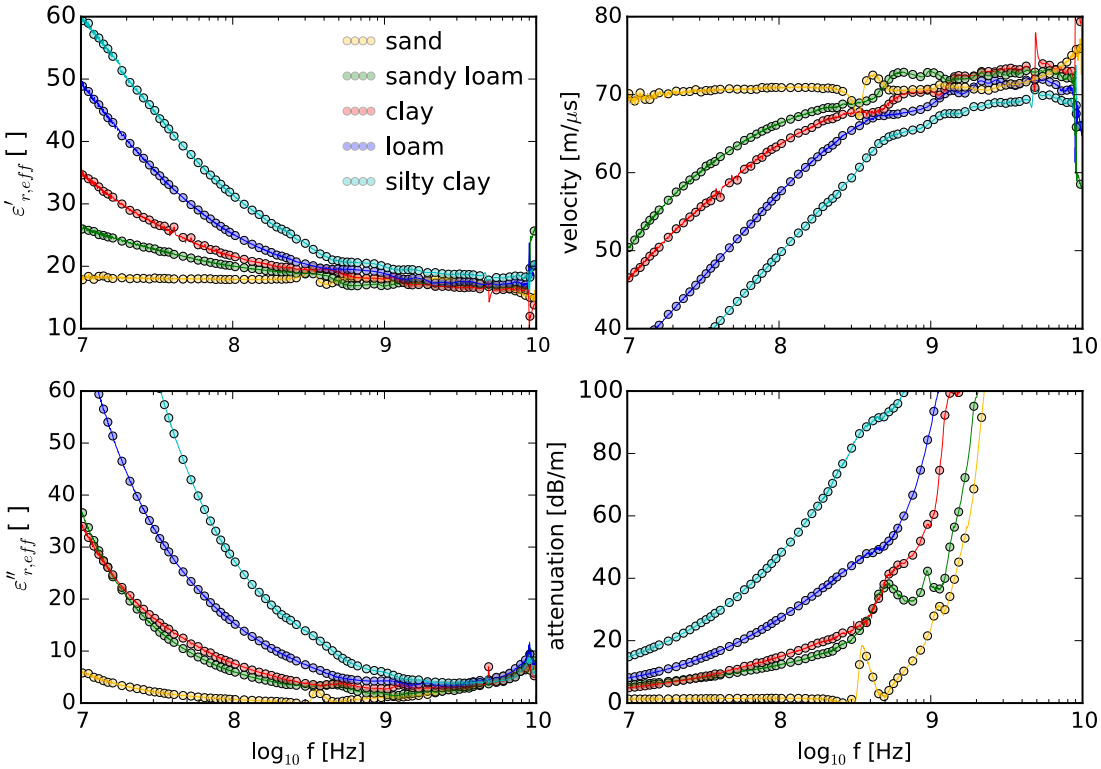

Fig. 6.3.: Real $\varepsilon'_{r,eff}$ and imaginary part $\varepsilon''_{r,eff}$ of the relative effective complex dielectric permittivity of the five soils (Tab. 6.1, Fig. 6.2) measured with the CTL technique. Aside, the calculated intrinsic attenuation (Eq. 6.2) and phase velocity (Eq. 6.3).

The complex dielectric permittivity measurements were carried out in the frequency range between 10 MHz and 10 GHz using a 2-port coaxial transmission line (CTL) together with a R&S ZVL13 vector network analyzer. The coaxial cell in which the soil samples were embedded consists of an outer and inner 50 mm length conductor made from copper with a volume of 42.3 cm^3. Each side of the cell was sealed with teflon disks to prevent leakage of the moist samples into the coaxial cell. In order to assess the data quality, we measured different calibrations standards like teflon, water and alcohols, whose typical relaxation parameters are described in the literature (see Loewer et al., 2017). The CTL technique generally measures the complex reflection and transmission parameters (scattering or S-parameters) of the device under test. We use a combination of the quasi-analytical propagation matrix (PM) method (10-200 MHz; Gorriti and Slob, 2005c) and the fast transmission method (FAST; 200 MHz-10 GHz; Agilent, 2014) in order to derive the complex dielectric permittivity from the scattering parameters. A detailed description of the utilized CTL technique and cell holders can be found in Lauer et al. (2012) and Wagner et al. (2013).
The measured data of the five soil samples are shown in different colors in Fig. 6.3 with their real $\varepsilon'_{r,eff}$ and imaginary part $\varepsilon''_{r,eff}$ of the relative effective complex dielectric

permittivity given as:

$$\varepsilon^*_{r,eff}(\omega) = \varepsilon'_{r,eff} - i\varepsilon''_{r,eff} = \varepsilon'_r - i\left(\varepsilon''_r + \frac{\sigma_{dc}}{\omega\varepsilon_0}\right), \tag{6.1}$$

where ε'_r, ε''_r and ε_0 the real and imaginary relative permittivity and the free space permittivity and σ_{dc} is the dc-conductivity, with ω the angular frequency ($\omega = 2\pi f$, where f is the frequency). We assume that the real electrical conductivity $\sigma'(\omega)$ is constant, which corresponds to σ_{dc} and therefore that the imaginary electrical conductivity $\sigma''(\omega)$ can be neglected in the GPR frequency range (Knight and Endres, 2005). Furthermore, we calculated the intrinsic attenuation [in dB/m]:

$$\alpha(\omega) = \frac{8.686\,\omega}{c_0}\sqrt{\frac{\varepsilon'_{r,eff}}{2}\left(\sqrt{1+\left(\frac{\varepsilon''_{r,eff}}{\varepsilon'_{r,eff}}\right)^2} - 1\right)} \tag{6.2}$$

and the phase velocity [in m/ns]:

$$v(\omega) = c_0\sqrt{\frac{\varepsilon'_{r,eff}}{2}\left(\sqrt{1+\left(\frac{\varepsilon''_{r,eff}}{\varepsilon'_{r,eff}}\right)^2} + 1\right)}^{-1}. \tag{6.3}$$

from the measured data, with the conduction to displacement current ratio $\varepsilon''_{r,eff}/\varepsilon'_{r,eff}$ commonly referred to as the loss tangent ($\tan\delta$). The attenuation spectra of sand and sandy loam (see Fig. 6.3) show some artifacts at around 400 and 500 MHz probably caused by scattering effects in the measuring cell due to sample heterogeneity. These effects were typically seen on dielectric spectra of more coarse grained sandy soils and are probably attributed to small gaps between the grainy substance and the conductors of the CTL.

6.2.3. Dielectric relaxations

Apart from the sand, it can be observed that both $\varepsilon'_{r,eff}$ and $\varepsilon''_{r,eff}$ increases with decreasing frequency (see Fig. 6.3). The increase in $\varepsilon''_{r,eff}$ is controlled by losses due to electrical current flow and dielectric relaxation phenomena. Whereas the increase in the real part at LF is attributed to relaxation phenomena alone. With respect to the texture of the measured soils, the strength of the dielectric relaxation increases with increasing silt and clay fraction. This is due to the interfacial relaxation effects with charges and polar molecules at the solid-liquid interface of the soil. The interfacial and surface area of the soil increases with increasing amount of fine-grained material, which in turn increase the bulk interfacial relaxation effect. Physico-chemical phe-

nomena that belong to the interfacial relaxation effects comprise the Maxwell-Wagner effect (Knight and Nur, 1987), with typical relaxation frequencies between the kHz and MHz range. Furthermore, it includes the relaxation due to physically bound and hydrated water (Ishida et al., 2000), together with the relaxation process referred to as adsorption/desorption rates of counterions in clay interlayers (MHz to GHz range; Rotenberg et al., 2005). In contrast, it is primarily the dipolar orientational relaxation of free and immobile[1] water that controls the real effective dielectric permittivity in the GHz range (Kaatze, 2000). With a relaxation frequency for free water of around 17 GHz (at 20° C) the maximum of that effect however is beyond the investigated frequency range.
The intrinsic attenuation and velocity, as well as the dispersion thereof are strongly influenced by the conduction current to displacements current ratios $(\varepsilon''_{r,eff}/\varepsilon'_{r,eff})$. The velocity generally depends on the water content where frequency-dependence of velocity (velocity dispersion) is predominantly observed below the GHz frequency range and linked to the dc-conductivity and LF interfacial dielectric relaxation effects. In contrast, frequency-dependence of attenuation (attenuation dispersion) is primarily controlled by the free-water dielectric relaxation above the GHz frequency-range. At lower frequencies it is primarily controlled by the dc-conductivity as well as interfacial relaxation effects.

6.2.4. Fitting Debye models

A common approach for describing the measured data using a manageable set of parameters are phenomenological and semi-empirical models in the frequency-domain as the Debye or Cole-Cole (CC) model. Many studies fit one or two CC models to the broandband dieletric data of soil (e.g. Wagner et al., 2011; Lauer et al., 2012; Wagner et al., 2013). In contrast to the Debye model, the CC model comes along with a stretching factor in order to cover a distribution of relaxation times for the broadband interfacial relaxations (Loewer et al., 2017). However, Fourier transformation of the CC model requires complex approximations in the time-domain, which are computational expensive in the FDTD simulation code. Thus, we use a multiple-pole Debye model instead of a single broadband CC model to describe the interfacial relaxations in the MHz range and the free-water relaxation in the GHz range. The Debye model is the most straightforward way to implement the complex dielectric permittivity parameter into a FDTD code in order to solve the Maxwell equations. Examples with multiple-pole Debye relaxations for dispersive media can be found in Xu and McMechan (1997); Bergmann et al. (1998); Teixeira et al. (1998); Carcione and Schoenberg (2000). However, in most of the shown examples and due to a lack of measured dielectric spectroscopy data for soils, many authors make simplified assumption regarding the number of Debye poles, dc-conductivity levels and the relaxation time or

[1]

frequency of the free-water relaxation. Furthermore, the fitting procedure using third-hand laboratory data (e.g. Xu and McMechan, 1997) and the implementation of the relaxation parameters into the FDTD code strongly varies amongst the authors.
We investigated the fit of measured complex dielectric permittivity data of our soil sampels in frequency-domain using a multiple-pole Debye model consisting of either 1, 2 or 3 Debye poles and a dc-conductivity term:

$$\varepsilon^*_{r,eff}(\omega) = \varepsilon_\infty + \sum_{k=1}^{N} \frac{\Delta\varepsilon_k}{1+i\omega\tau_k} - i\frac{\sigma_{dc}}{\omega\varepsilon_0}, \tag{6.4}$$

with $\Delta\varepsilon_k = \varepsilon_{s,k} - \varepsilon_\infty$, wherein ε_∞ corresponds to the infinite frequency limit of the relative permittivity, $\varepsilon_{s,k}$ and τ_k are the static or low-frequency limit and the relaxation time of the k-th Debye pole and N={1;2;3} is the maximum number of Debye poles. In order to find the best fitting parameters we used a Levenberg-Marquardt inversion scheme provided by the Geophysical Inversion and Modelling Library (GIMLi, Rücker et al., 2016). For each dielectric spectrum of the soils, we fitted five different models with increasing complexity:

1. ε =const. and $\sigma = 0$,
2. ε =const. and $\sigma = \sigma_{HF}$,
3. $\varepsilon^*_{r,eff}(\omega)$ with N=1 (1 Debye) and $\sigma = \sigma_{dc}$,
4. $\varepsilon^*_{r,eff}(\omega)$ with N=2 (2 Debye) and $\sigma = \sigma_{dc}$,
5. $\varepsilon^*_{r,eff}(\omega)$ with N=3 (3 Debye) and $\sigma = \sigma_{dc}$.

We compared the misfit to find the smallest number of parameters that accurately describe the underlying material in the measured frequency range (10 MHz to 10 GHz). Fig. 6.4 shows by way of example for loam the measured real ($\varepsilon'_{r,eff}$) and imaginary parts ($\varepsilon''_{r,eff}$) of the complex effective relative dielectric permittivity with increasing model complexity that had been fitted to the data. The dataset in the first two rows show the fit (blue lines) using constant material parameters for fitting dielectric permittivity ε and electrical conductivity σ. In the first case σ was chosen to be zero ($\sigma = 0$). In the second case a constant σ value was fitted to the downward slope of the imaginary permittivity, which in contrast to the quasi-direct current low-frequency electrical conductivity σ_{dc} we call a high-frequency electrical conductivity ($\sigma = \sigma_{HF}$). The fitted linear slope of $\sigma = \sigma_{HF}$ intersects the measured data approximately at 100 MHz, which by chance corresponds to the center frequency of one of the simulated wavelets. The sub-figures in the 3rd to 5th row introduce Debye models to fit the same data with 1 dielectric relaxation (Dby 1, Fig. 6.4) at 18 GHz (Tab. 6.2) for the free water relaxation and another 0 to 2 Debye relaxations (and a dc-conductivity term σ_{dc})

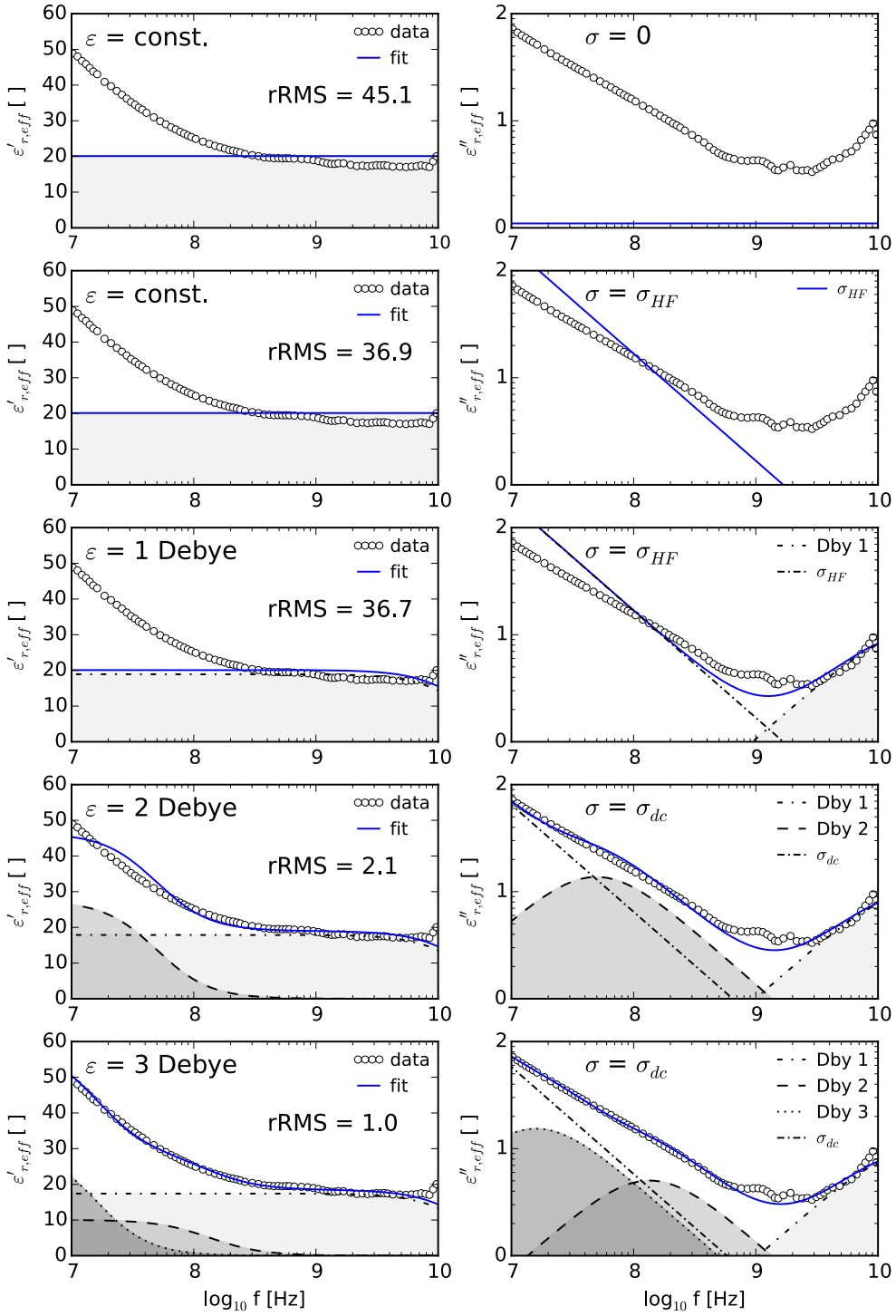

Fig. 6.4.: Real $\varepsilon'_{r,eff}$ and imaginary part $\varepsilon''_{r,eff}$ of the measured relative effective complex dielectric permittivity of loam (Tab. 6.1) fitted with constant material parameters (ε = const.) or multiple-term (1-3 Debye) relaxation models with increasing complexity (overall fit: blue line; Debye models: grey shaded areas).

in order to fit the interfacial relaxation in the MHz frequency range (Dby 2, Dby 3, Fig. 6.4).

The decision of which model accurately describes the data was made on the basis of the relative root mean square error (*rRMS*) of $\varepsilon^*_{r,eff}$ given in percent deviation from the measured data as:

$$rRMS = \sqrt{\frac{1}{n}\sum_{i=1}^{n}\left|\frac{\log(d_i)-\log(p_i)}{\log(p_i)}\right|^2}, \tag{6.5}$$

where n is the number of data points, d_i are the model predictions given by the model and p_i are the measured data. It is apparent from the shown example (Fig. 6.4) that the best fit of the entire spectrum can be achieved with the maximum number of Debye-poles. In case of the loam sample 3 Debye poles gave the smallest rRMS error of 0.9%. The fitting parameters for the five measured soils together with the rRMS error are listed in Tab. 6.2.
The effect the fitted electrical media models with different complexity have on the simulated GPR wave propagation strongly depends on the bandwidth of the source wavelet, which is going to be addressed at a later point. Until this point, our perspective was focused on an accurate description of the dielectric measurements for the entire spectrum using a phenomenological model in frequency-domain.
However in the FDTD code, the Debye equation and its multiple-pole variant is implemented in time-domain and represented in terms of the electrical susceptibility χ. Thus, Eq. 6.4 can be rewritten as:

$$\varepsilon^*_{r,eff}(\omega) = \varepsilon_\infty + \sum_{k=1}^{N}\chi_k(\omega) - i\frac{\sigma_{dc}}{\omega\varepsilon_0}, \tag{6.6}$$

with

$$\chi_k(\omega) = \frac{\Delta\varepsilon_k}{1+i\omega\tau_k} \tag{6.7}$$

and its Fourier transform is found to be

$$\chi_k(t) = \frac{\Delta\varepsilon_k}{\tau_k}e^{-t/\tau_k}U(t) = \frac{\varepsilon_{s,k}-\varepsilon_\infty}{\tau_k}e^{-t/\tau_k}U(t), \tag{6.8}$$

where $U(t)$ is the Heaviside step function (Luebbers et al., 1990; Giannopoulos, 1998). The convolution between the electric field and the time-domain electrical susceptibility χ of the Nth-order dispersive medium is recursively implemented into the FDTD code (Luebbers and Hunsberger, 1992).

Tab. 6.2.: Constant electrical and dielectric parameters and single and multiple-term Debye relaxation parameters (Eq. 6.4) that were calculated by the fitting process and used in the FDTD simulations (Eq. 6.8). The relative root mean square error (rRMS) given in %.

	sand	sandy loam	clay	loam	silty clay
const. para ($\sigma = 0$).					
ε	18.05	18.25	18.86	20.11	21.76
σ_{HF} [S/m]	0.0	0.0	0.0	0.0	0.0
rRMS [%]	4.3	14.5	14.9	20.2	28.1
const. para.					
ε	18.05	18.25	18.86	20.11	21.76
σ_{HF} [S/m]	0.003	0.036	0.046	0.093	0.175
rRMS [%]	2.7	6.3	8.8	8.8	8.5
1 Debye					
$\Delta\varepsilon_1$	18.05	18.25	18.86	20.11	21.76
τ_1 [ps]	8.76	8.65	8.97	8.97	8.21
σ_{HF} [S/m]	0.003	0.036	0.046	0.093	0.175
ε_∞	1.20	2.23	1.53	1.15	3.92
rRMS [%]	0.9	5.8	8.2	8.3	8.1
2 Debye					
$\Delta\varepsilon_1$	18.26	17.70	18.17	18.96	19.83
$\Delta\varepsilon_2$	0.86	7.99	15.09	28.50	37.96
τ_1 [ps]	8.95	7.96	8.98	8.98	7.92
τ_2 [ns]	0.47	1.72	2.76	3.21	2.15
σ_{dc} [S/m]	0.003	0.020	0.017	0.036	0.085
ε_∞	1.22	1.69	1.69	1.05	3.86
rRMS [%]	0.8	1.3	1.9	1.8	1.6
3 Debye					
$\Delta\varepsilon_1$	18.11	17.22	19.00	18.43	19.24
$\Delta\varepsilon_2$	0.84	4.30	5.11	11.07	18.45
$\Delta\varepsilon_3$	1.63	8.81	17.06	31.68	36.72
τ_1 [ps]	8.80	7.28	7.37	8.76	7.15
τ_2 [ps]	377.13	637.66	352.74	1176.8	882.01
τ_3 [ns]	13.17	8.73	7.88	22.3	9.99
σ_{dc} [S/m]	0.003	0.019	0.015	0.032	0.081
ε_∞	1.01	1.00	1.03	1.01	1.00
rRMS [%]	0.8	0.7	0.9	0.9	0.5

6.2.5. FDTD simulations

For the FDTD simulation of the electromagnetic wave propagation in dispersive media we used the open source software gprMax (e.g., Giannopoulos, 2005; Warren et al., 2016). The software solves Maxwell's equations in 3D using the Yee algorithm (Yee, 1966) and it can take different relaxation and dispersion models into account, like the Debye, Lorentz or Drude model using a noval piecewise linear recursive convolution approach (PLRC; Giannakis and Giannopoulos, 2014). Furthermore, it enables to add an arbitrary number of relaxation poles to each individual model. So, we can incorporate accurately fitted model parameters of measured complex dielectric permittivity spectra of any material into the time-domain code. We implemented the single- and multi-pole Debye model parameters for the complex dielectric permittivity and electrical conductivity given in Tab. 6.1 to describe the media for the FDTD simulation.
The model for the simulation consisted of a thin rectangular block where both, transmitter and receiver were placed in a certain distance from each other within the medium. We compared the wavelet at the start position with the wavelet that traveled to a certain distance d from the transmitter inside the dispersive medium and analysed the influence of the chosen media parameters on the wavelet. Our source antenna was a Hertzian dipole and the source signal was a ricker wavelet with a center frequency of either 100 MHz or 1 GHz, which covers the frequency range typically used for most GPR investigations. The source-receiver distance was 2 m for the 100 MHz signal and 1 m for the 1 GHz signal. The model size for the 100 MHz simulation is 2.65 m along the transmitter-receiver axis and 1.3 m perpendicular to it. For the 1 GHz simulation the width of the model was reduced by half (0.65 m). The Yee cell in z-direction is only one cell thick, which means that we carried out 2D simulations. The time increment Δt had to be smaller than the smallest relaxation time τ that in turn binds the spacial discretisation (Giannopoulos, 1998). Furthermore, in order to ensure numerical stability, the time increment is controlled by the Courant-Friedrichs-Lewy (CFL) condition. In gprMax, the time increment is by default calculated from the spacial discretization (see Warren et al., 2016), which in turn had to be small enough, in order to receive time steps shorter than the free water relaxation time (7.9 ps). However, the equality of time discretization with the CFL condition by default can be modified by introducing a time-step stability factor ($0 \leq f_1 \leq 1$), which multiplies to the calculated time step. For the 100 MHz simulations, we chose a spacial discretization of 10 mm in x,y,z -direction and a time-step stability factor ($f1$) of 0.2, which gave a time step of 4.7 ps. In case of the 1 GHz wavelet and wave propagation in moist soil with relative dielectric permittivity as high as 25.6, the wave length becomes as small as 29 mm. Given the rule of thumb that the spacial distretization should be in the order of a tenth of the wavelength (Giannopoulos, 1998), we chose a spacial discretization of 2 mm for the 1 GHz simulations. In analogy to the 100 MHz simulations this gave a time step of 4.7 ps, which is clearly below the relaxation time of water. Perfectly matched layer (PML) absorbing boundary conditions (ABCs) were used, which are based on a

recursive integration approach to the complex frequency shift RIPML (Giannopoulos, 2012). We analyse and compare relatively weak signals that might be disturbed by weak reflections at the model boundaries, however after several tests a number of 10 cells for the ABC proved to be sufficient.
In order to describe wavelet changes and differences with quantitative numbers, we calculated the following values and characteristic properties:

1. the envelope (env), which is the absolute value of the Hilbert-transform of the wavelet,

2. the spectrum of the wavelet calculated by the FFT frequency-spectrum of the wavelet,

3. the center frequency (f_c) that is calculated on the basis of the center point of the half-band width as given in Wang (2015),

4. the wavelet elongation (we), which is the half width of the envelope of the wavelet,

5. the cross-correlation (cc) between two wavelets in order to access their similarities (on the one hand, we use the cc in order to correlate different wavelets with the start wavelet (cc - 0m) and on the other hand, we correlate the wavelets of different models of a soil with the wavelet corresponding to the most complex model for the soil with 3 Debye relaxations (cc - 3Dby)),

6. the wavelet attenuation (α), which was calculated by the logarithm of the maximum envelope amplitude ratios of the propagated wavelet to the wavelet at the start and

7. the travel time (t) at which most wavelet energy is concentrated (envelope maximum) after 2 m (100 MHz) or 1 m (1 GHz) distance.

6.3. Results & Discussion

The results of the FDTD simulation for the 100 MHz and 1 GHz wavelets are shown together with the attenuation and the velocity of the measured permittivity data and the different models that were fitted to the data in a 6x6 sub-figure matrix (Fig. 6.5-6.9). Sub-figure columns 3 and 4 show attenuation (α) and velocity (v) spectra of the soil, which had been calculated on the basis of the measured dielectric spectroscopy data. The fitting result of a certain media model to the dielectric permittivity data can be observed in the attenuation and velocity spectra. The decomposition of the fitted media model into individual processes is shown in the attenuation spectra alone. The decomposition highlights the influence and extend of individual dielectric relaxation

processes and losses due to electrical conduction to the overall fit of the data. The complexity of the underlying media model increases from the top to the bottom row of sub-figures, in analogy to the fitting example in Fig. 6.4. The criterion for a reasonable fit of the dielectric permittivity spectra was an rRMS error $\leq 1\%$.
The initial wavelet of the FDTD simulation near the source point is shown in the first sub-figure row. The source itself is located inside the soil. In order to compare only the effect of the soil properties on the propagating wavelets, without the influence of the antenna near-field, the initial wavelets for the 100 MHz and 1 GHz simulations are received at 15 cm and 5 cm distance from the source, respectively. As a consequence and at first approximation, the original ricker impulse on the antenna takes the form of its second derivative at the beginning of the antenna far-field. The wavelets that propagated 1 or 2 m through the soil, which is described by different media models with increasing complexity, is shown in the rows underneath. The first column of sub-figures corresponds to the normalized amplitude versus travel-time A(t) of the 100 MHz wavelets after a propagation distance of 2 m from the source (for the initial wavelet in the first raw the propagation distance is 0 m). The second column shows the normalized amplitude of the frequency spectrum A(f) of the wavelets (vertical colored line: center frequency). Analogously to the 100 MHz wavelets, the same is shown in columns five and six for the 1 GHz wavelets, but at a distance of 1 m from the source (at HF, we chose a shorter distance for the wavelet analysis, due to much stronger signal attenuation). An overview of the results of the wavelet analysis using different characteristic wavelet properties (see previous section) for all soils, fitting models and both frequencies is shown in terms of bar diagrams in Fig. 6.10. The wavelet analysis of each soil is discussed in the following.

6.3.1. Sand

Fig. 6.5 shows the simulation and fitting result for sand. The attenuation spectrum of the measured data (column 3) is typically low for sand at low frequencies. At higher frequencies (above 300 MHz), attenuation increases exponentially. The data show scattering artefacts at around 400 MHz as described in the 'Dielectric Permittivity Measurement' section. In contrast to attenuation, phase velocity is predominantly constant in the 10 MHz to 10 GHz frequency range. Using a model with constant parameters for ε and σ (row 3 from the top) perfectly enables to describe the entire velocity spectrum, but fails to describe attenuation at HF above $\approx$ 300 MHz. In contrast, an accurate fit of the complex permittivity data (rRMS error = 0.9%) and accordingly the velocity and attenuation in the considered frequency range can be achieved using a one-pole Debye model for the dielectric polarization in combination with a dc-conductivity term describing the conduction losses (ε: 1 Debye, $\sigma = \sigma_{dc}$; row 4 from the top). Herebye, the Debye relaxation describes the relaxation of free water molecules that occur at HF, which is entirely responsible for the strong rise of attenuation (see grey shaded zones). Adding more Debye relaxations (2 or 3 Debye poles) to

the media model (rows 5 and 6 from the top) did not considerably improve the fitting result (rRMS error = 0.8%).
Regarding the simulation results, the 100 MHz wavelets (first column) at 2 m distance (black lines) show no difference to the starting wavelet at 0 m (grey line), independent of the underlying media model, which is confirmed by the cross-correlations (cc - 0m and cc - 3 Dby) of the wavelets (Fig. 6.10). Therefore, for a nearly saturated sand one can use constant parameters to accurately simulate GPR at 100 MHz center frequency. However, assuming an antenna frequency of 1 GHz attenuation becomes strongly frequency-dependent. Therefore, with respect to the wavelet analysis (Fig. 6.10), the assumption of constant media parameters underestimates attenuation (α by 18 dB/m at 1 GHz center-frequency) and the subsequent shift of the center-frequency (f_c; from 1 GHz down to 600 MHz) plus an elongation of the wavelet (we; of around 70%). The differences of wavelet travel-times t only vary slightly (by smaller than 1 ns) between the constant parameter model and the single Debye pole model. Interestingly, the 1 GHz-wavelet after 1 m propagation and assuming a 1-Debye medium (row 4) for the sand only correlates 70% to the original wavelet, which shows the strong influence of attenuation dispersion at HF. In contrast, the 100 MHz wavelet after 2 m propagation remains 100% correlated to the start wavelet.

6.3.2. Sandy loam

The simulation and fitting result for the sandy loam is shown in Fig. 6.6. Both, attenuation and velocity spectra depend on frequency. Similarly to the sand, the data show scattering artefacts at around 500 MHz probably caused by the coarse part of the mineral matrix (70% sand content). From 10 MHz to 1 GHz the attenuation increases from 4 to 40 dB/m and above 1 GHz it further increases exponentially with frequency. The velocity dispersion increases with decreasing frequency, which is due to the increasing influence of dc-conductivity and interfacial relaxation effects (cf. Eq. 6.3) and reaches a plateau of 0.073 m/ns at above 1 GHz. The best fit (rRMS = 0.7%) of the dielectric data can be made assuming a 3-pole Debye relaxation model together with a constant dc-conductivity term (ε: 3 Debye, $\sigma = \sigma_{dc}$; row 6). In contrast, a model consisting of 2 Debye poles and a dc-conductivity term (row 5) seems to be appropriate as well (rRMS error = 1.3%), but it yields distinct discrepancies in the simulation result, as will be discussed further down. The application of constant parameters for ε and σ does not accurately fit the measured data (cf. row 2 and 3). Albeit we notice that frequency-independent media parameters also create dispersion, which is due to the increasing influence of the conduction current with decreasing frequency. So, the higher σ_{HF} (with $\sigma_{HF} >> \sigma_{dc}$), the further velocity dispersion reaches into the high frequency range. In our measurements, this transmission dispersion effect (Annan, 1996) was limited to frequencies below ≈50 MHz. Fitting constant media parameters to the data, we can approximately follow the general dispersive trend of the velocity

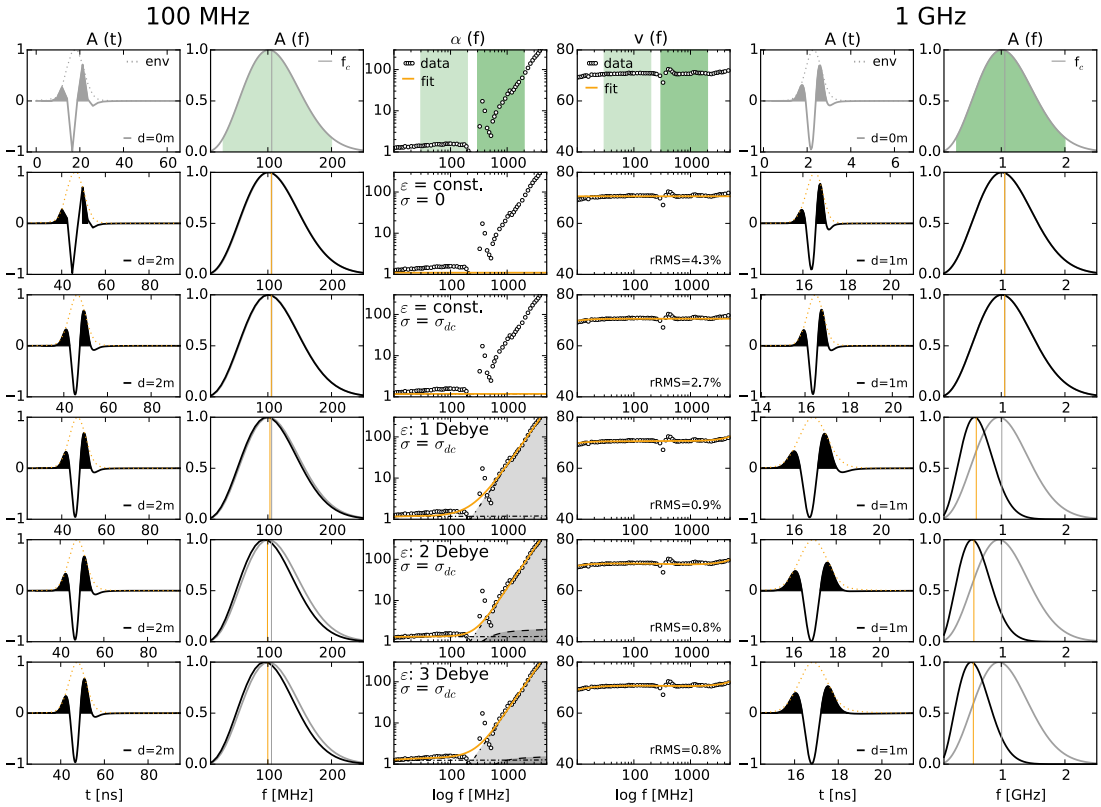

Fig. 6.5.: Sand: simulated 100 MHz and 1 GHz wavelets with normalized amplitude A(t) and amplitude spectrum A(f) (vertical orange line: center frequency f_c) after propagating distance d in sand described by varying underlying media models (sub-figure row 1: start wavelet; row 2 and 3: constant media parameters (ε, σ); rows 3 to 6: 1 Debye, 2 Debye and 3 Debye relaxation models and constant σ_{dc}. The start wavelet (d=0m) in the top row (grey line) and the propagated wavelets (black line) and their envelopes (dashed orange line) after 2 m (for 100 MHz) and 1 m (for 1 GHz) distance. The dashed line and grey shaded zones (cf. Fig. 6.4) indicate the contribution of an individual Debye model to the overall fit. The top row green shaded areas mark the bandwidth of the start signal. Column 3 and 4 show attenuation and velocity spectra together with their model fits (orange line: overall fit; dashed black line and shaded areas: 1st, 2nd & 3rd Debye model). Green shaded columns in the first row indicate the bandwidth of the source wavelet. The colored line in row 2-6 of the attenuation and velocity spectra show the overall fit (with rRMS error).

curve, but we cannot fit frequency-dependent attenuation data, especially not at HF. With respect to the fitting result and for the following discussion, we assume that the simulation of a wavelet propagating in the 3-pole Debye medium (row 6) is the most realistic result. The shift of the center-frequency (f_c) as seen in the frequency spectra of the wavelets (Fig. 6.6, column 2 and 6) and in the bar diagram in Fig. 6.10 is 21 MHz for the 100 MHz wavelet and gets overestimated in the simulation assuming a 2-pole Debye medium. When using constant parameters or a 1 Debye relaxation model the frequency shift is underestimated. Similarly for the wavelet elongation (we) at LF, which is slightly smaller for the model with the highest complexity in comparison to the simulation with the 2-pole Debye model. The cross-correlation of the wavelet in the 3-pole Debye medium with the initial wavelet (cc - 0m) at 2 m distance from the source is 90%, which is 20% more than assuming a 2-pole Debye medium. The atten-

uation α at 100 MHz is roughly the same for all models (around 11 dB/m).
In case of the 1 GHz wavelet, the frequency-shift (f_c) is much more pronounced. Assuming the most accurate model (3 Debye, last row) the shift is 500 MHz, which corresponds to half the bandwidth of the initial wavelet. The shift gets increasingly underestimated assuming a less complex media model for the simulation. At 1 GHz, attenuation α, which was calculated on basis of the amplitude difference between start and distant wavelets, is 40 dB/m and matches very well with the fitted value in the attenuation spectrum (based on the dielectric spectroscopy data). In contrast, with decreasing model complexity, α gets increasingly underestimated. However, the 1 GHz wavelet that propagated 1 m in the 3-pole Debye medium only correlates 50% with the initial wavelet (cc - 0m). Hence, the shape of the wavelet strongly changed during wave propagation. Furthermore, the correlation of the 1 GHz wavelet propagating in the 3-pole Debye medium with the wavelets propagating in less complex media (cc - 3 Dby), decreases with decreasing complexity.

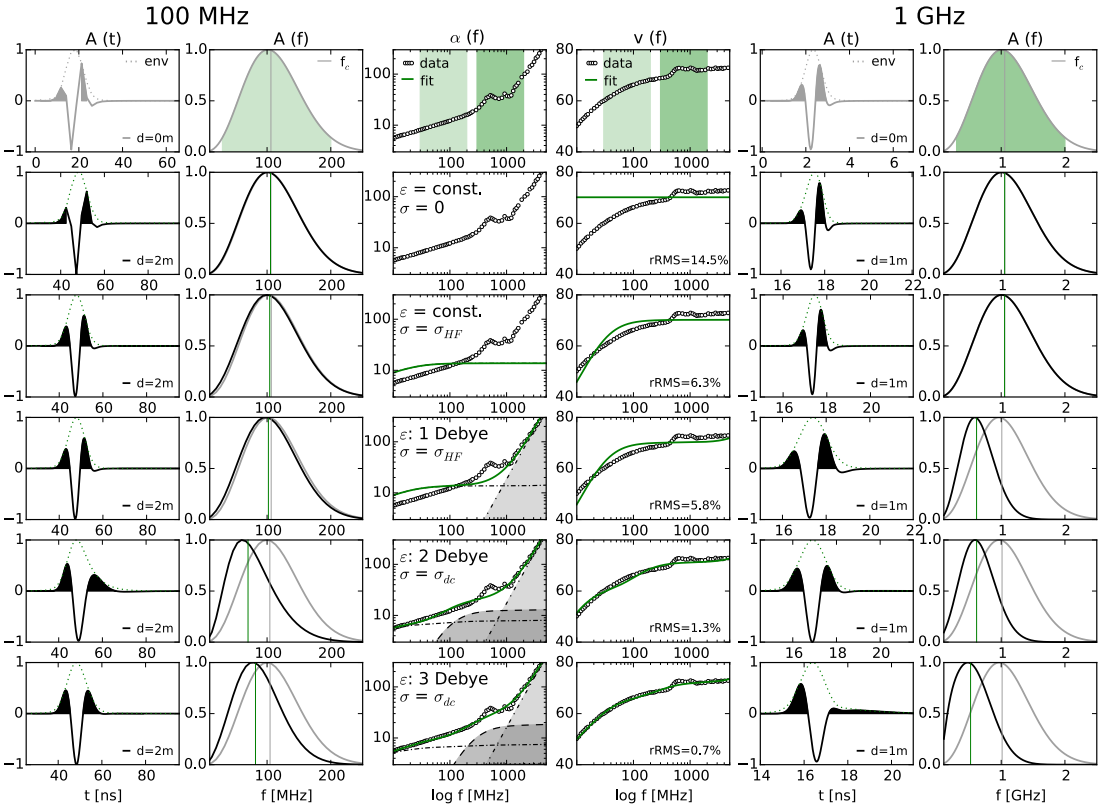

Fig. 6.6.: Sandy loam: Simulated 100 MHz and 1 GHz wavelets and spectra after propagating a distance d. The medium is described by varying underlying media models (row 2 to 6). Column 3 and 4 show attenuation and velocity spectra together with the model fit (green line). Further description is analogue to Fig.6.5.

6.3.3. Clay

Fig. 6.7 shows the simulated radar signal and fitting results of the dielectric data for the clay. The attenuation and the velocity spectra of the moist soil sample are both dispersive in a wide frequency range. In the 50 to 150 MHz-frequency band of the 100 MHz wavelet, frequency-dependent attenuation varies between 10 and 18 dB/m (80%) and velocity varies between 0.058 and 0.065 m/ns (12%). In the frequency-band of the 1 GHz wavelet, attenuation varies between 35 and 80 dB/m (129%) and velocity between 0.07 and 0.075 m/ns (7%), which suggests that wavelet changes at high frequencies are basically controlled by attenuation. The best fit of the attenuation and velocity spectra can be achieved using a 3-pole Debye relaxation plus the dc-conductivity term σ_{dc} (row 6; rRMS=0.9%). Whereas at 100 MHz, a 2-pole Debye model seem to fit the data adequately, 3 Debye relaxation poles become necessary, in order to improve the poor fit of the attenuation spectrum in the 400 MHz to 1.5 GHz frequency range. For this rather fine-grained soil, the influence of interfacial relaxation

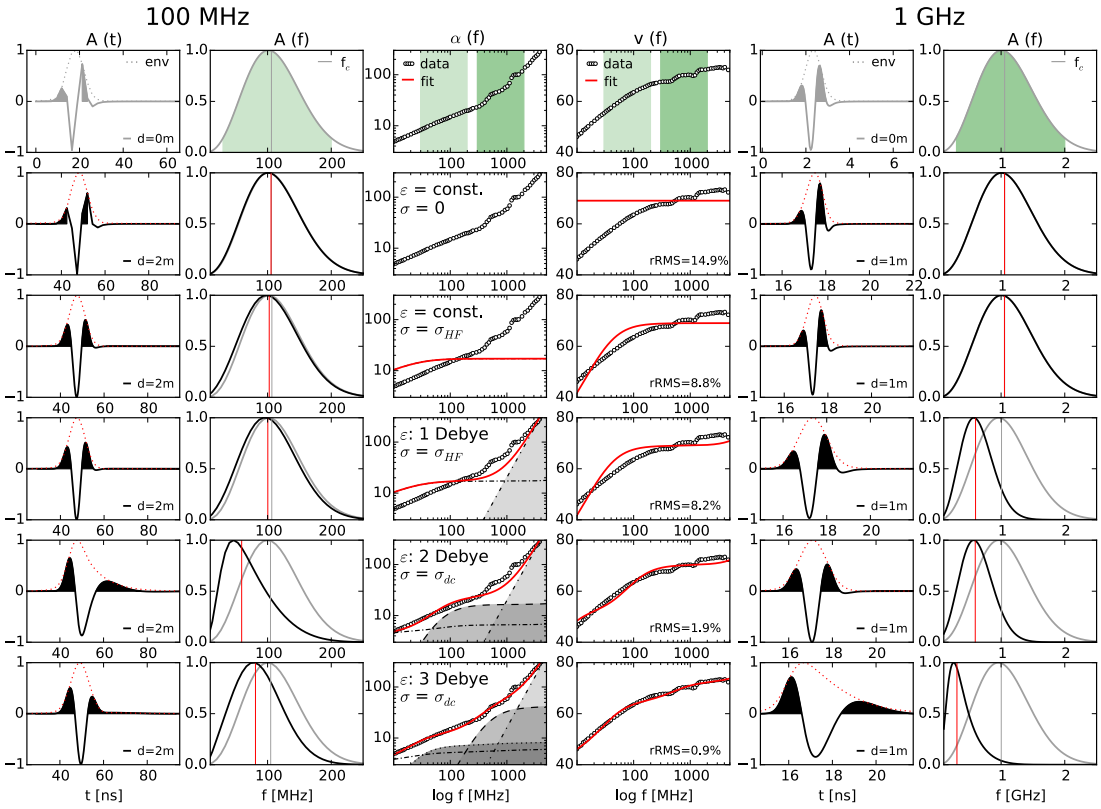

Fig. 6.7.: Clay: simulated 100 MHz and 1 GHz wavelets and spectra after propagating a distance d. The medium is described by varying underlying media models (row 2 to 6). Column 3 and 4 show attenuation and velocity spectra together with the model fit (red line). Further description is analogue to Fig.6.5.

of bound and hydrated water at the mineral-water interfaces the Maxwell-Wagner effect becomes severe, which create distinct and relatively broad dielectric relaxation

effects in the lower to upper MHz frequency range. The broadband interfacial relaxations can be adequately described by 2 Debye relaxations with center-frequencies at 20 MHz and 450 MHz.
In the 100 MHz case and considering the simulation result for the 3-pole Debye media model (row 6), the frequency-shift (f_c) of the wavelet at a distance of 2 m from the source is 25 MHz (Fig. 6.10). The shift gets overestimated (by a factor of 2) using only 2 Debye poles in the dispersive media model description and neglected when using constant electrical parameters. The measured travel-times t at maximum envelope of the different wavelets vary between 30 ns and 34 ns. The wavelet that propagated 2 m through the 3-pole Debye media correlates 80% with the initial wavelet (cc - 0m), whereas in case of the 2-pole Debye medium correlation is only 50%. Attenuation α (determined by the wavelet envelopes) decreases with increasing model complexity for the 100 MHz wavelet, reaching 12 dB/m for the 3-pole Debye case, which matches the attenuation in the spectrum at 100 MHz. In contrast and similarly to the sandy loam, attenuation α increases for the 1 GHz wavelets with increasing model fit precision. At 1 GHz, attenuation is 50 dB/m in the 3-pole Debye model, both in the fitted spectrum and calculated from the wavelets. The shift of the center-frequency f_c is very high (700 MHz) for the 1 GHz wavelet and largely underestimated using simpler media models. Most striking is the distinct wavelet elongation (we= 2.8, or 180%) for the 1 GHz wavelet, when using the 3-pole Debye model in comparison to the other models. Furthermore, the cross-correlation of the wavelet with the starting wavelet is less than 10%. Both observations are in contrast to the result with more simplified media models with much less apparent elongation of the wavelet. This can be attributed to the more precisely fitted attenuation in the high frequency range, which at 1 GHz generates 60 dB/m in the 3-pole Debye model and only 40 dB/m in the media model with 2 Debye poles. Again, we need to emphasize that we tried to fit the entire measured spectrum from 10 MHz and 10 GHz with the different models and not the reduced spectrum of the individual GPR wavelets.

6.3.4. Loam

The comparison of simulated wavelets with different underlying media models of the moist loam sample can be observed in Fig. 6.8. Similar to the clay, attenuation and velocity spectra are both strongly frequency-dependent. However, the dc-conductivity of the loam is approximately twice as high ($\sigma_{dc} = 32$ mS/m, cf. Tab. 6.2) in comparison to the clay ($\sigma_{dc} = 15$ mS/m), which can indirectly be seen at the attenuation spectrum, where at the lowest measured frequency (10 MHz) the attenuation is much higher than for the clay. This observation is interesting, since the texture of the loam only contains half the clay fraction in comparison to the clay soil and therefore, one would expect the clay to be more conductive then the loam. However, the clay sample is laterite, which generally undergoes strong weathering in a tropical environment during soil genesis. The weathering and type of parent rock controls the clay mineral synthesis and there-

fore, the cation exchange capacity of the clays, which in turn strongly influences the dc-conductivity of the soil. In contrast to the clay, the loam has a higher CEC, which indicates that the parent rock underwent less chemical weathering.

The phase velocity of the loam decreases linearly with frequency below approxi-

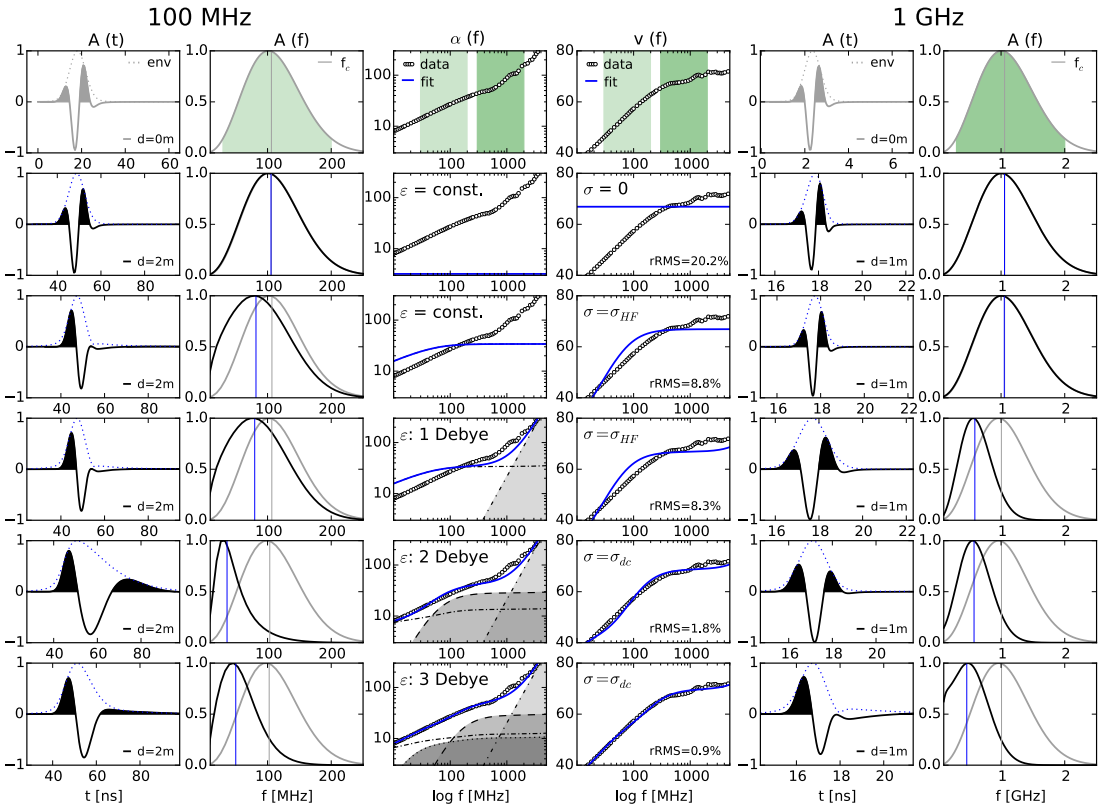

Fig. 6.8.: Loam: simulated 100 MHz and 1 GHz wavelets and spectra after propagating a distance d. The medium is described by varying underlying media models (row 2 to 6). Column 3 and 4 show attenuation and velocity spectra together with the model fit (blue line). Further description is analogue to Fig.6.5.

mately 300 MHz. Above 300 MHz it slightly varies between 0.068 m/ns and 0.072 m/ns (6%) and at 5 GHz, the velocity has not reached its maximum yet. The most accurate fit across the spectrum was achieved using the maximum number of Debye models (ε: 3 Debye; row 6) and one σ_{dc} term (rRMS error = 0.9%). Even so, fitting the model with 2 Debye terms (rRMS error = 1.8%) comes close to it, the attenuation is again slightly overestimated around 100 MHz and underestimated in the 1 GHz area. Analogue to the other results, the fit is getting worse with decreasing complexity of the dispersive media model.

In case of a 100 MHz wavelet and considering the simulation result with the most accurate media model (row 6), the shift of center-frequency (f_c) of the wavelet at a distance of 2 m from the source is 50 MHz (Fig. 6.10), which is twice as much as for the clay. This is attributed to the higher attenuation of 28 dB/m at 100 MHz in contrast to 14 dB/m for the clay and in turn, basically attributed to a higher σ_{dc}. The shift of the

center-frequency gets overestimated by 18 MHz assuming 2 instead of 3 Debye media models. The same holds for the wavelet elongation, which is almost 160% in comparison to the start wavelet for the 2-Debye model, but only 60% for the propagation in the 3-pole Debye medium. Attenuation is overestimated by 23% using either constant electrical parameters, or a 1 Debye instead of a 2 or 3 Debye relaxation model. The wavelet that travelled through a medium with zero conductivity (row 2) now correlates only 40% with the wavelet that propagated through the most accurate model (row 6; cc - 3Dby). In accordance to this observation, the wavelet that propagated through the accurately described medium (row 6) correlates 40% with the initial wavelet. So, for the moist loam and at low frequencies as 100 MHz, the influence of dc-conductivity in comparison to the dielectric relaxation losses on the wavelet properties becomes severe. For the 1 GHz wavelet, the differences in the (apparent) wavelet elongation for the propagation in the 2 different multi-Debye models, the cross-correlation and the frequency-shift seem to be smaller and fitted attenuation only varies between 58 dB/m and 61 dB/m. This can be attributed to the fact that one major part, the losses due to electrical conduction (σ_{dc}) is more or less fixed, since the inversion process revealed very similar values (32 mS/m vs. 36 mS/m, cf. Tab. 6.2). However, the difference to the case were constant parameters for the media description are assumed is striking and emphasizes again the need to use frequency-dependent media parameters for fine-grained soil material.

6.3.5. Silty clay

Fig. 6.9 shows simulations for the 100 MHz and 1 GHz wavelets and fitting results for the silty clay sample. In all aspects of the presented data, the silty clay provided the most extreme results among the investigated soils. It has the highest clay (44%) and silt (49%) content and the highest CEC (18.5 meq/100g). At 1 GHz frequency, attenuation almost reaches 100 dB/m, which is in a region where GPR clearly fails due to the dynamic range limitation. Both attenuation and velocity are strongly dispersive. The dc-conductivity of the silty clay ($\sigma_{dc} = 85$ mS/m, cf. Tab. 6.2) is 2.5 times higher than the conductivity of the loam, which causes a distinct up-shift of the measured attenuation spectrum to higher values. At the lowest frequency of 10 MHz, attenuation is as high as 14 dB/m, which corresponds to the same value for sand (at the same moisture level), but at 800 MHz. Phase velocity decreases linearly with frequency below frequencies of approximately 500 MHz. The best fit can again be achieved using the 3-pole Debye relaxation (ε: 3 Debye, row 5) and a constant σ_{dc} term (rRMS error = 0.5%). However, fitting a 2-pole Debye model (rRMS error = 1.6%) seems to be quite accurate as well and for the simulation with the 100 MHz wavelet it might suffice, but not for the simulation with higher frequencies. In contrast, using constant parameters requires a HF conductivity of $\sigma_{HF} = 175$ mS/m, which is beyond the conductivity range, where HF sensing techniques like GPR is typically used.
For the 100 MHz wavelet, the (apparent) wavelet elongation is 100% considering 3

Debye models and the frequency shift is 70 MHz with an attenuation of 35 dB/m. The values differ by approximately 10 to 15% if we assume a 2 Debye media model. The correlation between the wavelet (2, 3 Debye) at 2 m distance and the initial wavelet is only 20%. The variation of travel-times of the 100 MHz wavelets with respect to the different media models varies distinctly between 51 ns and 57 ns. This is due to the strong overestimation of attenuation, when assuming constant constitutive parameters or a single-pole Debye relaxation. This overestimation generates very high conductivities (σ_{HF}) that cause a frequencies shift of more than 80 MHz, which in turn distorts the signal. For 1 GHz wavelets the frequency-shift gets underestimated by more than 400 MHz when using constant parameters instead of frequency-dependent parameters and reaches a maximum of 900 MHz (f_c-shift). Attenuation calculated on basis of the wavelet decay is 95 dB/m, which matches the fitted value in the attenuation spectrum at 1 GHz. Thus, the elongation of the wavelet is 200% (we=3), which gets clearly underestimated with simpler dispersion models. Furthermore, the shape of the wavelet strongly deviates from all other wavelets based on simpler models, since the correlation among each other is below 20% in all investigated cases (cc - 0m, cc - 3 Dby).

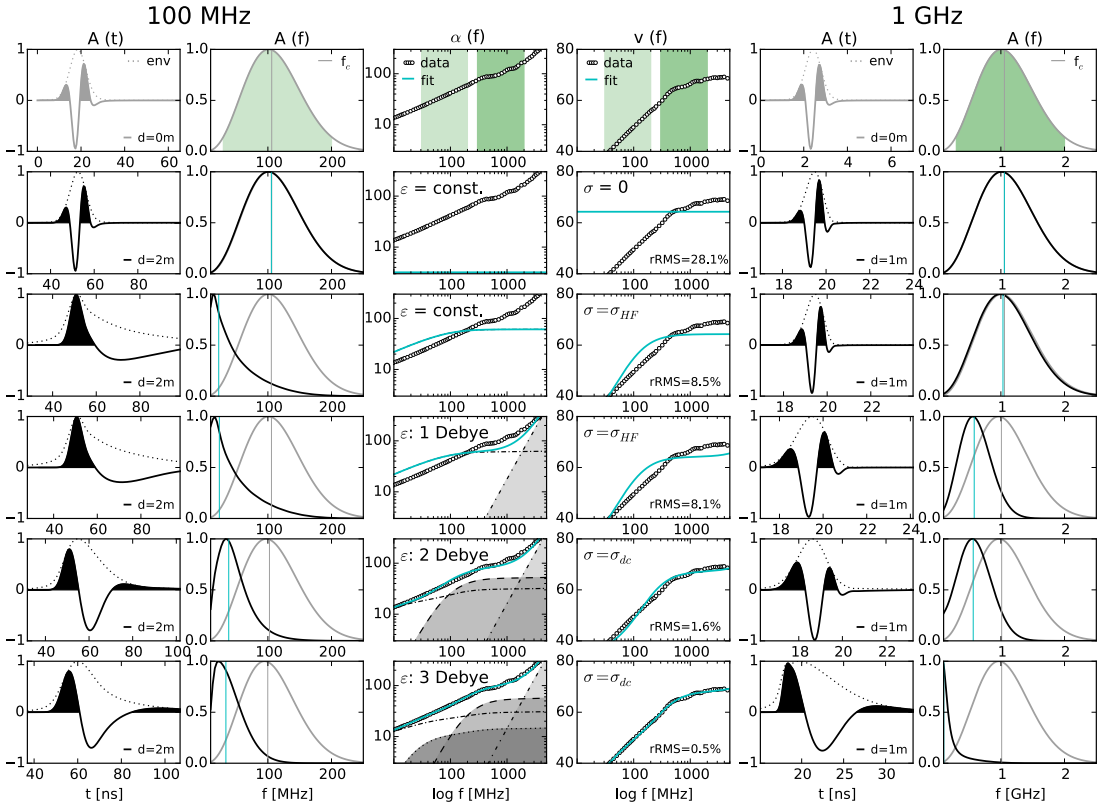

Fig. 6.9.: Silty clay: simulated 100 MHz and 1 GHz wavelets and spectra after propagating a distance d. The medium is described by varying underlying media models (row 2 to 6). Column 3 and 4 show attenuation and velocity spectra together with the model fit (cyan line). Further description is analogue to Fig.6.5.

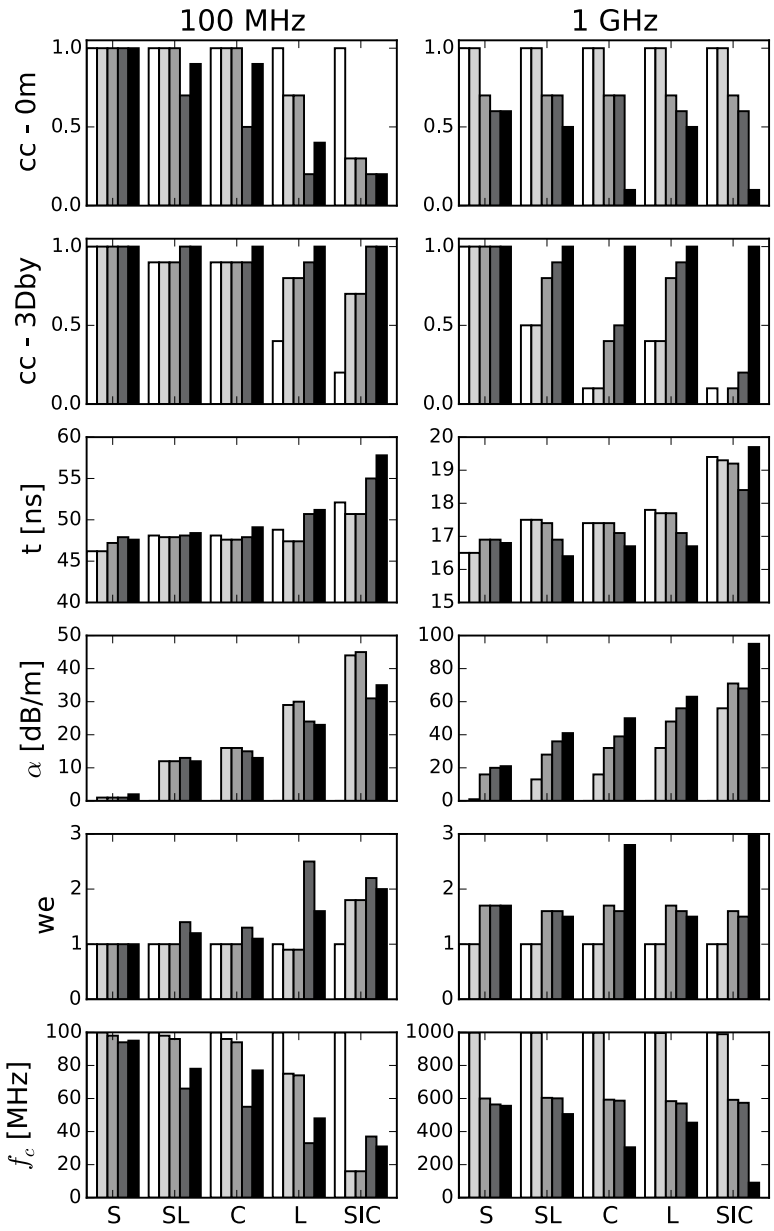

Fig. 6.10.: Analysis of the 100 MHz and 1 GHz wavelets that propagated through the soils (S: sand, SL: sandy loam, C: clay, L: loam, SIC: silty clay) in Tab. 6.1 with respect to the different underlying media model (bars; Tab. 6.2 and Figs. 6.5-6.9): Cross-correlation with the initial wavelet (cc - 0m); cross-correlation with the wavelet that propagated through the 3-pole Debye medium (cc - 3 Dby); travel-time (t) at maximum wavelet amplitude for distance d; wavelet attenuation (α); wavelet elongation (we) and center frequency (f_c).

6.3.6. Soil comparison over distance

In addition to the observation of the influence of the media model on the wavelet at a single distance (2 m for 100 MHz and 1 m for 1 GHz), we also analyzed the change of the wavelet with respect to several propagation distances d. The chosen examples

depict the importance of incorporating realistic media models for FDTD simulations. The sandy loam (humus) of this study is a medium soil concerning radar performance. It has a low dc-conductivity (σ_{dc} = 20 mS/m) and consist of 70% sand. However, as shown in Fig. 6.6 and Tab. 6.2, if we had assumed a simplified media model to describe the sandy loam, e.g. with constant parameters, we would underestimate important wavelet characteristics, which in turn will result in completely different simulation outcomes.

Fig. 6.11 shows the normalized wavelet travel-time and its frequency-spectrum of

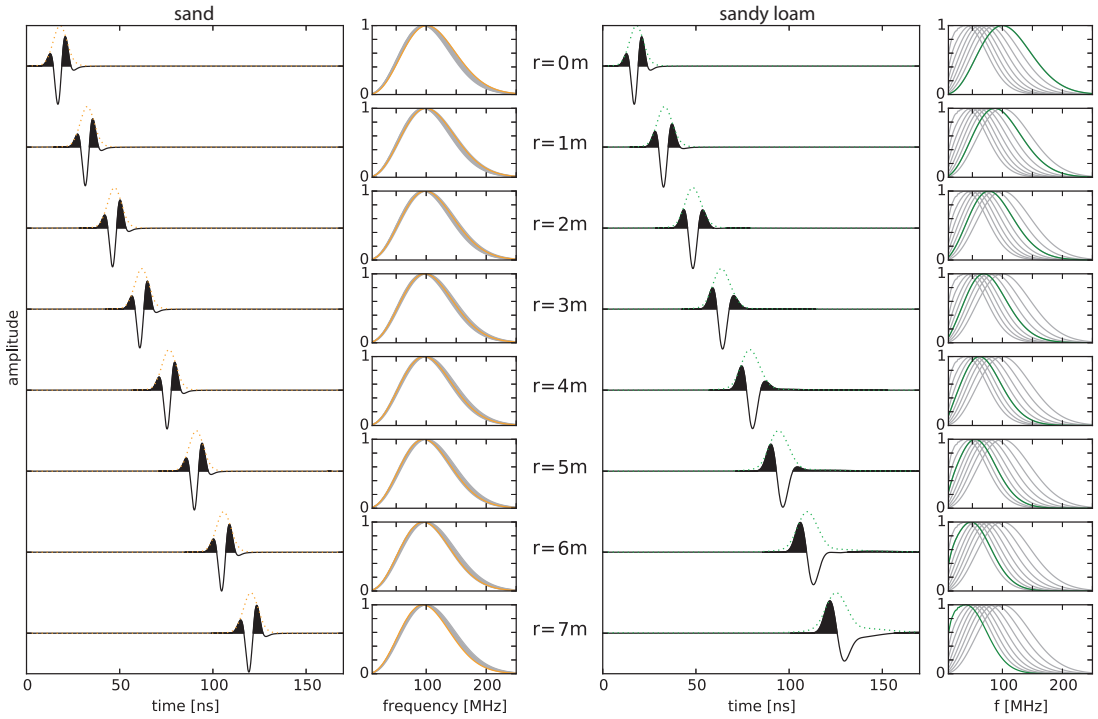

Fig. 6.11.: Simulation of a 100 MHz ricker wavelet propagating in sand (yellow line) in comparison to sandy loam (green line) across a distance of 7 meters. The envelope of the normalized wavelet is shown in dashed lines and the normalized frequency-spectrum is shown to the right of each radar trace.

a 100 MHz source for the sand and the sandy loam; both media with generally good GPR performance. The wavelets (black line) are corrected for spherical divergence (multiplication by $\sqrt{(d)}$) and their envelopes (dashed line) are plotted at each meter for an overall propagation distance of 7 meters from the source. The underlying media model comprises 1 Debye model for the sand (rRMS error = 0.9%; Fig. 6.5) as this simple model showed to describe the electrical properties accurately and a 3-term Debye model for the sandy loam (rRMS error = 0.7%; Fig. 6.6). Furthermore, Fig. 6.12 shows the wavelet analysis of the simulated radar traces (Fig. 6.11) with the decay of the envelope amplitude, the cross-correlation between the propagated wavelets and the initial wavelet, the shift of center-frequency and the wavelet elongation with propagation distance. The wavelets of the sand shows no change of their shape during

propagation. The cross-correlation with the start wavelet is 1 for all wavelets at each distance and wavelet elongation is in the order of 5% at 7 m distance. The maximum frequency-shift is 8 MHz and the amplitudes decay is very slow with approximately 50% decay after 4 m (or 1.5 dB/m). In contrast, the wavelet propagating in the sandy loam strongly changes with propagation distance. The second amplitude maximum of the normalized wavelet decays with propagation distance and after 5 m distance becomes completely blurred. At 7 m distance from the source the wavelet is only 33% correlated with the initial wavelet and the wavelet elongation is more than 50%. The amplitude decay is very rapid. In the first 3 m the amplitudes (corrected for spherical spreading) decay to 1% of its initial level at the source ($\approx$ 13 dB/m). Furthermore, the frequency-shift is strong with approximately -10 MHz per meter, in comparison to the sand with $<$ -1 MHz per meter.

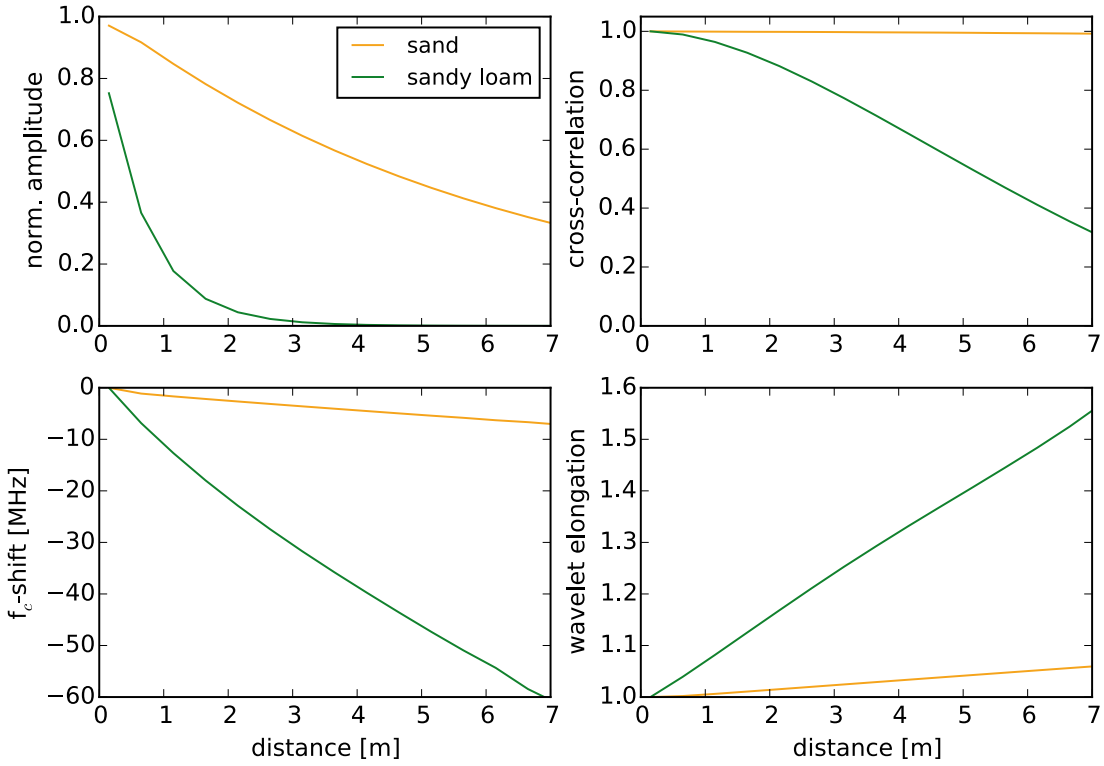

Fig. 6.12.: Wavelet analysis of the radar trace simulation for sand and sandy loam (Fig. 6.11) with the decay of the envelope amplitude (normalized amplitude), the cross-correlation of the initial signal (r=0 m) with the wavelet at at r=1-7 m, the shift of the center-frequency (f_c-shift) and the wavelet elongation with respect to the traveled distance.

6.4. Conclusions

We carried out 2D simulations of the electromagnetic wave propagation in five different soils with the focus on an accurate description of the electrical frequency-

dependent media parameters. The complex effective dielectric permittivity of the soils was measured in a CTL in a frequency range between 10 MHz- 10 GHz. All soils had a similar water content, but different textures ranging from sand to silty clay. With decreasing grain-size fraction the attenuation increased in the GPR frequency-band, which can be attributed to the increased interfacial relaxation effect of the Maxwell-Wagner type and the bound or hydrated water relaxation at LF. The silty clay had the highest silt and clay content and the highest CEC among all soils of this study and would strongly limit the GPR application. Assuming a common-offset ground-coupled GPR system with 100 dB dynamic range would cause a transmitted 100 MHz signal to become undetectable in the silty clay ($\alpha = 35$ dB/m) after a two-way travel distance of 3 m (corresponding to 1.5 m investigation depth). Using a signal with 1 GHz center frequency and adding losses due to factors like scattering, surface roughness and soil heterogeneity to the electrical absorption, GPR is very unlikely to succeed in the silty clay. However, in case of more sandy soils with less energy absorption, the distortion of the propagating wavelet (which is strongly affected by the dispersive electrical parameters) could be used in order to derive petro-physical parameters like texture and CEC.

However, the application of realistic dielectric media models requires very small time increments for the simulation that must be shorter than the free water relaxation time. Fortunately, equality of the time steps with the CFL condition (default in gprMax) for numerical stability can be modified by introducing a time-step stability factor, which in turn made the choice for the spacial discretization less dependent from the time discretization. However, due to simulations with high GPR-frequencies in media with relative high relative dielectric permittivity ($\approx$25) the shortest wave length were less than 30 mm. Using a spacial discretization of 2 mm for the 1 GHz simulations and an accurately described dispersive media model (3 Debye) with dimensions as introduced in section 6.2.5, the computational time was not higher than 8 min, 40 s on an ordinary PC (Intel i7 processor with 2,3 GHz speed, 4 cores, 16 GB RAM). The time was reduced to 4.5 min, when using constant electrical parameters for the model description. Each additional Debye-term in the simulation added approximately another 1.12 min (or 25%) to the overall computational time. The 100 MHz simulations needed less computational time, since their spacial discretization was increased to 10 mm. The maximum time for the most complex model with 3 Debye relaxation was 1 min and 40 s.

Our simulation analysis shows that the influence of the chosen parameter model on the wave propagation is distinctly depending on the soil type. Apart from the sand, all soils were most accurately described in the 10 MHz to 5 GHz range by means of 3 Debye models and one dc-conductivity term. The Debye relaxation with the short relaxation times (7-9 ps) can be attributed to the free water relaxation in the lower GHz frequency range and defines the minimal Δt required by the FDTD code. The other two relaxations with longer relaxation times (0,4 - 22 ns) together describe the relatively broad interfacial relaxation effects that occur in the MHz frequency range. The sand

can be fitted using 1 Debye model for the free water relaxation alone, since interfacial relaxation effects are negligible. For frequencies below 300 MHz (dependent on the soil water content also higher frequencies are possible) the sand can quite accurately be described with constant electrical media parameters. Therefore, a larger discretisation can be chosen for the FDTD simulation . In contrast, in the shown simulation in the more fine-grained soils, the application of constant media parameters strongly underestimated the attenuation dispersion at HF and velocity dispersion at LF. This goes on the expense of an underestimated frequency-shift and elongation of the wavelet. The precise fitting of these effects was only possibly using multiple-pole Debye models. In fact, it could be observed that the FDTD simulation is very sensitive to the chosen media model and that apparently small changes or deviations in the model fit of the measured data produce a different simulation outcome. Therefore, it is recommended to measure the complex dielectric permittivity of the soil in the survey area in the considered GPR frequency band and incorporate them in the simulation model by means of muliple-pole Debye terms. This is especially important for future studies, which aim at interpreting wavelet shapes to derive further physical and chemical soil properties. In the future, further investigations have to be carried out in order to systematically analyse the interdependencies of water content, texture and (clay) mineralogy of a soil and its electromagnetic response.

7. Discussion and Outlook

The following chapter discusses how different topics covered in this thesis can be used and developed further. The new findings may have an impact on a better principal understanding of single polarization and relaxation mechanisms using complementary methods or the improved data processing using new algorithms. On the other hand, the findings may be of practical use and e.g. extend the spectrum of application areas for well-established EM measurement techniques and for numerical simulations. In a general view, each subsection of this chapter is thematically tied to measurement and analysis of frequency-dependent electrical soil properties and the fundamental technical methods, which were presented in the papers. The methods consist of electrical spectroscopy, TDR and FDTD simulations for analysis of the EM wave propagation.

New insights on dielectric relaxation mechanisms

As described in the thesis, the frequency-dependent response of soils in an alternating EM field is composed of different polarization and relaxation mechanisms. The relaxation at very high frequencies with relaxation times in the picosecond range is attributed to the relaxation of free water molecules. For fine-grained soils the relaxation times, which were calculated by model fitting are often shifted to slightly longer times than they were found at the analysis of pure water in the same frequency range. The effect was attributed to hydrogen network fluctuations of free water and to the overlay with strong interfacial relaxation effects taking place in the microwave frequency rage (Wagner et al., 2013). However, in order to examine if the effect has physical reasons or if it is caused by model fitting of a process that occurs beyond the measured frequency range (relaxation frequency of free water is 17 GHz at 20°C and the upper measurement limit is 10 GHz), the measured frequency range would need to get increased (to ≈30 GHz).
The attempt for an isolated examination of the relaxation of bound or hydrated water, which for instance can influence the water or nutrient supply of plants, is a bigger challenge. The relatively high-frequency relaxations in the upper MHz ranges at fine-grained soils attributed to adsorption and desorption exchanges at clay surfaces and high-frequency counter-ion relaxations are complemented by low-frequency processes (Maxwell-Wagner effect, LF counter-ion relaxation), which can superimpose the high-frequency processes (Wagner et al., 2013). A discrimination between the bound-water relaxation process and other relaxation processes can for instance be reached under the assumption of certain thermodynamic models that incorporate the activation enthalpy

of water with respect to the matric potential of the soil (Hilhorst et al., 2001; Wagner and Scheuermann, 2009). In this context, it is also conceivable to combine dielectric spectroscopy with nuclear magnetic resonance (NMR), which can be used to distinguish water with different binding forms. However, the definition of different binding strength is different for each individual analyzing technique (NMR, dielectric spectroscopy, tensiometry, etc.). So, in a first step it should be clarified, what bound water from a NMR perspective is and what can be considered to be bound water from the dielectric spectroscopy perspective (e.g. the dependence of the relaxation properties from a certain distance of water molecules from the mineral surface and the activation enthalpy are currently research topics). In this connection, the model by (Boyarskii et al., 2002) can get tested and enhanced.
An observation that was also made in this thesis applies to the connection between the relaxation strength of bound water (and also Maxwell-Wagner effect) and the level of cation exchange capacity of the soil. Accordingly, the inclusion of clay mineralogy in the systematic analysis of the connection between CEC and the broad distribution of relaxations in the kHz to MHz range, especially for clayey soils is necessary. The specific surface area (SSA) of soils is strongly connected to the clay content and CEC, and the fractale dimension of the grain size distribution correlates positively with the clay content and negatively with the sand content in most soils (Ersahin et al., 2006). This indicates that it could be possible to get information on the CEC and the fractal dimension of the grain size distribution using the frequency-dependent polarization and relaxation behavior of a soil.
In order to cover the broadband Maxwell-Wagner effect and to differ it from the low-frequency counter-ion relaxations, broadband measurements are needed that cover at least the lower kHz and the upper MHz frequency range. The ultra-broadband dielectric spectroscopy introduced in chapter 5, which combines SIP together with the CTL method is generally able to do that. However, it is very time-consuming for a big number of samples, since two different cells with non-identical samples have to be used in each method and can fail in case of dry samples due to a lack of electrical coupling in the cell. In addition, the frequency gap between 45 kHz and 1 MHz must be closed using a third method in order to preclude failures. Bobrov et al. (2015) for example introduced a single uniform cell for dielectric spectroscopy of soils with a LCR meter and a VNA in the frequency range from 42 Hz to 8.5 GHz.
Regarding the calculation of permittivity from the measured S-parameters in the CTL method, there is demand for a single algorithm that can cover the whole frequency band from 1 MHz to 10 GHz without mixing the results of 2 algorithms (in this thesis the PM method was used for low-frequency (< 2 MHz) and the Fast algorithm for higher frequencies (≥ 2 MHz); see section 3.2). A conceivable approach could be the enhancement of the PM method itself or otherwise, an iterative direct fit of the S-parameters using a generalized dielectric relaxation model (see Wagner et al., 2013).

Exploiting the full potential of TDR in the field

The field moisture sensor on basis of TDR was calibrated in an elaborate procedure as described in sections 4.5 and A.2 so that GPR performance can be directly assessed. However, the calibration and regression equation is only valid for the identical type of sensor with coated rods. Furthermore, the TDR-amplitude at a particular time in the measured TDR signal, which is attributed to the high-frequency conductivity (or intrinsic attenuation) and the permittivity is picked internally and cannot be modified. Thus, the calculation of high-frequency conductivity or attenuation according to Topp et al. (1988) or Dasberg and Dalton (1985) cannot be carried out. In this connection, the application of a different TDR system that is more frequently used in research and which allows for a flexible wave analysis would be in favor (e.g. Tektronix 1502b or TDR100; Jones et al., 2002; Robinson et al., 2003). Apart from measurements of high-frequency conductivity, dc-conductivity and dielectric permittivity by TDR, there are also approaches that aim to derive the ion solution concentration and the matric potential (Wraith et al., 2005). Hilhorst et al. (2001) and Wagner and Scheuermann (2009) showed the relation of dielectric properties and the matric potential for fine-grained soils in frequency-domain. Thus, the question arose how the results for matric potential analysis from frequency-domain measurements with dielectric spectroscopy are interrelated to the results from time-domain measurements using TDR. Furthermore, is it possible to estimate dielectric relaxation parameters from long TDR traces or their Fourier transform?

Realistic FDTD simulation of GPR in complex media

The influence of the choice of the media model with frequency-dependent electrical parameters for dispersive and lossy soils on the outcome of a GPR simulation was shown in chapter 6. In the shown analysis the wave propagation was simulated assuming homogeneous media models. However, in order to assess the influence of soil on GPR performance to full extend, other loss mechanisms apart from the intrinsic attenuation should be considered as well, as previously described in section 3.1.2. In this context, scattering due to soil heterogeneity plays an important role. Thus, in order to receive as realistic results as possible, both influencing factors must be considered for GPR simulations. The influence of the attenuation of each individual process on the total attenuation can be accessed using appropriate simulation models for the soil heterogeneity together with realistic relaxation models for the electrical parameters. The knowledge of the influence of scattering attenuation on the total attenuation can help to further specify the validity of the GPR performance assessment using a TDR sensor. In addition, FDTD simulations can be used in order to simulate wave propagation in the coaxial cells. This could illustrate, e.g. the influence of layered and heterogeneous media, as well as possible cracks and gaps in the soil sample on the electrical response.

8. Summary and Conclusions

The presented thesis is composed of three publications, which analyzed the frequency-dependent electrical properties of different soils. The motivation behind the investigation was based on the question of how these properties can influence the performance of GPR with respect to the soil. Observations on GPR data that were collected to detect buried objects in the field have shown that attenuation as well as dispersion of GPR signals can strongly control the detection result. However, in most simulations of GPR wave propagation in subsurface models, constant parameters and simplified assumptions for the electrical properties are commonly used. Furthermore, the cause behind the frequency-dependence of the electrical properties of soils and the possibility to predict or assess them in the field had not sufficiently been investigated in the past.

In order to measure the complex effective permittivity of different soils in a frequency range that covers the entire GPR frequency range, a CTL in combination with a VNA and two measuring cells with different volumes were used. By measuring different liquids and standards it has been verified that the device was properly calibrated to measure effective permittivity in the 1 MHz to 10 GHz frequency-range. The investigated samples covered a broad spectrum of soils with varying grain size distribution, water content, mineralogical composition, clay types and organic content. The decomposition of the complex dielectric spectra using a multi-term relaxation model enabled to determine empirically the individual influence of the physical loss mechanisms with respect to frequency. With respect to the GPR method, the decomposition enabled a precise analysis of the soil-dependent attenuation and dispersion of the GPR signal. In the past, losses were generally attributed to dc-electrical conductivity of the soil and individual influences of dielectric relaxations was sometimes indicated, but not measured or covered in more depth. Furthermore, no differentiation has commonly been made between dc-conductivity and a high-frequency conductivity. This work emphasizes that GPR is influenced by the effective high-frequency conductivity, which covers the losses due to dielectric relaxation effects. Using the decomposition of measured effective permittivity spectra, two pronounced loss mechanisms could be isolated for all investigated soils: at the one hand, the relaxation due to the free water relaxation, which clearly begins to play a dominant role at the upper end of the measured spectrum, but whose maximum lies beyond this spectrum ($\approx$17 GHz at 20°C). On the other hand, the losses due to the dc-electrical conductivity, which starts to exceed all losses from frequencies below 100 MHz and which increases linearly with

decreasing frequency in the imaginary part of effective permittivity. However, characteristic for the presented thesis is the investigation of relaxation mechanisms, which cannot be attributed to the two described loss mechanisms, but which are especially pronounced in fine-grained soils. Relaxations in the intermediate range were barely considered and investigated in the past, but can play a significant role in the frequency range of GPR. In the first publication (chapter 4), it was indicated that these loss mechanisms in the intermediate GPR frequency range can be described using a single very broad relaxation based on a Cole-Cole model and that they were primarily attributed to polarization and relaxation mechanisms at grain-water inter-phases and clay interlayers. The model decomposition in individual processes indicated that, e.g. when using a GPR-system with 500 MHz center frequency in moist clay loam with low dc-conductivity of 4 mS/m, the broadband dielectric relaxation alone leads to strong dispersion effects and attenuation of the GPR signal of up to 40 dB/m, which strongly reduces the penetration depth.

However, the model fitting of the spectra indicated that the fitting parameters of the low-frequency relaxation model were badly resolved, because the peak relaxation frequency is below the measured frequency range. Therefore, the dielectric spectroscopy measurements were combined by SIP measurements in order to extend the spectrum to lower frequencies, which is a novelty. In the past, typical measurement frequencies for SIP were limited at the upside to approximately 100 to 1000 kHz. However, measurement precision of SIP equipment increased lately and with that the interest on polarization and relaxation effects that dominate at higher-frequencies. From a SIP perspective, combined data sets of dielectric spectroscopy and SIP can answer the question on how dielectric relaxations above the typical SIP frequency range influence the SIP results. Nevertheless, SIP measures different physical quantities than dielectric spectroscopy. However, this thesis showed that both methods measure complex parameters of the effective permittivity or the effective conductivity that fulfill Kramers-Kronig relation and which can be converted into each other. The combined spectra of electrical properties cover an extraordinary broad spectrum for soils (and one sandstone). It could be observed that the spectrum at very low frequencies could not adequately be described by the combination of dielectric relaxation models plus a dc-conductivity term. Thus, as shown in the second paper (chapter 5), a new semi-empirical model (CPCM) was proposed, which is a combination of two multi-term Cole-Cole models: one that is commonly used to describe SIP data at mHz to lower kHz frequencies and one, which is applied in dielectric spectroscopy to fit dielectric data above MHz frequency ranges. Extending the spectrum to lower frequencies below the common GPR frequency range and the application of the new model helped to decrease the fitting uncertainty of the broadband relaxation in the CTL spectrum. It was shown that this broadband relaxation consists of two single relaxation processes attributed to the bound water and HF counter-ion relaxation in the upper MHz ranges and a very broad relaxation in the upper kHz ranges that was attributed to the Maxwell-

Wagner effect and the LF counter-ion relaxation. The combination of the SIP and CTL spectra in comparison to each individual spectrum alone showed that the bandwidth of the measured data controls the fitting parameters of the broadband relaxations that occur in the kHz to upper MHz frequency range. Thus, in order to assess these parameters, the combination of different measuring techniques showed to be essential.

In order to predict soil suitability for GPR in the field, a device was required that enables to measure (di)electric properties. The analyses of the broadband laboratory spectra of soils clearly illustrated that the frequency of a potential measuring technique plays a crucial role. The assertion is supported by a huge number of soils using a comparison between the dc-conductivity with the effective high-frequency permittivity or intrinsic attenuation that was deduced therefrom. As a consequence, dc-conductivity as measured by geoelectrics or using induction techniques can strongly underestimate attenuation of EM waves in the soil, since dielectric relaxations that occur in the GPR frequency range are completely neglected. Depending on the type and amount of clay minerals and the water content of the soil, dc-conductivity can strongly vary and thus, dielectric relaxations due to e.g. the bound water relaxation can outreach the losses of electrical conductivity. As a cheap and easy to handle alternative, TDR shows to be a convenient tool to evaluate the soil-dependent performance of GPR. Since it measures at an effectively high frequency, it also incorporates the losses due to dielectric relaxations. A simple field moisture sensor on TDR basis was presented in the thesis, which has been calibrated for intrinsic attenuation at an effective frequency of 1 GHz. Together with the simultaneous measurement of the relative permittivity, the sensor enables to predict the performance of a high-frequency GPR system in the field.

The negative influence of dispersive and lossy soils on the propagating GPR signal was additionally verified by simulations. For the first time, data of soils that span a broad range of texture classes were measured using dielectric spectroscopy and incorporated into a FDTD code in order to create realistic dispersive media models. In contrast to the CPCM, the dielectric spectra were fitted using a multi-pole Debye relaxation approach, because in contrast to Cole-Cole type functions, the time-domain model can effectively be implemented in time-domain codes. The simulations in varying media showed that the result is very sensitive to the number of chosen Debye-poles that were used to fit the dielectric spectra. Pure sand can be described using constant parameters for electrical conductivity and permittivity in case of low GPR frequencies and a single Debye relaxation and a constant conductivity term in case of high GPR frequencies. However, rather fine-grained soils can only be described using 3 Debye poles in order to accurately fit the frequency-dependent permittivity. The fitting parameters and physical properties for the different soils are provided in the third publication (chapter 6) and can serve as database for realistic simulation experiments in the future.

A. Appendix

A.1. Particle size distribution of measured soils

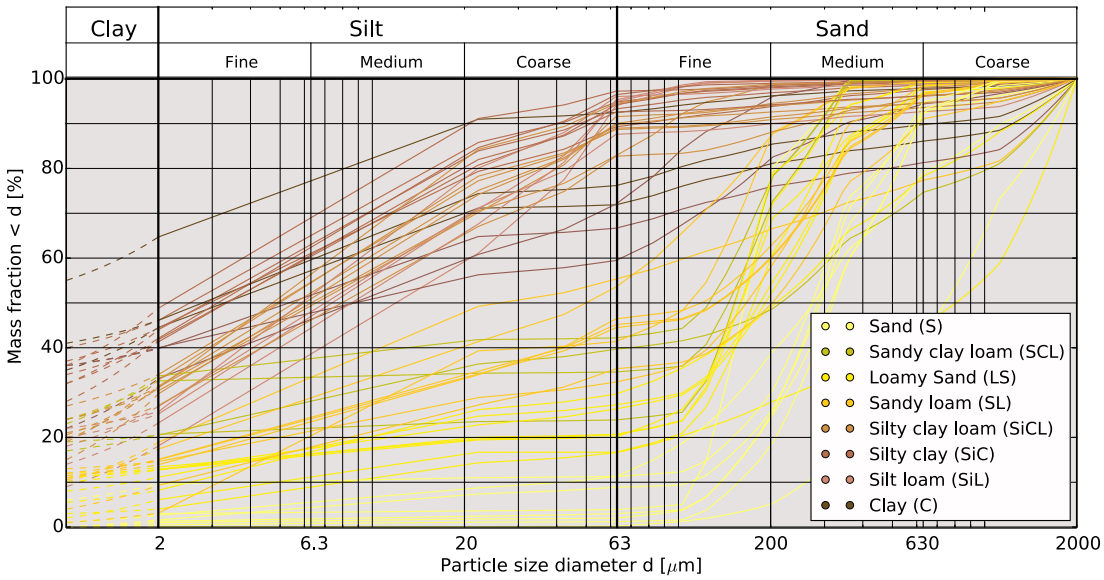

Fig. A.1.: Grain size distribution and texture classes defined after USDA (1987) for 53 different soil samples spanning the spectrum from clay (dark brown) to sand (yellow). The soils were measured by combination of sieve analysis and a sedigraph. The samples are the basis of dielectric measurements and soil moisture regression analysis as depicted in Fig. 2.6.

A.2. Soil suitability assessment for GPR

Section 4.5 described how intrinsic attenuation can be measured in the field using a field moisture sensor on the basis of TDR. Here, a device was used that actually is intended to determine moisture content and electrical conductivity at an effective frequency of ≈1 GHz. The applied device was a TRIME-PICO 64 field moisture sensor (see Fig. A.2). The description of the typical waveform for a measurement using this TDR device is shown in Fig. 3.12 and described in the methodology chapter in section 3.3. According to the described principle the device measures the reflection amplitude or more accurately, a certain point at the ascending curve of the reflected TDR signal

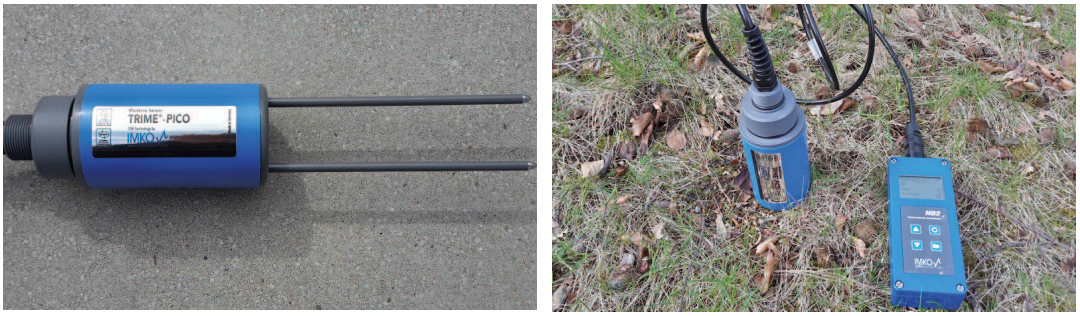

Fig. A.2.: Field moisture sensor TRIME-PICO 64based on the TDR technique (IMKO Micromodultechnik GmbH; left). Installed TDR probe with attached HD2 processing unit (right)

and deduces soil moisture content and HF-electrical conductivity by means of a set of regression functions. As depicted in the paper, we calibrated the automatically picked data point for intrinsic attenuation instead of electrical conductivity. The calibration used in the paper was based on a relatively small number of samples. In the meantime further soils have been investigated, which enables to define a more precise regression curve. Thus, the relative small amount of data as used in the paper could be enlarged by a factor of 10.

Fig. A.3 shows 130 measurements of the complex effective dielectric permittivity for 4 different soils with varying moisture content, which were fitted using a multi-component dielectric relaxation model (Eq. 4.8). Velocity and attenuation were calculated from the fitted data. The same samples were measured using the TRIME-PICO 64 TDR probe, however using a much bigger sample volume. The attenuation at 1 GHz (dashed line in Fig. A.3) that is based on the CTL measurements is plotted against the TDR-amplitude in Fig. A.4. The following regression curve was calculated for the relation between attenuation and TDR-amplitude on basis of the supplemented bigger data volume:

$$\alpha[\mathrm{dB/m}] = 231 - 2.42 \cdot A_{TDR}. \tag{A.1}$$

Fig. A.4 shows a linear correlation between both parameters with relatively small variation. However, in comparison the new regression curve only slightly deviates from the previous regression curve (Eq. 4.9 and Fig. 4.6).

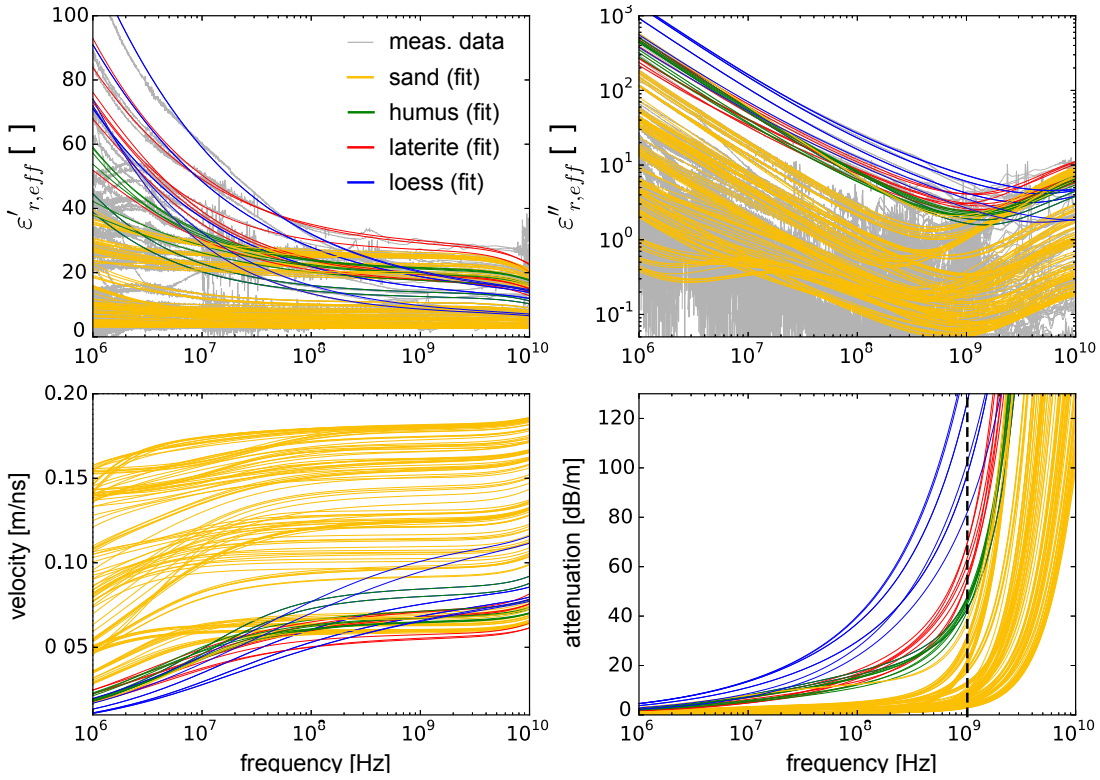

Fig. A.3.: Effective complex dielectric permittivity $\varepsilon^*_{r,eff}$ with real and imaginary part measured with dielectric spectroscopy for 4 different soil with varying water content (130 samples). The data are fitted using a multi-component dielectric relaxation model (Eq.4.8) and attenuation and velocity are calculated therefrom..

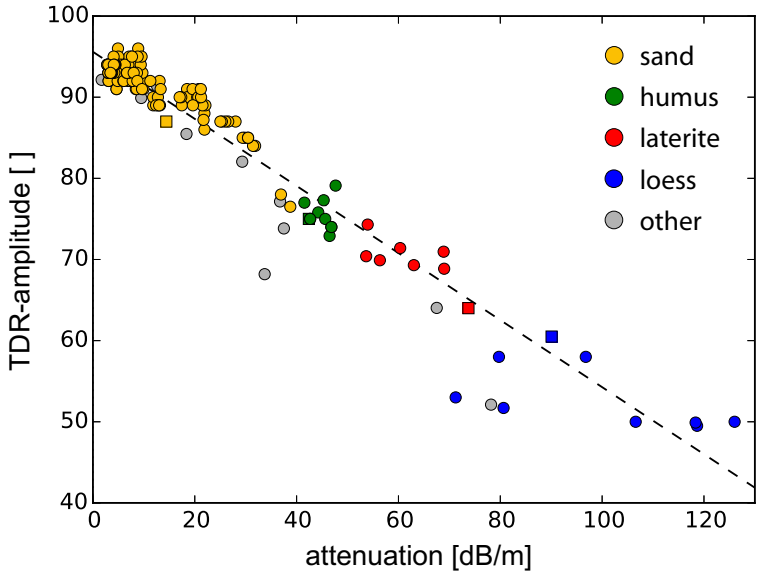

Fig. A.4.: TDR-amplitude of 130 samples of 4 soils measured by the TRIME-PICO 64 field moisture sensor against attenuation of the same samples measured by dielectric spectroscopy (see Fig. A.3). The dashed line refers to the regression equation (Eq. A.1).

Fig. A.5.: IMKO HD2 device with special adapted display and calibration to show intrinsic attenuation and permittivity.

The display of the HD2 processing unit was changed correspondingly upon request by the manufacturer and the new calibration was implemented into the software. The device now allows to show real dielectric permittivity ("DK") as well as intrinsic attenuation [in dB/m] (ger.: *Dämpfung*) directly in the field instead of soil moisture and conductivity as by the standard software (Fig. A.5). Thus, the calibrated moisture sensor provides a quick and easy opportunity to assess the GPR suitability of soils for GPR systems with ≈1 GHz center frequency and with regard to intrinsic attenuation.

Bibliography

Agilent (2014). Keysight 85071E – Materials Measurements Software, Technical Overview. `http://literature.cdn.keysight.com/litweb/pdf/5988-9472EN.pdf` [Accessed: sep 30, 2017]. 47, 68, 93

Allroggen, N. and Tronicke, J. (2016). Attribute-based analysis of time-lapse ground-penetrating radar data. *Geophysics*, 81(1):1–8. 88

Ambronn, R. (1926). Elektrische Erderforschungsmethoden. In Liesegang, R., editor, *Methoden der Angewandten Geophysik*, pages 105–150. Verlag von Theodor Steinkopff, Dresden. 28

Annan, A. (1996). Transmission dispersion and GPR. *J. Environ. Eng. Geoph.*, 1(B):125–136. 88, 103

Annan, A. (2005). chapter 11: Ground-Penetrating Radar. In Butler, D., editor, *Near-Surface Geophysics - A Tool for Hydrogeology*, pages 357–438. Society of Exploration Geophysicists. 45

Annan, A. (2009). chapter 1: Electromagentic Principles of Ground Penetrating Radar. In Jol, H., editor, *Ground Penetrating Radar - Theory and Applications*, pages 1–40. Elsevier. 8, 28, 29, 30

Annan, A. and Davis, J. (1976). Impulse radar sounding in permafrost. *Radio Sci.*, 11(4):383–394. 28

Archie, G. (1942). The electrical resistivity log as an aid in determining some reservoir characteristics. *Trans. Am. Inst. Min., Metall. Pet. Eng.*, 146:54–62. 66

Arcone, S. and Boinett, G. (2012). Maxwell-Wagner relaxation in common minerals and a desert soil at low water content. *J. Appl. Geophys.*, 81:97–105. 42, 88

Arcone, S., Grant, S., Boitnott, G., and Bostick, B. (2008). Complex permittivity and clay mineralogy of grain-size fractions in a wet silt soil. *Geophysics*, 73(3):J1–J13. 42

Athey, T., Stuchly, M., and Stuchly, S. (1982). Measurement of radio frequency permittivity of biological tissues with an open-ended coaxial line: Part I. *IEEE Trans. Microw. Theory Techn.*, 30(1):82–86. 32

Baker-Jarvis, J., Vanzura, E., and Kissick, W. (1990). Improved technique for determining complex permittivity with the transmission/reflection method. *IEEE Trans. Microw. Theory Techn.*, 38(8):1096–1103. 33

Behari, J., editor (2005). *Microwave Dielectric Behaviour of Wet Soils*. Springer, New York. 16

Benedetto, A., Benedetto, F., and Tosti, F. (2012). GPR applications for geotechnical stability of transportation infrastructures. *Nondestruct. Test. Eva.*, 27(3):253–262. 88

Bergmann, T., Robertsson, J., and Holliger, K. (1998). Finite-difference modeling of electromagnetic wave propagation in dispersive and attenuating media. *Geophysics*, 63(3):856–867. 89, 95

Binley, A., Slater, L., Fukes, M., and Cassiani, G. (2005). Relationship between spectral induced polarization and hydraulic properties of saturated and unsaturated sandstone. *Water Resour. Res.*, 41(12):W12417. 58, 59

Bobrov, P., Repin, A., and Rodionova, O. (2015). Wideband Frequency Domain Method of Soil Dielectric Property Measurements. *IEEE Trans. Geosci. Remote Sens.*, 53(5):2366–2373. 67, 118

Bockris, J., Devanathan, M., and Mueller, K. (1963). On the structure of charged interfaces. *Proc. Royal Soc. A*, 274(1356):55–79. 23

Börner, F. (2009). chapter 4: Complex conductivity measurements. In Kirsch, R., editor, *Groundwater Geophysics - A Tool for Hydrogeology, 2nd edition*, pages 119–153. Springer. 59, 67

Boukamp, B. (1993). Practical application of the Kramers-Kronig transformation on impedance measurements in solid state electrochemistry. *Solid State Ionics*, 62(1-2):131–141. 69

Boyarskii, D., Tikhonov, V., and Komarova, N. (2002). Model of dielectric constant of bound water in soil for applications of microwave remote sensing. *Prog. Electromagn. Res.*, 35:251–269. 24, 118

Bradford, J. (2007). Frequency-dependent attenuation analysis of ground-penetrating radar data. *Geophysics*, 72(3):J7–J16. 2, 42, 89

Bradford, J. (2011). Frequency dependent attenuation of GPR data as a tool for material property characterization: A review and new developments. In *6th Int. Workshop on Advanced GPR (IWAGPR), Aachen, Germany.* 2

Bradford, J., Dickins, D., and Brandvik, P. (2010). Assessing the potential to detect oil spills in and under snow using airborne ground-penetrating radar. *Geophysics*, 75(2):G1–G12. 88

Bristow, C. and Jol, H. (2003). *Ground Penetrating Radar in Sediments*. Geological Society of London, Special Publications, 211. 88

Buchner, R., Barthel, J., and Stauber, J. (1999). The dielectric relaxation of water between 0°C and 35°C. *Chem. Phys. Lett.*, 306(1-2):57–63. 21

Buchner, R. and Hefter, G. (2009). Interactions and dynamics in electrolyte solutions by dielectric spectroscopy. *Phys. Chem. Chem. Phys.*, 11(40):8984–8999. 22

Bücker, M. and Hördt, A. (2013). Analytical modelling of membrane polarization with explicit parametrization of pore radii and the electrical double layer. *Geophys. J. Int.*, 194(2):804–813. 63

Busch, S., van der Kruk, J., Bikowski, J., and Vereecken, H. (2012). Quantitative conductivity and permittivity estimation using full-waveform inversion of on-ground GPR data. *Geophysics*, 77(6):79–91. 88

Busch, S., van der Kruk, J., and Vereecken, H. (2014). Improved characterization of fine-texture soils using on-ground GPR full-waveform inversion. *IEEE Trans. Geosci. Remote Sens.*, 52(7):3947–3958. 88

Campbell (2013). *Instruction Manual - TDR Probes CS605, CS610, CS630, CS635, CS640, CS645*. `https://s.campbellsci.com/documents/ca/manuals/tdr-probes-manual.pdf` [Accessed: sep 30, 2017]. 37

Carcione, J. and Schoenberg, M. (2000). 3-D ground-penetrating radar simulation and plane-wave theory in anisotropic media. *Geophysics*, 65(5):1527–1541. 95

Cassidy, N. (2001). *The application of mathematical modelling in the interpretation of near-surface archeological ground-penetrating radar*. PhD thesis, University of Keele. 2, 89

Cassidy, N. (2007). A review of practical numerical modelling methods for the advanced interpretation of ground-penetrating radar in near-surface environments. *Near Surf. Geophys.*, 5(1):5–21. 88

Cassidy, N. (2008). GPR attenuation and scattering in a mature hydrocarbon spill: A modeling study. *Vadose Zone J.*, 7(1):140–159. 42, 88, 89

Cassidy, N. (2009). chapter 2: Electrical and magnetic properties of rocks, soils and fluids. In Jol, H., editor, *Ground Penetrating Radar - Theory and Applications*, pages 41–72. Elsevier. 12, 18, 25

Chapman, D. (1913). A contribution to the theory of electrocapillarity. *Phil. Mag.*, 25(148):475–481. 26

Chelidze, T., Gueguen, Y., and Ruffet, C. (1999). Electrical spectroscopy of porous rocks: a review– II. Experimental results and interpretation. *Geophys. J. Int.*, 137(2):16–34. 58

Chen, Y. and Or, D. (2006). Effects of Maxwell-Wagner polarization on soil complex dielectric permittivity under variable temperatures and electrical conductivity. *Water Resour. Res.*, 42(6):W06424. 58

Coffey, W. (1980). Rotational and translational brownian motion. *Adv. Mol. Relax. Process.*, 17(3-4):169 – 337. 59

Cole, K. and Cole, R. (1941). Dispersion and Absorption in Dielectrics - I. Alternating Current Characteristics. *J. Chem. Phys.*, 9(4):341–351. 26, 71

Cole, R. (1977). Time Domain Reflectometry. *Ann. Rev. Phys. Chem.*, 28:283–300. 37

Comparon, L. (2005). *Etude experimentale des proprietes electriques et dielectriques des materiaux argileux consolides*. PhD thesis, Institut de Physique du Globe de Paris. 62, 67

Conyers, L. (2013). *Ground-Penetrating Radar for Archaeology*. AltaMira Press, Lanham, MD, 3 edition. 87

Cook, J. (1960). Proposed monocycle-pulse VHF radar for airborne ice and snow measurements. *AIEE Trans. Commun. and Electron.*, 79(2):588–594. 28

Cook, J. (1973). Radar exploration through rock in advance of mining. *Trans. Soc. Min. Eng. AIME*, 254:140–146. 28

Dalton, F., Herkelrath, W., Rawlins, D., and Rhoades, J. (1984). Time Domain Reflectometry: simultaneous assessment of soil water content and electrical conductivity with a single probe. *Science*, 224(4652):989–990. 39

Daniels, D. (1996). *Surface-Penetrating Radar*. The Institution of Electrical Engineers, London, UK, 1 edition. 28

Dasberg, S. and Dalton, F. (1985). Time domain reflectometry field measurements of soil water content and electrical conductivity. *Soil Sci. Soc. Am. J.*, 49(2):293–297. 39, 119

Davis, J., Scott, W., and Annan, A. (1976). Impulse radar experiments on permafrost near Tuktoyaktuk. *Can. J. Earth Sci.*, 13(11):1584–1590. 28

Debye, P. (1913). Zur Theorie der anomalen Dispersion im Gebiete der langwelligen elektrischen Strahlung. *Verh. d. Deutsch. Phys. Ges. Jg. 15*, 16:777–793. 20

Debye, P. (1929). Polar Molecules. By P. Debye, Ph.D., Pp. 172. New York: Chemical Catalog Co., Inc., 1929. *J. Chem. Technol. Biot.*, 48(43):1036–1037. 59

Dissado, L. and Hill, R. (1987). Self-similarity as a fundamental feature of the regression of fluctuations. *Chem. Phys.*, 111(2):193–207. 59

Dobson, M., Ulaby, F., Hallikainen, M., and El-Rayes, M. (1985). Microwave dielectric behaviour of wet soil – Part II: Dielectric mixing models. *IEEE Trans. Geosci. Remote Sens.*, GE-23(1):35–46. 2, 42, 91

Doolittle, J., Minzenmayer, F., Waltman, S., Benham, E., Tuttle, J., and Peaslee, S. (2007). Ground-Penetrating Radar soil suitability map of the conterminous United States. *Geoderma*, 141:426–421. 53, 88

Ernst, J., Maurer, H., Green, A., and Holliger, K. (2007). Full-waveform inversion of crosshole radar data based on 2-D Finite-Difference Time-Domain solutions of Maxwell's equations. *IEEE Trans. Antennas.*, 45(9):2807–2828. 88

Ersahin, S., Gunal, H., Kutlu, T., Yetgin, B., and Coban, S. (2006). Estimating specific surface area and cation exchange capacity in soils using fractal dimension of particle-size distribution. *Geoderma*, 136(3-4):588–597. 118

FAO (2015). World reference base for soil resource: A framework for international classification, correlation and communication. `ftp://ftp.fao.org/agl/agll/docs/wsrr103e.pdf` [Accessed: sep 30, 2017]. 53

Fellner-Feldegg, H. (1969). Measurement of dielectrics in the time domain. *J. Phys. Chem.*, 73(3):616–623. 37

Francke, J. (2014). chapter 70: GPR Principles and Application. In Webster, J. and Eren, H., editors, *Measurements, Instrumentation and Sensors Handbook, Part VIII. Environmental*, pages 1–14. CRC Press, Boca Raton, FL. 28

Fukasawa, T., Sato, T., Watanabe, J., Hama, Y., Kunz, W., and Buchner, R. (2005). Relation between dielectric and low-frequency raman spectra of hydrogen-bond liquids. *Phys. Rev. Lett.*, 95(19):1–4. 22

Fuller, B. and Ward, S. (1970). Linear System Description of the Electrical Parameters of Rocks. *IEEE Trans. Geosci. Elec.*, 8(1):7–18. 64

Galati, G. (2016). *100 Years of Radar*. Springer, Berlin, 1st edition. 18

Gekle, S. and Netz, R. (2012). Anisotropy in the dielectric spectrum of hydration water and its relation to water dynamics. *J. Chem. Phys.*, 137(10):104704–104704–12. 76

Giannakis, I. and Giannopoulos (2014). A noval piecewise linear recursive convolution approach for dispersive media using the finite difference time-domain method. *IEEE Trans. Antennas.*, 62(5):2669–2678. 100

Giannakis, I., Giannopoulos, A., and Warren, C. (2015). A realistic FDTD numerical modeling framework of Ground Penetrating Radar for landmine detection. *IEEE J. Sel. Topics Appl. Earth Observ. in Remote Sens.*, 9(1):37–51. 88

Giannopoulos, A. (1998). *The Investigation of Transmission-Line Matrix and Finite-Difference Time-Domain Methods for the Forward Problem of Ground Probing Radar*. PhD thesis, The University of York. 98, 100

Giannopoulos, A. (2005). Modelling ground penetrating radar by gprMax. *Construction and Building Materials*, 19(10):755–762. 100

Giannopoulos, A. (2012). Unsplit implementation of higher order PMLs. *IEEE Trans. Antennas.*, 60(3):1479–1485. 101

Giese K, T. R. (1975). Determination of the complex permittivity from thin-sample time domain reflectometry. improved analysis of the step response waveform. *Adv. Mol. Relax. Process.*, 7(1):45–59. 38

Gorriti, A. and Slob, E. (2005a). Comparison of the different reconstruction techniques of permittivity from s-parameters. *IEEE Trans. Geosci. Remote Sens.*, 43(9):2051–2057. 34

Gorriti, A. and Slob, E. (2005b). A new tool for accurate s-parameters measurements and permittivity reconstruction. *IEEE Trans. Geosci. Remote Sens.*, 43(8):1727–1735. 34

Gorriti, A. and Slob, E. (2005c). Synthesis of all known analytical permittivity reconstruction techniques of nonmagnetic materials. *IEEE Trans. Geosci. Remote Sens.*, 2(4):433–436. 33, 34, 47, 68, 93

Gouy, G. (1910). Sur la constitution de la charge électrique a la surface d'un électrolyte. *J. de Phys.*, 9(1):457–468. 26

Gregory, A. and Clarke, R. (2012). Tables of the complex permittivity of dielectric reference liquids at frequencies up to 5 GHz. Technical report, NPL Report MAT 23. `http://www.npl.co.uk/content/conpublication/4295` [Accessed: sep 30, 2017]. 35, 68, 69

Griffiths, D. J. (1999). *Introduction to Electrodynamics*. Prentice-Hall Inc., New Jersey, 3rd edition. 7, 8, 10

Grimm, R., Stillman, D., Dinwiddie, C., McGinnis, R., and Sandberg, S. (2017). On conductive ground: Analysis of 'Bistatic sounding of the deep subsurface with ground penetrating radar – experimental validation' by V. Ciarletti et al. *Planet. Space Sci.*, 139:51–56. 30

Grosse, C. (2014). A program for fitting of Debye, Cole-Cole, Cole-Davidson, and Havriliak-Negami dispersions to dielectric data. *J. Colloid Interface Sci.*, 419:102–106. 59

Gueting, N., Klotzsche, A., van der Kruk, J., Vanderborght, J., Vereecken, H., and Englert, A. (2015). Imaging and characterization of facies heterogeneity in an alluvial aquifer using GPR full-waveform inversion and cone penetration tests. *J. Hydrol.*, 524:680–695. 88

Gurin, G., Titov, K., Ilyin, Y., and Tarasov, A. (2015). Induced polarization of disseminated electronically conductive minerals: a semi-empirical model. *Geophys. J. Int.*, 200(3):1555–1565. 63

Hallikainen, M., Ulaby, F., Dobson, M., El-Rayes, M., and Wu, L. (1985). Microwave dielectric behaviour of wet soil – Part I: Empirical models and experimental observations. *IEEE Trans. Geosci. Remote Sens.*, GE-23(1):25–34. 42, 91

Hasted, J. (1973). *Aqueous dielectrics*. Chapman and Hall. 44, 62

Heimovaara, T. J. (1994). Frequency domain analysis of time domain reflectometry waveforms - 1. measurement of the complex dielectric permittivity of soils. *Water Resour. Res.*, 30(2):189–199. 38

Hewlett-Packard (1964). Time Domain Reflectometry. *Hewlett-Packard Journal*, 15(6):2–8. 37

Hewlett-Packard (1993). HP 85071B Materials Measurement Software. Technical report, Hewlett Packard Company. `http://literature.cdn.keysight.com/litweb/pdf/5091-6248E.pdf` [Accessed: sep 30, 2017]. 34

Hilfer, R. (2002). H-function representations for stretched exponential relaxation and non-Debye susceptibilities in glassy systems. *Phys. Rev. E*, 65:061510. 59

Hilhorst, M., Dirksen, C., Kampers, F., and Feddes, R. (2001). Dielectric relaxation of bound water versus soil matric pressure. *Soil Sci. Soc. Am. J.*, 65(2):311–314. 118, 119

Hoekstra, P. and Delaney, A. (1974). Dielectric Properties of Soils at UHF and Microwave Frequencies. *J. Geophys. Res.*, 79(11):1699–1708. 37

Hoekstra, P. and Doyle, W. (1971). Dielectric relaxation of surface adsorbed water. *J. Colloid Interface Sci.*, 36(4):513–521. 62

Hubbard, C., West, L., Rodriguez-Blanco, J., and Shaw, S. (2014). Laboratory study of spectral induced polarization responses of magnetite – Fe2+ redox reactions in porous media. *Geophysics*, 79(1):D21–D30. 78

Hugenschmidt, J. (2010). chapter 15: Ground penetrating radar for the evaluation of reinforced concrete structures. In Maierhofer, C., Reinhardt, H.-W., and Dobmann, G., editors, *Non-destructive evaluation of reinforced concrete structures, Volume 2: Non-destructive testing methods*, pages 317–333. Woodhead Publishing Limited. 1

Hugenschmidt, J. and Kalogeropoulos, A. (2009). The inspection of retaining walls using GPR. *J. Appl. Geophys.*, 67(4):335–344. 88

Huisman, J., Hubbard, S., Redman, J., and Annan, A. (2003). Measuring Soil Water Content with Ground Penetrating Radar: A Review. *Vadose Zone J.*, 2(4):476–491. 2, 58, 88

ICBL-CMC (2016). Landmine Monitor 2016. Technical report, International Campaign to Ban Landmines. `www.the-monitor.org` [Accessed: sep 30, 2017]. 1

Igel, J. (2007). *On the Small-Scale Variability of Electrical Soil Properties and its Influence on Geophysical Measurements*. PhD thesis, Johann Wolfgang Goehte-Universität Frankfurt am Main. 2

Igel, J. (2008). The Small-Scale Variability of Electrical Soil Properties - Influence on GPR Measurements. In *12th Int. Conf. on GPR (GPR 2008), June 16-19, Birmingham, UK*. 2, 42, 52

Igel, J., Anschütz, Schmalholz, H., Wilhelm, H., Breh, W., Hötzl, H., and Hübner, C. (2001). chapter: Methods for determining soil moisture with Ground Penetrating Radar (GPR). In Breh, W., Gottlieb, J., Hötzl, H., Kern, F., Liesch, T., and Niessner, D., editors, *Field Screening Europe 2001*, pages 303–308. Springer, Dordrecht. 2

Igel, J., Günther, T., and Kuntzer, M. (2013a). Ground-penetrating radar insight into a coastal aquifer: The freshwater lens of borkum island. *Hydrol. Earth Syst. Sci.*, 17(2):519–531. 28, 58

Igel, J., Preetz, H., Takahashi, K., and Loewer, M. (2013b). Landmine and UXO detection using EMI and GPR - limitations due to the influence of the soil. *First Break*, 31(8):43–51. 1, 28

IMKO (2017). Theoretical Aspects on Measuring Moisture Using TRIME. Technical report, IMKO Micromodultechnik GmbH. `https://imko.de/phocadownload/TRIME-THEORY.pdf` [Accessed: sep 30, 2017]. 39

Irving, J. (2000). *Estimation and Correction of Wavelet Dispersion in Ground Penetrating Radar Data - Master of Science Thesis*. The University of British Columbia. 10

Irving, J. and Knight, R. (2003). Removal of wavelet dispersion form ground-penetrating radar. *Geophysics*, 68(3):960–970. 2, 42, 89

Ishida, T., Makino, T., and Wang, C. (2000). Dielectric-relaxation spectroscopy of Kaolinite, Montmorillonite, Allophane, and Imogolite under moist conditions. *Clays Clay Miner.*, 48(1):75–84. 58, 62, 63, 95

Jones, S., Wraith, J., and Or, D. (2002). Time domain reflectometry measurement principles and applications. *Hydrol. Process.*, 16(1):141–153. 119

Jonscher, A. K. (1977). The 'universal' dielectric response. *Nature*, 267(5613):673–679. 12

Kaatze, U. (1989). Complex permittivity of water as a function of frequency and temperature. *J. Chem. Eng. Data*, 34(4):371–374. 21

Kaatze, U. (2000). Hydrogen network fluctuations and the microwave dielectric properties of liquid water. *Subsurface Sensing Technologies and Applications*, 1(4):377–391. 18, 19, 21, 52, 62, 74, 95

Kaatze, U. (2007). Reference liquids for the calibration of dielectric sensors and measurement instruments. *Meas. Sci. Technol.*, 18(4):967–976. 35

Kaatze, U. (2015). chapter 3.1: Dielectric relaxation of water. In Raicu, V. and Feldmann, Y., editors, *Dielectric Relaxation in Biological Systems: Physical Principles, Methods, and Applications*. Oxford University Press. 20

Kashiwa, T. and Fukai, I. (1990). A treatment by FDTD method of dispersive characteristics associated with electromagnetic polarization. *Microw. Opt. Technol. Lett.*, 3(6):203–205. 89

Kaspan, H., Zahran, O., Elaraby, S., El-Kordy, M., and Abd El-Samie, F. (2010). A comparative study of landmine detection techniques. *Sens. Imaging*, 11:89–112. 1

Kelleners, T., Robinson, D., Shouse, P., Ayars, J., and Skaggs, T. (2005). Frequency dependence of the complex permittivity and its impact on dielectric sensor calibration in soils. *Soil Sci. Soc. Am. J.*, 69(1):67–76. 58

Kemna, A., Binley, A., Cassiani, G., Niederleithinger, E., Revil, A., Slater, L., Williams, K., Orozco, A., Haegel, F.-H., Hördt, A., Kruschwitz, S., Leroux, V., Titov, K., and Zimmermann, E. (2012). An overview of the spectral induced polarization method for near-surface applications. *Near Surf. Geophys.*, 10(6):453–468. 58, 59

Keysight-Technologies (2017). Models in the N1500A and 85071E Materials Measurement Software. Technical report, Keysight Technologies. `http://na.support.keysight.com/materials/docs/N1500A-85071EModels.pdf` [Accessed: sep 30, 2017]. 33, 34

Kim, H. and Kim, J.-H. (2011). A unified transformation function for lower and upper bounding constraints on model parameters in electrical and electromagnetic inversion. *J. Geophys. Eng.*, 8(1):21–26. 73

Klotzsche, A., van der Kruk, J., Linde, N. amd Doetsch, J., and Vereecken, H. (2013). 3-D characterization of high-permeability zones in a gravel aquifer using 2-D crosshole GPR full-waveform inversion and waveguide detection. *Geophys. J. Int.*, 195(2):932–944. 88

Knight, R. and Endres, A. (2005). chapter 3: An introduction to rock physics principles for near-surface geophysics. In Butler, D., editor, *Near-Surface Geophysics - A Tool for Hydrogeology*, pages 13–70. Society of Exploration Geophysicists. 7, 12, 13, 42, 64, 94

Knight, R. and Nur, A. (1987). The dielectric constant of sandstones, 60 kHz to 4 MHz. *Geophysics*, 52(5):644–654. 58, 62, 82, 95

Kremer, T., Schmutz, M., Leroy, P., Agrinier, P., and Maineult, A. (2016). Modelling the spectral induced polarization response of water-saturated sands in the intermediate frequency range (102 - 105 Hz) using mechanistic and empirical approaches. *Geophys. J. Int.*, 207(2):1303–1312. 58, 84

Kruschwitz, S. (2008). *Assessment of the complex resistivity behavior of salt affected building materials*. PhD thesis, Technical University Berlin. 27, 67, 69

Kruschwitz, S., Binley, A., Lesmes, D., and Elshenawy, A. (2010). Textural controls on low-frequency electrical spectra of porous media. *Geophysics*, 75(4):WA113–WA123. 82

Kruschwitz, S., Prinz, C., and Zimanthies, A. (2016). Study into the correlation of dominant pore throat size and SIP relaxation frequency. *J. Appl. Geophys.*, 135:375–386. 59, 60, 82

Kupfer, K., editor (2005). *Electromagentic Aquametry - Electromagnetic Wave Interaction with Water and Moist Substances*. Springer, Berlin. 58, 62

Kupfer, K. and Wagner, N., editors (2013). *Proc. of 10th Internat. Conf. on electromagentic water interaction with water and moist substances (ISEMA), Weimar, Germany*. 58

Lambot, S., van den Bosch, I., Stockbroeckx, B., Druyts, P., Vanclooster, M., and Slob, E. (2005). Frequency dependence of the soil electromagnetic properties derived from ground-penetrating radar signal inversion. *Subsurface Sensing Technologies and Applications*, 6(1):73–87. 88

Lang, J., Sievers, J., Loewer, M., Igel, J., and Winsemann, J. (2017). Deposits related to supercritical flows in glacifluvial deltas and subaqueous ice-contact fans: Integrating facies analysis and ground-penetrating radar. In *Proc. of 19th EGU General Assembly 2017*, page 3319. 28

Lauer, K., Wagner, N., and Felix-Henningsen, P. (2012). A new technique for measuring broadband dielectric spectra of undisturbed soil samples. *Eur. J. Soil Sci.*, 63(2):224–238. 32, 46, 48, 58, 68, 93, 95

Leroy, P. and Revil, A. (2009). A mechanistic model for the spectral induced polarization of clay materials. *J. Geophys. Res.*, 114(B10):B10202. 26, 58

Lesmes, D. and Frye, K. (2001). Influence of pore fluid chemistry on the complex conductivity and induced polarization of Berea sandstone. *J. Geophys. Res.*, 106(B3):4079–4090. 58

Lesmes, D. and Morgan, F. (2001). Dielectric spectroscopy of sedimentary rocks. *J. Geophys. Res.*, 106(B7):13329–13346. 59, 60

Loewer, M., Günther, T., Igel, J., Kruschwitz, S., Martin, T., and Wagner, N. (2017). Ultra-broadband electrical spectroscopy of soils and sediments - a combined permittivity and conductivity model. *Geophys. J. Int.*, 210(3):1360–1373. 88, 92, 93, 95

Loewer, M. and Igel, J. (2016). FDTD simulation of GPR with a realistic multi-pole Debye description of lossy and dispersive media. In *16th Int. Conf. on GPR (GPR 2016), June 16-19, Hong Kong*. 39, 58

Loewer, M., Igel, J., Minnich, C., and Wagner, N. (2016a). Electrical and dielectric properties of soils in the mHz to GHz frequency range. In *Proc. of 11th Int. Conf. on Electromagnetic Wave Interaction with Water and Moist Substances (ISEMA 2016), Florence*, pages 247–254. 70

Loewer, M., Igel, J., and Wagner, N. (2016b). Spectral decomposition of soil electrical and dielectric losses and prediction of in situ GPR performance. *IEEE J. Sel. Topics Earth Obs. Remote Sens.*, 9(1):212–220. 58, 88

Luebbers, R. and Hunsberger, F. (1992). FDTD for Nth-order dispersive media. *IEEE Trans. Antennas.*, 40(11):1297–1301. 98

Luebbers, R., Hunsberger, F., and Kunz, K. (1991). A frequency-dependent finite-difference time-domain formulation for transient propagation in plasma. *IEEE Trans. Antennas.*, 39(1):29–34. 89

Luebbers, R., Hunsberger, F., Kunz, K., Standler, R., and Schneider, M. (1990). A frequency-dependent finite-difference time-domain formulation for dispersive materials. *IEEE Trans. Electromagn. Compat*, 32(3):222–227. 98

Mao, D., Revil, A., and Hinton, J. (2016). Induced polarization response of porous media with metallic particles – Part 4: Detection of metallic and nonmetallic targets in time-domain-induced polarization tomography. *Geophysics*, 81(4):345–361. 63

Marquardt, D. W. (1963). An algorithm for least-squares estimation of nonlinear parameters. *J. Soc. Ind. Appl. Math.*, 11(2):431–441. 73

Marshall, D. and Madden, T. (1959). Induced polarization. a study of its causes. *Geophysics*, 24(4):780–816. 63

Martin, T., Nordsiek, S., and Weller, A. (2015). Low-frequency impedance spectroscopy of wood. *Journal of Research in Spectroscopy*, 2015(910447). 67

Maxwell, J. (1881). *Treatise on Electricity and Magnetism*. Clavendon Press, Oxford, 1st edition. 25

Meles, G., Greenhalgh, S., Green, A., Maurer, H., and Van der Kruk, J. (2012). GPR full waveform sensitivity and resolution analysis using an FDTD adjoint method. *IEEE Trans. Geosci. Remote Sens.*, 50(5):1881–1896. 88

Miller, T., Hendrickx, J., and Borchers, B. (2004). Radar detection of buried landmines in field soils. *Vadose Zone J.*, 3(4):1116–1127. 42

Mironov, V., Kosolapova, L., and Fomin, S. (2008). Soil dielectric model accounting for contribution of bound water spectra through clay content. *Prog. Electromagn. Res. Symp. Online*, 4(1):31–35. 91

Misra, D., Chabbra, M., Epstein, B., Microtznik, M., and Foster, K. (1990). Non-invasive electrical characterization of materials at microwave frequencies using an open-ended coaxial line: test of an improved calibration technique. *IEEE Trans. Microw. Theory Techn.*, 38(1):8–14. 32

Morey, R. (1974). Detection of subsurface cavities by ground penetrating radar. *Proc. of Highway Geological Symposium*, 27:28–30. 28

Nelson, P. (1994). Permeability-porosity relationships in sedimentary rocks. *Log Analyst*, 35(3):38–62. 66

Neubauer, W., Gugl, C., Scholz, M., Verhoeven, G., Trinks, I., Löcker, K., Doneus, M., Saey, T., and Van Meirvenne, M. (2014). The discovery of the school of gladiators at Carnuntum, Austria. *Antiquity*, 88:173–190. 88

Nicolson, A. and Ross, G. (1970). Measurement of the intrinsic properties of materials by time domain techniques. *IEEE Trans. Instrum. Meas.*, 19(4):377–382. 33

Nielsen, L., Møller, I., Nielsen, L., Johannessen, P., Pejrup, M., Andersen, T., and Korshøj, J. (2009). Integrating ground-penetrating radar and borehole data from a wadden sea barrier island. *J. Appl. Geophys.*, 68(1):47–59. 88

Nordsiek, S. and Weller, A. (2008). A new approach to fitting induced-polarization spectra. *Geophysics*, 73(6):F235–F245. 71

Oĝuz, U. and Gürel, L. (2002). Frequency responses of ground-penetrating radar operating over highly lossy ground. *IEEE Trans. Geosci. Remote Sens.*, 40(6):1385–1394. 88

Olhoeft, G. and Capron, D. (1993). Laboratory measurements of the radiofrequency electrical and magnetic properties of soils from near Yuma, Arizona. In *Open File report 93-701*, pages 1–214. U.S. Department of the Interior, U.S. Geological Survey. 2

Olhoeft, G. and Capron, D. (1994). Petrophysical causes of electromagnetic dispersion. In *5th Int. Conf. on GPR (GPR 1994), June 12-16, Kitchener, Ontario, Canada*, pages 145–152. 12, 42

Olhoeft, G. and Strangway, D. (1973). Magnetic relaxation and the electromagentic response parameter. *Geophysics*, 39(3):302–311. 78

Olmi, R. and Bittelli, M., editors (2016). *Proc. of 11th Int. Conf. on Electromagentic Wave Interaction with Water and Moist Substances (ISEMA), Florence, Italy*. 58

Or, D. and Wraith, J. (1999). Temperature effects on soil bulk dielectric permittivity measured by time domain reflectometry: A physical model. *Water Resour. Res.*, 35(2):1202–1215. 24

Orfanidis, S. J. (2013). *Electromagnetic Waves and Antennas - Ch. 1: Maxwell's Equations*. ECE Department - Rutgers University, NJ. `www.ece.rutgers.edu/~orfanidi/ewa` [Accessed: sep 30, 2017]. 7, 10

Pachepsky, Y., Timlin, D., and Varallyay, G. (1996). Artificial neural networks to estimate soil water retention from easily measurable data. *Soil Sci. Soc. Am. J.*, 60(3):727–733. 23

Peplinski, N., Ulaby, F., and Dobson, M. (1995). Dielectric properties of soils in the 0.3-1.3 GHz range. *IEEE Trans. Geosci. Remote Sens.*, 33(3):803–807. 91

Polizos, G., Vaia, R., Koerner, H., and Manias, E. (2013). Dynamics of amphiphilic surfactants confined in montmorillonite slits with different cation exchange capacities. *J. Phys. Chem. B*, 117(43):13667–13678. 62

Popov, V., Ishai, P., Khamzin, A., and Feldmann, Y. (2016). The mechanism of the dielectric relaxation of water. *Phys. Chem. Chem. Phys.*, 18(20):13941–13953. 20

Powers, M. (2001). *Dispersive Ground Penetrating Radar Modeling in 2D*. PhD thesis, Colorado School of Mines. 2, 7, 13

Rako, P. (2007). TDR: Taking the pulse of signal integrity. *EDN*, September 3:49–59. 37

Redman, J. (2009). chapter 8: Contaminant mapping. In Jol, H., editor, *Ground Penetrating Radar - Theory and Applications*, pages 247–270. Elsevier. 1

Revil, A. (2012). Spectral induced polarization of shaly sands: Influence of the electrical double layer. *Water Resour. Res.*, 48(2):1–23. 16

Revil, A. (2013). Effective conductivity and permittivity of unsaturated porous materials in the frequency range 1 mHz-1 GHz. *Water Resour. Res.*, 49(W02517):306–327. 27, 60, 67

Revil, A. (2014). Comment on: 'On the relationship between induced polarization and surface conductivity: Implications for petrophysical interpretation of electrical measurements' (Weller, A., Slater, L. and Nordsiek, S., Geophysics, 78, no. 5, D315–D325). *Geophysics*, 79(2):X1–X5. 58

Revil, A. and Florsch, N. (2010). Determination of permeability from spectral induced polarization in granular media. *Geophys. J. Int.*, 181(2):1480–1497. 58

Revil, A. and Skold, M. (2011). Salinity dependence of spectral induced polarization in sands and sandstones. *Geophys. J. Int.*, 187(2):813–824. 61, 63

Reynolds, J. (1997). *An Introduction to Applied and Environmental Geophysics*. Wiley-Blackwell, 2nd edition. 31

Robinson, D., Jones, S., Wraith, J., Or, D., and Friedman, S. (2003). A review of advances in dielectric and electrical conductivity measurement in soils using Time-Domain Reflectometry. *Vadose Zone J.*, 2(4):444–475. 37, 38, 53, 58, 119

Rotenberg, B., Cadene, A., Dufrêche, J., Durand-Vidal, S., Badot, J.-C., and Turq, P. (2005). An analytical model for probing ion dynamics in clays with broadband dielectric spectroscopy. *J. Phys. Chem. B*, 109(32):2267–2273. 26, 62, 76, 95

Roth, K., Schulin, R., Flühler, H., and Attinger, W. (1990). Calibration of Time-Domain Reflectometry for water content measurement using a composite dielectric approach. *Water Resour. Res.*, 26(10):2267–2273. 58

Rücker, C., Günther, T., and Wagner, F. (2016). pyGIMLi - An Open Source Python Library for Inversion and Modelling in Geophysics. In *78th EAGE Conference & Exhibition 2016, WS08-Open Source Software in Applied Geosciences*. `https://www.pygimli.org` [Accessed: sep 30, 2017]. 48, 72, 96

Saarenketo, T. and Scullion, T. (2000). Road evaluation with ground penetrating radar. *J. Appl. Geophys.*, 43(2-4):119–138. 28

Santamarina, J., Klein, K., and Fam, M., editors (2001). *Soils and Waves: Particulate Materials Behaviour, Characterization and Process Monitoring*. John Wiley & Sons, LTD. 22, 23, 25, 26, 58, 62

Sato, M., Takahashi, K., and Fujiwara, J. (2007). Development of the Hand held dual sensor ALIS and its evaluation. In *4th Int. Workshop on Advanced GPR (IWAGPR), Italy*. 88

Schön, J. (2015). *Physical Properties of Rocks – Fundamentals and Principles of Petrophysics*. Developments in Petroleum Science. Elsevier, 2nd edition. 61, 63, 66, 78

Schopper, J. (1982). Porosity and permeability. In Hellwege, K. and Madelung, O., editors, *Landolt-Börnstein. Numer. Data and Func. Relat. Sci. Technol. New Ser., Group V: Geophys. Space Res., vol. 1, Physical Properties of Rocks, subvol. A*. Springer. 66

Schwartz, R., Evett, S., Pelletier, M., and Bell, J. (2009). Complex permittivity model for time-domain reflectometry soil water content sensing: I. Theory. *Soil Sci. Soc. Am. J.*, 73(3):886–897. 58

Schwarz, G. (1962). A theory of the low-frequency dielectric dispersion of colloidal particles in electrolyte solution. *J. Phys. Chem.*, 66(12):2636–2642. 62

Schwing, M. (2015). *Mechanical, hydraulic, and dielectric characterisation of fine-grained soils during densification*. PhD thesis, The University of Queensland. 23, 61

Schwing, M., Chen, Z., Scheuermann, A., and Wagner, N. (2013). Dielectric properties of a clay soil determined in the frequency range from 1 MHz to 40 GHz. In *Proc. of 10th Int. Conf. on Electromagnetic Wave Interaction with Water and moist substances, Weimar*, pages 242–250. 48

Seigel, H. (1959). Mathematical formulation and type curves for induced polarization. *Geophysics*, 24(3):547–565. 71

Shen, L., Savre, W., Price, J., and Athavale, K. (1985). Dielectric properties of reservoir rocks at ultra-high frequencies. *Geophysics*, 50(4):692–704. 42

Sischka, F. (2010). IC-CAP Modeling Handbook. *Agilent Technologies*. `https://wiki.epfl.ch/carplat/documents/iccapmhb.pdf` [Accessed: sep 30, 2017]. 33

Slater, L. and Comas, X. (2009). chapter 7: The contribution of ground penetrating radar to water resource research. In Jol, H., editor, *Ground Penetrating Radar - Theory and Applications*, pages 203–246. Elsevier. 1

Sposito, G. and Prost, R. (1982). Structure of Water Adsorbed on Smectites. *Chem. Rev.*, 82(6):6065–6073. 61

Sposito, G., Skipper, N., Sutton, R., Park, S., Soper, A., and Greathouse, J. (1999). Surface geochemistry of the clay minerals. *Proc. Natl. Acad. Sci. USA*, 96(7):3358–3364. 23

Stacheder, M. (1996). *Schriftenreihe Angewandte Geologie Karlsruhe 40, I-XV*, chapter Die Time Domain Reflectometry in der Geotechnik - Messung von Wassergehalt, elektrischer Leitfähigkeit und Stofftransport, pages 1–170. Universität Karlsruhe. 54

Stern, O. (1924). Zur Theorie der elektrolytischen Doppelschicht. *Zeitschrift für Elektrochemie*, 20:508–516. 25

Stillman, D., Grimm, R., and Dec, S. (2010). Low-Frequency Electrical Properties of Ice-Silicate Mixtures. *J. Phys. Chem. B*, 114(18):6065–6073. 85

Stillman, D. and Olhoeft, G. (2008). Frequency and temperature dependence in electromagentic properties of martian analog minerals. *J. Geophys. Res.*, 113(E9). 42

Taherian, M., Kenyon, W., and Safinya, K. (1990). Measurements of dielectric response of water-saturated rocks. *Geophysics*, 55(12):1530–1541. 42

Takahashi, K., Igel, J., and Preetz, H. (2012). Modeling of GPR clutter caused by soil heterogeneity. *Int. J. Antennas Propag.*, 2012(7):31–38. 2, 42

Takahashi, K., Preetz, H., and Igel, J. (2011). Soil properties and performance of landmine detection by metal detector and ground-penetrating radar - Soil characterization and its verification by a field test. *J. Appl. Geophys.*, 73(4):368–377. 1, 28, 31, 42, 52

Takahashi, K. and Sato, M. (2008). A hand-held dual-sensor system using impulse GPR for demining. In *Proc. of 2008 IEEE Int. Conf. on Ultra-Wideband (ICUWB2008)*, volume 3. 1, 42, 52

Tarasov, A. and Titov, K. (2013). On the use of the Cole-Cole equations in spectral induced polarization. *Geophys. J. Int.*, 195(1):352–356. 59, 60, 84

Teixeira, F., Chew, W., Straka, M., Oristaglio, M., and Wang, T. (1998). Finite-difference time-domain simulation of ground penetrating radar on dispersive, inhomogeneous, and conductive soils. *IEEE Trans. Geosci. Remote Sens.*, 36(6):1928–1937. 89, 95

Teschke, O., Ceotto, G., and de Souza, E. (2001). Interfacial water dielectric-permittivity-profile measurements using atomic force microscopy. *Phys. Rev. E Stat. Nonlin. Soft Matter Phys.*, 64(1):1–10. 23, 24

Tierbach, R. (1974). Electromagnetic reflections in salt deposits. *Journal of Geophysics*, 40:633–637. 28

Titov, K., Komarov, V., Tarasov, V., and Levitski, A. (2002). Theoretical and experimental study of time domain-induced polarization in water-saturated sands. *J. Appl. Geophys.*, 50(4):417–433. 61

Titov, K., Tarasov, A., Ilyin, Y., Seleznev, N., and Boyd, A. (2010). Relationship between induced polarization relaxation time and hydraulic properties of sandstone. *Geophys. J. Int.*, 180(3):1095–1106. 82

Topp, G., Davis, J., and Annan, A. (1980). Electromagnetic determination of soil water content: Measurement in coaxial transmission lines. *Water Resour. Res.*, 16(3):574–582. 2, 19, 37, 38, 43, 58

Topp, G., Yanuka, M., Zebchuk, W., and Zegelin, S. (1988). Determination of electrical conductivity using time domain reflectometry: Soil and water experiments in coaxial lines. *Water Resour. Res.*, 24(7):945–952. 38, 119

Tosti, F., Patriarca, C., Slob, E., Benedetto, A., and Lambot, S. (2013). Clay content evaluation in soils through GPR signal processing. *J. Appl. Geophys.*, 97:69–80. 88

USDA, S. C. S. (1987). *Soil Mechanics Level I, Module 3 – USDA Textural Soil Classification*. `https://www.nrcs.usda.gov/Internet/FSE_DOCUMENTS/stelprdb1044818.pdf` [Accessed: sep 30, 2017]. 19, 66, 91, 92, 125

Ustra, A., Mendonça, C., Ntarlagiannis, D., and Slater, L. (2016). Relaxation time distribution obtained from a Debye decomposition of spectral induced polarization data. *Geophysics*, 81(2):E129–E138. 71

Van der Bosch, I., Lambot, S., Druyts, D., Huynen, I., and Acheroy, M. (2006). Buried target signature extraction from ground-penetrating radar signal: measurements and simulations. *Near Surf. Geophys.*, 4(1):31–38. 42

Vaughan, C. (1986). Ground-penetrating radar surveys used in archaeological investigations. *Geophysics*, 51(3):595–604. 1

Vaughan, D., Corr, H., Doake, C., and Waddington, E. (1999). Distortion of isochronous layers in ice revealed by ground-penetrating radar. *Nature*, 398:323–326. 1

Volkmann, J. and Klitzsch, N. (2015). Wideband impedance spectroscopy from 1 mHz to 10 MHz by combination of four-and two-electrode methods. *J. Appl. Geophys.*, 114:191–201. 59, 69

von Hippel, A. (1954). *Dielectrics and Waves*, volume 1. Wiley and Sons, New York, 1st edition. 37

Wagner, K. (1913). Zur Theorie der unvollkommenen Dielektrika. *Ann. Phys.*, 345:817–855. 25

Wagner, N., Bore, T., Robinet, J., Coelho, D., Taillade, F., and Delepine-Lesoille, S. (2013). Dielectric relaxation behaviour of callovo-oxfordian clay rock: A hydraulic-mechanical-electromagnetic coupling approach. *J. Geophys. Res. B: Solid Earth*, 118(9):4729–4744. 23, 32, 52, 58, 68, 70, 76, 93, 95, 117, 118

Wagner, N., Emmerich, K., Bonitz, F., and Kupfer, K. (2011). Experimental investigations on the frequency- and temperature- dependent dielectric material properties of soils. *IEEE Trans. Geosci. Remote Sens.*, 49(7):2518–2530. 14, 16, 32, 43, 58, 70, 95

Wagner, N., Kupfer, K., and Trinks, E. (2007). A broadband spectroscopy study of the relaxation behaviour of subsoil. In *Proc. of 7th Int. Conf. on Electromagentic Wave Interaction with Water and Moist Substances (ISEMA), Hamamatsu, Japan*, pages 31–38. 61, 67

Wagner, N., Müller, B., Kupfer, K., Schwing, M., and Scheuermann, A. (2010). Broadband electromagnetic characterization of two-port rod based transmission lines for dielectric spectroscopy in soils. In *Proc. of First Europ. Conf. on Moisture Measurement (Aquametry 2010), Weimar*, pages 228–237. 46, 48

Wagner, N. and Scheuermann, A. (2009). On the relationship between matric potential and dielectric properties of organic free soils: A sensitivity study. *Can. Geotech. J.*, 46(10):1202–1215. 16, 21, 23, 24, 26, 43, 58, 70, 118, 119

Wang, Y. (2015). Frequencies of the ricker wavelet. *Geophysics*, 80(2):31–37. 30, 101

Warren, C., Giannopoulos, A., and Giannakis, I. (2016). gprMax: Open source software to simulate electromagnetic wave propagation for Ground Penetrating Radar. *Comput. Phys. Commun.*, 209:163–170. 100

Waxman, M. and Smits, L. (1968). Electrical conductivities in oil-bearing shaly sands. *Soc. Petrol. Eng. J.*, 8(2):107–122. 66

Weigand, M. and Kemna, A. (2016). Relationship between Cole-Cole model parameters and spectral decomposition parameters derived from SIP data. *Geophys. J. Int.*, 205(3):1414–1419. 59, 84

Weir, W. (1974). Automatic measurement of complex dielectric constant and permeability at microwave frequencies. *Proc. of IEEE*, 62(1):33–36. 33

Weller, A., Slater, L., and Nordsiek, S. (2013). On the relationship between induced polarization and surface conductivity: Implications for petrophysical interpretation of electrical measurements. *Geophysics*, 78(5):D315–D325. 58

Weller, A., Slater, L., and Nordsiek, S. (2014). Reply to the discussion by A. Revil, Comment on: 'On the relationship between induced polarization and surface conductivity: Implications for petrophysical interpretation of electrical measurements' (Weller, A., Slater, L. and Nordsiek, S. Geophysics, 78, no. 5, d315–d325). *Geophysics*, 79(2):X6–X10. 58

Weller, A., Zhang, Z., Slater, L., Kruschwitz, S., and Halisch, M. (2016). Induced polarization and pore radius - A discussion. *Geophysics*, 81(5):D519–D526. 58

Wraith, J., Robinson, D., Jones, S., and Long, D. (2005). Spatially characterizing apparent electrical conductivity and water content of surface soils with time domain reflectometry. *Comput. Electron. Agric.*, 46(1–3):239–261. 119

Wunderlich, T. and Rabbel, W. (2013). Absorption and frequency shift of GPR signals in sandy and silty soils: empirical relations between quality factor Q, complex permittivity and clay and water contents. *Near Surf. Geophys.*, 11(2):1–11. 2, 88

Xu, T. and McMechan, G. (1997). GPR attenuation and its numerical simulation in 2.5 dimensions. *Geophysics*, 62(1):403–414. 95, 96

Yee, K. (1966). Numerical solution of initial boundary value problems involving Maxwell's equations in isotropic media. *IEEE Trans. Antennas.*, AP-14(3):302–307. 100

Yelf, R. (2007). Application of ground penetrating radar to civil and geotechnical engineering. *Electromagn. Phenom. J.*, 7(1):102–117. 1, 28

Young, J. (1995). Propagation in linear dispersive media: Finite difference time-domain methodologies. *IEEE Trans. Antennas.*, 43(4):422–426. 89

Zimmermann, E., Kemna, A., Berwix, J., Glaas, W., and Vereecken, H. (2008). EIT measurement system with high phase accuracy for the imaging of spectral induced polarization properties of soils and sediments. *Meas. Sci. Technol.*, 19(9):094010. 67

Acknowledgments

I want to express my gratitude to people and institutions who supported my work.

I am very grateful for partial funding of the projects by the Federal Ministry of Defense, Germany (grant no. C/E520/DF019/AF199) and by the support of the Leibniz Institute for Applied Geophysics (LIAG), Hannover, where I carried out most part of the work.

I thank Prof. Charlotte Krawczyk for her encouragement at the LIAG and for examining my thesis at the TU Berlin. Furthermore, I thank Prof. Frank Börner and Prof. Jens Tronicke for reviewing and examining this work. Without the technical and scientific advice of Dr. Norman Wagner and our discussions on dielectric spectroscopy, many ideas in the thesis would not have been born. My deepest appreciation and intellectual dept goes to Dr. Jan Igel for his mentoring, as well as for being a great colleague and friend, who supervised my work at the LIAG. I also want to thank Dr. Holger Preetz for our insightful discussions on the 'landmine project' and his constant encouragements. Special thanks also go to Dr. Thomas Günther for his support in using the GIMLi inversion toolbox and his advice on the new phenomenological model. I thank Dr. Tina Martin for her help and permission to use the measurement facilities in Berlin and I also appreciate the discussions I had with Prof. Sabine Kruschwitz on SIP.

The S2 technical team at LIAG, represented by Dieter Epping, Robert Meyer and Wolfgang Südekum was an invaluable help. I am also grateful to Cynthia Minnich for assisting the measurements and I will never forget our endurance runs after work. I also want to thank the staff of WTD 52 in Oberjettenberg and all colleagues that were involved in the 'landmine & counter-IED' projects for their assistance and support.

I am deeply grateful to all young researchers and research assistants at the LIAG for being fantastic colleagues and comrades, who also shared common interests with me in their free time. Thanks for the good time!

Last but not least, I thank my family for their patience, constant encouragement and appreciation.